Modeling, Sensing, and Estimation for Miniature Dynamic Systems with Contact

by

Jinhong Qu

A dissertation submitted in partial fulfillment
of the requirements for the degree of
Doctor of Philosophy
(Mechanical Engineering)
in the University of Michigan
2018

Doctoral Committee:

Associate Professor Kenn R. Oldham, Chair
Professor Bogdan I. Epureanu
Associate Professor Anouck R. Girard
Professor Noel C. Perkins

Jinhong Qu

jinhongq@umich.edu

ORCID iD: 0000-0003-3017-9235

ACKNOWLEDGEMENT

The author thanks Professor Kenn R. Oldham for his time and patient in last 8 years.

The author thanks Vibration and Acoustics Laboratory for the help in micro-robot project:

Professor Karl Grosh, Dr. Jongsoo Choi, Dr. Minchul Shin, Dr. Kendall Teichert, Clark B. Teeple, Yi Chen, Lu Wang, Mayur Birla, Hermione Li, Buyi Zhang, Ketul Patel, Joseph Jang, and everybody else

The author thanks Wireless Integrated MicroSensing & Systems (WIMS) for the help in micro-motor project:

Professor Yogesh Gianchandani, Dr. Scott Green, Dr. Jun Tang, Professor Khalil Najafi, Dr. Jong Kwan Woo and everybody else.

The author thanks Lurie Nanofabrication Facility and Army Research Laboratory for the help in fabrication and design process.

This work was supported by DARPA MTO, contract W31P4Q-12-1-0002 (PASCAL Program) and NSF awards CMMI 1435222, IIS 1208233, and CMMI 0954422.

TABLE OF CONTENTS

LIST OF TABLES

LIST OF FIGURES

ABSTRACT

This dissertation focuses on modeling and sensing for miniature devices characterized by mixed elastic and rigid body motion with contact. Understanding dynamics of miniature devices, including microelectromechanical systems (MEMS) and related small-scale prototypes, is valuable for improving device design and helping develop estimation and control algorithms for better performance. This work particularly emphasizes dynamic modeling of small-scale devices that depend on contact interactions between structures to generate continuous or repeated motion, and thus modeling will incorporate contact dynamics within devices featuring both compliant and rigid components.

The first task is to model the dynamics of a magnetoelastic micro-motor. The magnetoelastic micro-motor has characteristics of large payload capacity and feasibility of bidirectional motion. These characteristics suggest it as a good candidate for gyroscope calibration in the field as a type of miniature rate table. This task proposes a dynamic model including both a compliant model for the stator and bidirectional rigid body motion model for the rotor, with a capacitive sensing design to precisely track the motor motion. The contact interactions between the stator and rotor are the key feature of the micro-motor actuation, so the influence of this interaction is modeled for a better understanding of the micro-motor behavior. Stochastic bouncing motion of the magnetoelastic rotor is not ideal for a controlled motion, such that the dynamic model helps compensate for this limitation of magnetoelastic actuation. Experimental comparison validates the dynamic model for a reproduction of major micro-motor dynamic features. Capacitive sensing based on this work is predicted to compensate for off-axis motion.

The second task is to model the nonlinear hybrid dynamics of a piezoelectric walking micro-robot. The piezoelectric micro-robot is suitable for integration with control and power systems because a relatively large payload can be supported at low power. However, piezoelectric actuation usually provides a relatively short actuation stroke, and to overcome this drawback, piezoelectric actuators are often operated near their resonance. Therefore, the dynamics of the piezoelectric micro-robot is formulated using a resonance-based model for its compliant leg mechanisms and rigid chassis motion moving in multiple degrees of freedom. The dynamic model including those features, along with contact dynamics between the robot and ground, is desirable for future implementation of control strategies and locomotion over complex terrain. Experiments are also performed on two centimeter-scale robot prototypes to validate the robot dynamics when using a simplified foot-terrain interaction model.

The third task is to improve micro-robot performance using the resulting understanding of the robots' nonlinear hybrid dynamics. One such step is the development of optimization algorithms for robot inputs. Acquisition of on-board sensing information of robot motion is first addressed. Then the performance of optimization algorithms with and without such information can help determine the importance of on-board sensing. The swarm performance of robots is also studied using swarm optimization, which is implemented in simulation using representative on-board sensing signals. Another application is to develop alternate potential locomotion gaits for a single robot from a design standpoint. Both applications are studied using rapid prototyping and simulations, which are then extended to predictions for true micro-scale robots.

CHAPTER 1 Introduction

1.1 Background

Microelectromechanical systems (MEMS) have established themselves in many applications during the last half century. Major classes of MEMS devices include sensors, such as inertial sensors [1] and pressure sensors [2], and actuators, such as inkjet printing heads [3] and micro-mirrors [4]. Miniature actuation technologies have become progressively more advanced, with various transduction mechanisms having been tested across a wide variety of devices. Among these, for example, micro-scale robotic systems with capabilities for micro- and meso-scale manipulation and locomotion are attractive for applications such as defense, disaster response, and exploration. As another example, various MEMS devices have been developed to generate rotational and translational motion at small scales. Micro-motors and micro-robots are examples of MEMS devices that make possible large rotational and translational motions through repetition of smaller displacements.

To realize useful motion at small scales, actuator design, power budget, and control techniques should ideally all be taken into consideration. Actuation, including structural design, the transduction principle, and dynamic behavior, is a key design element of many MEMS devices. Meanwhile, both device efficiency and effectiveness are tightly related to the power requirements of the device. Finally, control algorithms should also be developed based on an understanding of the device's actuation scheme and dynamics.

Structural geometry and transducer designs for MEMS devices are generally limited by microfabrication technologies. Planar micromachining technologies are still the most common and efficient choice for producing MEMS devices, though some 3D fabrication [5] technologies are available for specific materials. The transduction choice determines how a MEMS device will produce force transduced from another energy source to overcome stiffness, friction, damping, and other external forces to produce movement at the micro-scale. Common transduction principles for micro actuators include, but are not limited to, piezoelectric, electrostatic, electrothermal, and magnetoelastic actuation. The output schemes of different transduction principles are not identical, but they can generally be simplified to a force-displacement relationship within an actuation range. While fabrication and transduction mechanisms in MEMS are constrained, dynamics of movable MEMS devices can be highly complex because of the diversity of possible geometries and mass and force distributions. Dynamics can become even more complex in the presence of nonlinear contact and/or interaction between a device and its external environment [6]. Some MEMS devices [7], including those that are the focus of this work, take advantage of impact contact to perpetuate motion. Therefore, understanding the dynamics of MEMS devices becomes a dominant concern for design optimization, estimation, and control.

Nonlinear dynamics appear frequently in the study of MEMS devices at small scales, though often motions can be simplified to piece-wise linear because the motion range is limited. Meanwhile, while hybrid dynamic modeling and analysis are common topics in larger-scale applications, they are less common in small scales because discrete transitions of dynamics, as by changes in physical contacts or configurations, are comparatively rare. Such behaviors increase design complexity and reliability challenges for devices, and thus are commonly avoided in micro-scale systems. However, given functional limits of simple device designs, it can be important to push the understanding of micro-scale dynamics towards this more complex level. In this work, nonlinear hybrid dynamics in multiple domains are studied for some sample devices, namely a rotary micro-motor and terrestrial micro-robot. This work breaks device behavior into an appropriate set of models for various conditions. With a reasonable understanding of the micro-scale dynamics of devices from the fundamental concepts of physics, this

modeling can help improve the design and prediction of devices' performance, improvement and optimization algorithm development, and experimental testing design. Examples of micro-scale devices that might benefit from this work include:

1) Robotic systems with various locomotion strategies such as walking, swimming, and flying;

2) Micro mechanical devices experiencing contact events such as motors, gears, mechanisms, and valves;

3) Micro tools interacting with a changing external environment such as probes, tweezers, sorters, and Atomic force microscopy (AFM) elements;

4) Navigation measurement units such as accelerometers and gyroscopes.

1.1.1 Micro-motors

Chip-scale rotary micro-motors based on magnetoelastic transduction have recently been demonstrated. These motors join those based on other transduction mechanisms, such as electrostatic and piezoelectric transduction [8], for realizing chip-scale rotary motion. In general, micro-motors based on smart materials and fabricated by MEMS technology at small scales have demonstrated better efficiency than chip-scale versions of traditional electromagnetic motors. The early development of MEMS micro-motors (Figure 1) starts around the 1980s with electrostatic actuation [9]. This sort of micro-motor is designed with the rotary component (rotor) constrained by a hub at its rotation axis, and actuated with capacitive force generated across the gap between the rotor and a fixture placed around the rotor. The electrostatic micro-motors are easily adapted to standard fabrication processes, including standard integrated circuit (IC) processing [9]. But, the electrostatic micro-motors require large voltages and produce limited torque.

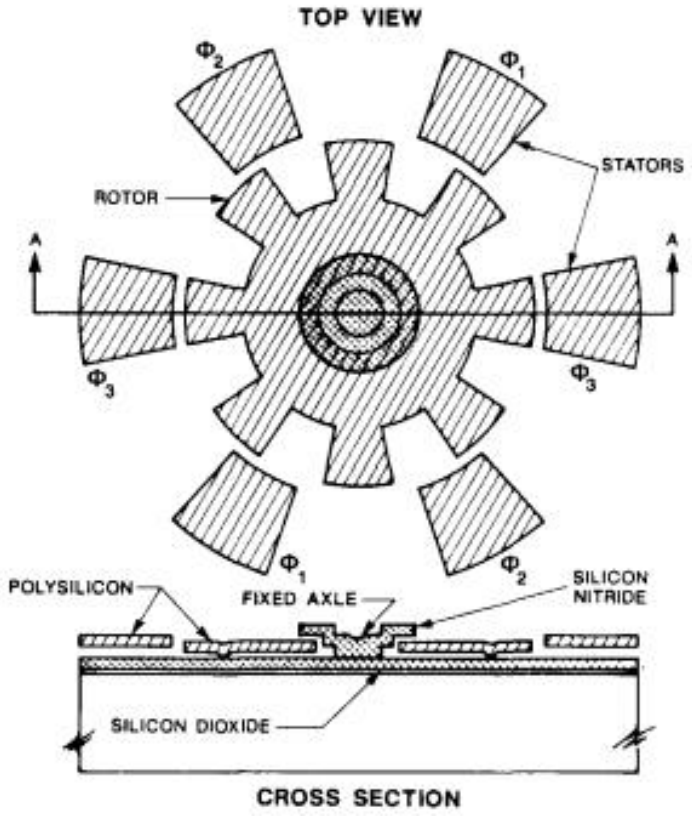

Figure 1 Top view and cross-section of a stepping electrostatic micromotor [9].

Other transduction techniques have since been used to generate micro-scale rotational motion. Magnetic field-actuated reluctance motors are mature in the macro-scale, from which miniaturization has been accomplished [10, 11]. A typical magnetic micro-motor is capable of rotating at tens of thousands of rotations per minute, but is not feasible for use in large payload applications at the micro-scale. Piezoelectric ultrasonic micro-motors also turn a rotor continuously, usually with thin-film lead-zirconate-titanate (PZT) generating standing [12] (Figure 2) or traveling waves [13, 14] on the stator. Thermally actuated micro-motors [15] form another category that provides large actuation force when necessary. However, thermal actuation has considerable power consumption, complex transmission design, and slower response than other transduction mechanisms.

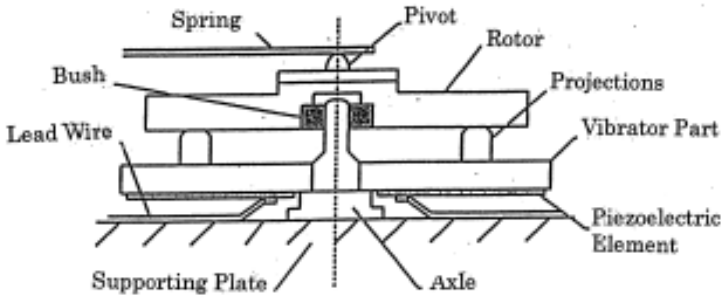

Figure 2 Cross-sectional view of ultrasonic micro-motor [12]

Magnetoelastic micro-motors (Figure 3 [8]) are designed to operate via magnetoelastic coupling, which is the interaction between material stress and strain and a magnetic field. This category of actuators operates at resonance under an external alternating magnetic field. Magnetoelastic micro-motors have the advantages of wireless power transmission, similar to other magnetic micro-motors, and large payload and energy transmission via contact dynamics between their stator and rotor. The contact dynamics for magnetoelastic micro-motors are similar to those of ultrasonic micro-motors, but have not been examined closely prior to this current work.

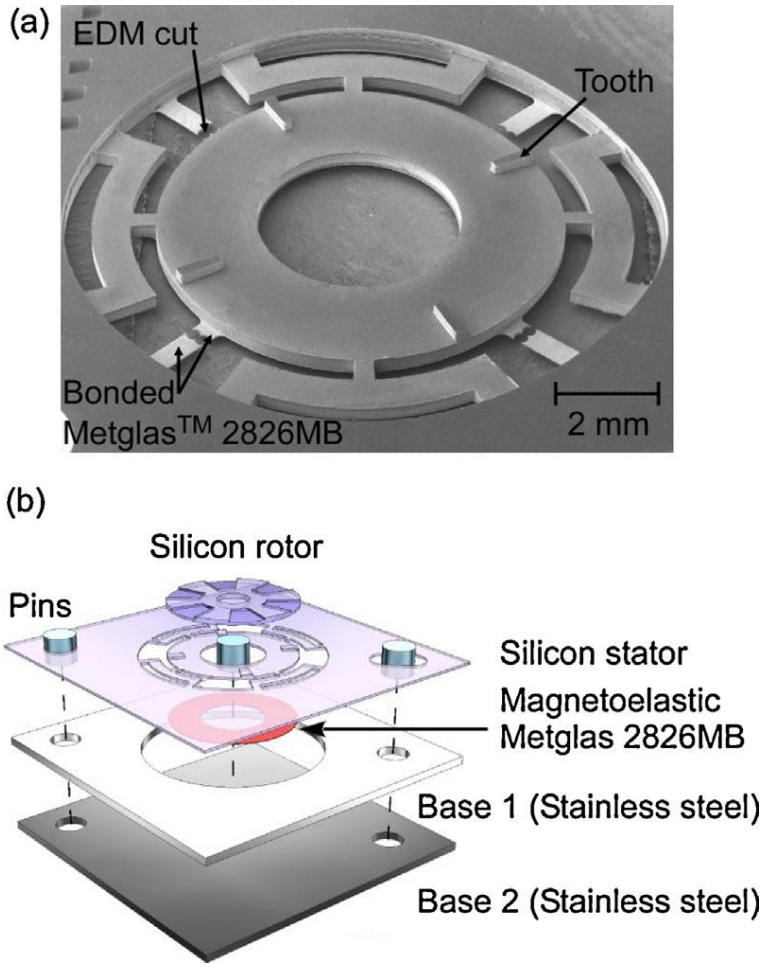

Figure 3 Prototypes of the magnetoelastic micro-motor (a) SEM of the stator layer; (b) schematic of the magnetoelastic micro-motor.

The dynamics of micro-motor are well developed for some of the other transduction mechanisms. Electrostatic micro-motors, as a large category, are actuated with non-contact electrostatic forcing [16-18]. This category of micro-motors is only considered to have contact dynamics between their hub and rotor and slipping friction between the rotor and supporting structure. Also, the electrostatic force locks the rotor into planar motion, eliminating out-of-plane displacements. The rotational motion of the rotor is modeled using the moment of inertia, air viscous drag, and nonlinear kinetic friction. Magnetic micro-motors are also designed to operate with non-contact force, and share similar dynamics with electrostatic motors [10, 11].

Piezoelectric ultrasonic micro-motors require mechanical contact to transmit energy from vibration to rotational motion of the rotor. The traveling wave-actuated ultrasonic micro-motors are more easily modeled due to their constant contact features between their rotor and stator, while standing wave-actuated micro-motors experience much more complex dynamics due to stochastically-distributed contact timing and off-axis motion. Different types of dynamic models for piezoelectric ultrasonic motors are previously published: 1) a dynamic model based on nonlinear stator-rotor interaction [19]; 2) a dynamic model based on the Rayleigh-Ritz mode energy model [20]; 3) a model with linearized impact force as a change in the stator's resonance [21]; 4) finite element models with the assumption of constant contact between rotor and stator [22, 23]. Drawbacks still exist in previous work such as neglecting the reaction force from rotor to stator [19]; neglecting off-axis shear and rotary inertia effects [20]; over-simplifying the stochastic contact dynamics[21]; and assuming only constant contact for traveling wave micro-motors [22, 23].

The magnetoelastic micro-motors are newly developed, so the dynamic model of this type of devices is still in development. Magnetoelastic micro-motors have a complex dynamic performance that is not identical to any of the prior types of rotary micro-motor. In brief, the vibration of the stator moves teeth in two directions. The teeth are silicon structures fabricated on the stator with high aspect ratio. To transmit vibration from stator teeth to rotor, impact dynamics are critical to calculate the relative dynamic states of both stator and rotor. Though similar to piezoelectric ultrasonic motors, some key differences exist. For one, the actuation resonance for magnetoelastic materials is much lower than piezoelectric materials because of the difference in elasticity properties. Lower actuation frequency emphasizes the importance of each impact contact between the stator and robot. Second, unlike actuation with piezoelectric material underneath the rotor on a comparatively rigid substrate, the stator of a magnetoelastic micro-motor is actuated with an external alternating magnetic field. The much greater relative compliance of such a magnetoelastic stator increases the importance of understanding the stator resonance based on structural geometry and material properties. Rotational motion is then determined by the influence of a collection of compliant stator impacts on the rigid rotor. The air viscosity, via squeeze film damping, affects the rotor dynamics as well.

1.1.2 Micro-robots

The micro-motors described above are used for generating micro-scale rotational motion, achieving large rotation angles via repeated small actuation motions. Mobile micro-robots, as another category of MEMS devices, are able to generate not only rotational motion, but also translational motion, again accumulated from many small actuator displacements.

The diversity of micro-robots has been increasing in recent decades as different micro-technologies improved fabrication possibilities. At the millimeter-scale, micro-robots share potential advantages of other MEMS devices such as low unit cost, low power consumption and small size. Early micro-robots can be tracked back to the 1990s [24]. This micro-robot with a footprint about 1 mm^2 was able to move at around 2 mm/s. No actuators were built on the robot; rather, the robot was actuated by external vibration. Micro-robots with many other types of locomotion have been developed over the decades since. Walking [25], swimming [26, 27], flying [28, 29], jumping [30, 31] and many other locomotion [32] ideas are employed to move these devices at the micro-scale. Candidate actuation methods for both micro-motors and micro-robots are similar, drawing from common MEMS transduction mechanisms such as electrostatic, magnetic, piezoelectric and electrothermal transduction, among others.

Walking robots form a major category of terrestrial robots. Walking micro-robots have the potential to fulfill many on-field applications, such as rescue and tactical missions, because they can carry reasonable payloads at small scale. Walking locomotion is potentially more predictable and controllable than jumping and hopping. Also it is more suitable than other terrestrial locomotion such as wheeled driving for overcoming small-scale obstacles and exploring complex terrain [33].

Several attempts have been made to create walking robots at the micro-scale. These attempts are grouped into those powered by external actuation versus those containing internal actuation. External actuation bypasses the consideration for either onboard power or wired power transmission and wire effects on robot dynamics, but a

specific working space or surface is required which limits the applications of this type of micro-robot. Internal actuation enables micro-robots to potentially operate in a large diversity of environments, but internal actuation design with actuators on-board requires a more complex design process and enhances fabrication difficulties.

As an example of external actuation, one passive micro-robot was built to be placed on a piezoelectric vibrator. With proper dynamics design, the robot legs with difference resonance could be actuated by external vibration, to move the micro-robot on the vibrator plane. The micro-robots [24, 34] designed with external vibration actuation always include at least one support leg. The support legs constantly contact with ground while other kicking legs overcome the friction force between support legs and ground to produce locomotion. The kicking legs are actuated near resonance to assure a high efficiency with a given external vibration amplitude.

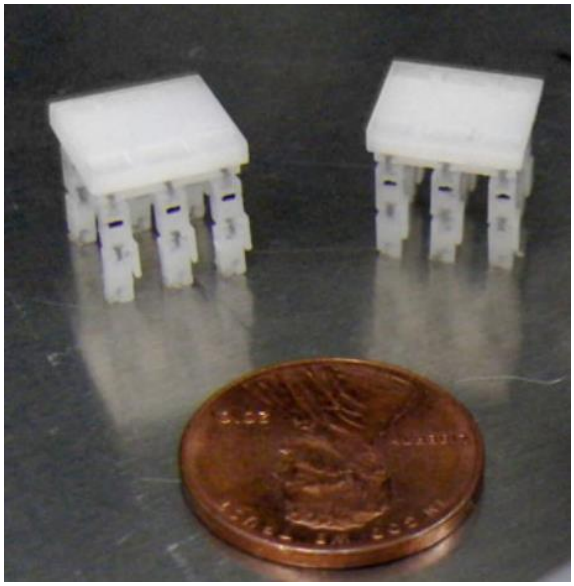

Figure 4 Micro-robots for use with an external alternating magnetic field [35]

Another external actuation principle is that of magnetic field-actuated micro-robots [35-37]. This category of micro-robots (Figure 4) interacts with an external magnetic field using magnetic materials. These magnetic materials with simple geometry also help simplify the modeling process for robot dynamics. However, magnetic micro-robots are to date designed with single actuators because multiple actuators in the same

magnetic field could not only provide no more actuation independence during operation, but also increase the design complexity.

Electrostatic actuation also could operate micro-robots without any wires [38]. The actuation is realized by the electrostatic coupling between the ground plane and the micro-robots. Two components on board are attracted to ground under different threshold voltage. This difference equips the micro-robot with four different static states. By actuating different states, the robot is able to move forward and turn in a single direction. This principle has similar drawbacks as external magnetic field actuation, as it could not be actuated with selectivity and requires special ground conditions.

As has been seen above, getting rid of wires connected to micro-robots through use of external actuation principles may be useful in some applications, but the external actuation limits micro-robots' walking range. A vibration table underneath, multiple coils closely-space around the micro-robots, or a ground with high AC voltage signal are necessary during testing for the respective robots described above.

To satisfy a broader range of potential micro-robot missions, a more general architecture is to design multiple actuators on board to move a micro-robot against friction between the micro-robot and ground. In this scenario, the payload is a major consideration because the weight of the power unit may be substantial when compared with the mass of the robot structure and actuators. Common actuators that transfer electric energy to force and displacement are electrostatic actuators, electrothermal actuators and piezoelectrical actuators. Electrostatic actuation is broadly used in MEMS devices as an actuation principle. However, its disadvantages are very limiting for micro-robots. It is challenge to achieve vertical motion with simple a fabrication process. Also, the nonlinear relationship between displacement and force for electrostatic actuators limits both actuation force amplitude and displacement range. Finally, very high voltage can be hard to achieve on an autonomous robot. Therefore, limited efforts are committed to this actuation principle for micro-robots [39-41]. One major exception, shown in [41], used almost half of its footprint to actuate just two single degree-of-freedom legs, using tens of electrostatic comb-drive actuators.

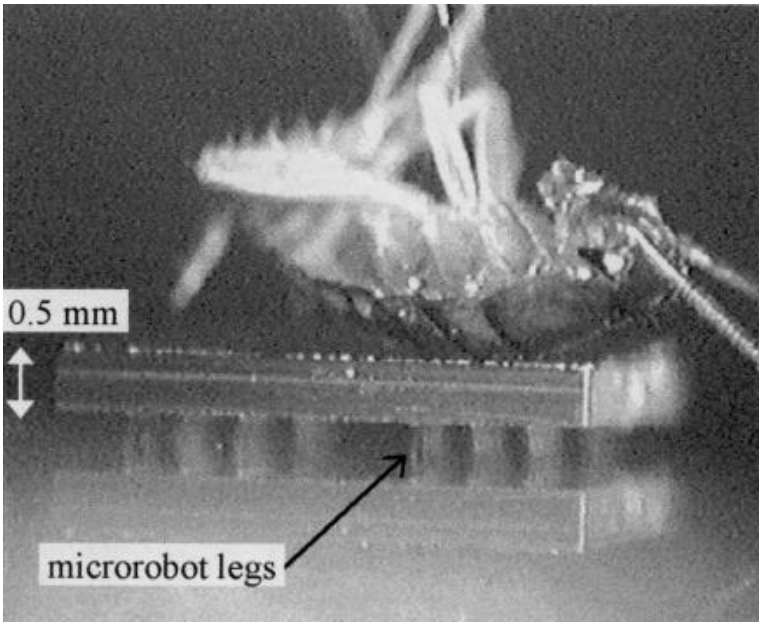

Figure 5 Electrothermal micro-robots with an insect as payload [42]

Electrothermal actuation uses electrically-heated thermal expansion to actuate devices. With proper design, this principle can provide large displacement with reasonable actuation force for micro-robotic applications. Electrothermally actuated micro-robots [25, 42, 43] are usually designed with multiple groups of legs integrated with actuators (Figure 5). Compliant joints connect the legs and the robot body, providing motion of a single degree of freedom each. Groups of legs are actuated with different signals, two groups of legs, as an example, actuated with inputs out-of-phase. Then, the micro-robots walk in a pattern close to the locomotion of some walking insects. Design emphases are the reliability of joints connecting the legs and body and the threshold friction force. These micro-robots tolerate large payloads, tens of their weight. However, the large power consumption that generates the temperature difference in the actuators limits the opportunity for further integration of battery or wireless power receiving systems.

Figure 6 Prototype of hexapod micro-robots with piezoelectric actuator and polymer structure.

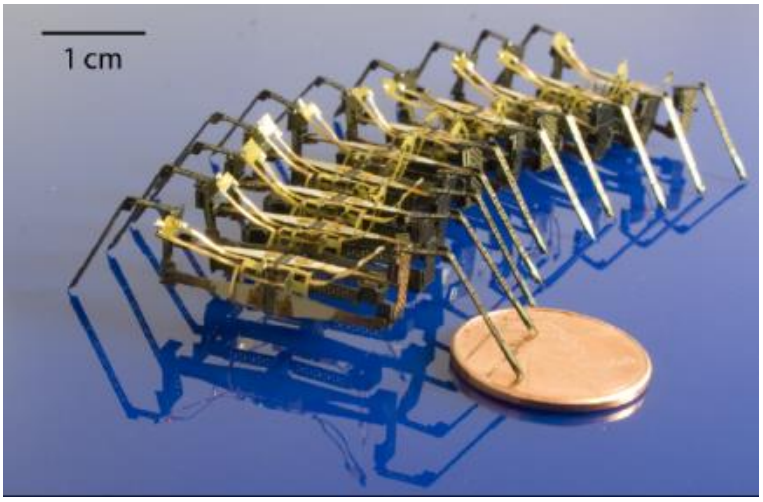

Figure 7 A myriapod millirobot with passive undulatory gaits ([44], [2011 IEEE])

Piezoelectric actuation has the advantages of excellent work and energy density. This feature is important when the payload of micro-robots is limited by its mechanical design. For example, piezoelectric actuation has even been applied to flying micro-robots [28]. Those micro-robots have piezoelectric actuators driving thin structures to move air and lift the robot. Walking micro-robots [45-47] with piezoelectric actuators are also addressed in some previous research (Figure 6 and Figure 7). As disadvantages, thin-film piezoelectric materials, most commonly lead-zirconate-titanate (PZT) [47, 48] are typically brittle when fabricated with micro-technology and difficult to integrate with other microstructures. To improve the performance of thin-film PZT, polymer materials

[47, 48] are chosen as coatings, reinforcing the piezoelectric bending beams and introducing additional compliant elements in more complex designs. A piezoelectric micro-robot prototype designed with polymer joint mechanisms is shown in Figure 6. Other smart materials such as shape memory alloy [49, 50] have also been tried for micro-robot actuation.

The dynamics of walking micro-robots are important for design, sensing and control of robot locomotion. However, the dynamics of micro-robot locomotion vary dramatically based on actuation principles and robot design. External vibration actuation requires support legs to constantly contact with ground. Then, the dynamics of this category of micro-robots can be simplified to a lumped mass-spring-damper system[24]. Operating at structural resonance of micro-robots benefits the robot efficiency, which is important under low power budgets. Resonant behavior can be derived from lumped element systems, or from finite element analysis [34] when the geometry is more complex.

The contact dynamics for micro-robots actuated by external vibration are not well studied in previous work [24, 34]. External magnetic field-actuated micro-robots always require simple geometry, so a rigid body model [37] was accurate enough to describe the dynamics. For some micro-robots with spring structures, finite element analysis helps to estimate the structure resonance[36]. Externally-driven electrostatic robots also rely on a simple geometry. [38] showed quasi-static states are used to control the forward motion and turning of a flat robot. Likewise, both external magnetic [36, 37] and electrostatically [38] actuated micro-robots have been considered to be quasi-static for each locomotion state. Friction is critical for motion, but foot impact contact dynamics are neglected for all cases.

Unlike externally actuated micro-robots, the stick and slip principle is the most common basis for motion of electrothermally-actuated micro-robots [25, 42, 43]. With a single degree of freedom in electrothermal actuation, multiple groups of legs are distributed in either slip state or stick state. This locomotion principle also could be simplified to be quasi-static. For each leg, its state could be either on or off when the voltage is applied or not.

Piezoelectrically actuated micro-robots [45-47] are potentially the best candidate for versatile robotic operations with large work density, reasonable actuation force, and the potential to be integrated with entire power, sensing and control systems on board. The I-Swarm project [46] developed small, piezoelectrically actuated robots to study swarm control strategies and swarm performance but with limited modeling of individual robots. The myriapod millirobot [44] emphasizes undulatory gaits and studied robot dynamics with Euler-Lagrange methods. The millirobot is simplified for representation as an assembly of rigid beam structures and springs to derive the dynamic equation from energy conservation based on lumped element assumptions.

Works [45, 48] describe piezoelectric micro-robot designs having compliant actuators or legs and relatively rigid bodies based on thin-film piezoelectric and polymer structures. The rigid chassis enables micro-robots to carry future power, sensing and control units. The compliant mechanism of piezoelectric actuators integrated with polymer flexures enables relatively large actuation amplitudes around structural resonances. These actuators can also generate coupled motion in multiple directions. This type of hybrid system, including both continuous compliant structures and rigid body structures, can be a challenge for dynamics modeling, especially in the presence of contact dynamics. The complexity of dynamic modeling is increased by the nonlinear contact dynamics between robot feet and ground at the micro-scale. The contact dynamics for this micro-robot plays a more critical role when compared to other micro-robots because of the high contact frequency, micrometer-scale contact area and multiple degrees of freedom for interaction with ground. Also, air damping reduces the robot in-air time, and changes the forward motion speed.

1.1.3 Similarities between micro-motors and micro-robots

Several similarities are shared between the dynamics of micro-motors and micro-robots: importance of contact dynamics, existence of compliant mechanisms with contributions from rigid body motion, and effects of fluid viscosity. Ultimately, the magnetoelastic micro-motors and piezoelectric micro-robots are both designed on the basis of actuation schemes to generate motion via contact dynamics.

Contact dynamics: Contact dynamics are relevant to many MEMS devices such as switches [51], probes [52] and micro-mirrors [53]. Some relevant research has been published addressing limits for MEMS devices designed for motion in the presence of contact. The majority of these researches are focused on the statistical contacts [54, 55]. For contact dynamics, works include single degree of freedom models [56], single parameter comparisons [57, 58] and time-domain comparisons based on single inputs [59]. Contact dynamics have also been studied in micro- and meso-scale previously for micro-robots in our group [60-64].

Fundamentally, micro-scale contact dynamics are dictated by atomic forces at a solid interface that behave as an adhesion and/or contact force. The complexity of these contact dynamics arises from short contact times and low energy interactions. Contact surface geometry, electrostatic force, adhesion effects and squeeze film damping all come into play for micro-scale impact [61]. High frequency impact at the micro-scale is also prevalent compared to macro-scale system, with different combinations of effects being most important in different circumstances.

The modeling of contact dynamics is similar but not identical for the devices studied here: magnetoelastic micro-motors and piezoelectric micro-robots. A simple coefficient of restitution is enough to capture the effects of meso-scale contact for the magnetoelastic micro-motors, but not always sufficient for the piezoelectric micro-robots. This difference is caused by the amount of contact area and contact component scale, which is in the millimeter range for the micro-motor but micrometer range for the micro-robots.

Compliance: The resonance of compliant actuators is important for achieving efficient actuation under power budget constraints. Modeling compliant actuators can be done based on finite element analysis and/or theoretical derivations. However, both methods are not always in agreement with experimental results because of limited fabrication resolution, material property variance, and aging. Empirical identification of resonance is often necessary for better actuation efficiency and control algorithm design. Modeling multiple modes helps to understand both the bidirectional motion for micro-motors and the high order resonance influence on the micro-robots. Furthermore, the

variance of resonance also causes a non-uniform influence from actuators to the rigid body, rotor or chassis.

Rigid body motion: Rigid body motion is the simplest feature to be modeled for both micro-motors and micro-robots, though it appears at different locations in the two structures. Complexity can still be amplified by the number of contact points, from rotor to teeth for micro-motors, and from central chassis to legged actuators for micro-robots. The primary motion, rotation for motors and forward motion for robots, along with the off-axis motion require the rigid body to be modeled in multiple degrees of freedom.

Air damping: Fluid viscosity slows down the primary motion of both micro-scale devices. Squeeze film damping and the air viscous force are necessary to accurately model the behavior of both micro-motors and micro-robots. These forces are geometry- and velocity-related, which makes them nonlinear in modeling.

2.1 Problem Statement and Tasks

The complexity of micro-scale dynamics is affected by many different factors. The major task is to determine the dominant effects to the dynamics and the influence from different parameters to the final motion of the device. The benefits of dynamic modeling of micro-motors and micro-robots, as an example of hybrid micro-systems, include: 1) ability to aid device design with numerical analysis; 2) ability to design sensing algorithms to monitor motor and robot motion and the external environment; 3) ability to test and/or be integrated with novel control strategies using a dynamic simulation model.

The research objective of this work is to establish dynamic modeling procedures, along with empirical system parameter identification and/or modification, for micro-scale devices with a combination of elastic and rigid elements and contact dynamics. As discussed above, micro-motors and micro-robots are examples of this class of micro-scale

devices. The component mechanism includes contact dynamics, compliant mechanism, rigid body motion and fluid viscosity. The modeling procedures have the ability to consider the interaction between components with different mechanisms in the devices, and also the interaction between device components and their environment via contact and viscous forces. The modeling procedures also need to consider multiple modes for compliant components and multiple degrees of freedom for rigid body components.

As introduced in background, the dynamics of magnetoelastic micro-motors have not been studied previously. The previous work on the dynamics of other types of micro-motors cannot provide numerical analysis of the whole dynamic performance of a micro-motor from actuation signal to final rotational motion including all dynamics behaviors. A dynamic model of micro-motors, as an integration of all dynamics of/between different components, can help for designing sensing algorithms and control strategies for better tracking of motor motion. The objective of this study is also to identify trends of motor rotational motion based on different actuation conditions and design parameters. Therefore, the first task of this work is to model a magnetoelastic micro-motor, including: 1) modal analysis with multiple resonance of the compliant stator and the dual directional teeth motion; 2) rigid body analysis of rotor with two degrees of freedom, vertical and rotational motion; 3) interaction between rotor and stator with transient motions for both components; 4) squeeze film damping caused by the air trapped between stator and rotor. The extensive work of this task is to design a sensor schematic to track the rotation, with an estimator designed based on the understanding of system dynamics.

The second task of this work is to model the dynamics of a legged walking micro-robot actuated by piezoelectric actuators with polymer reinforcement structure. Dynamics of a micro-robot with compliant actuators and rigid chassis in multiple degrees of freedom have not been studied before. The objective of this study is to identify the trends of robot forward motion based on different actuation conditions and design parameters. The challenge of this task is to include all following dynamic behaviors in a single model: 1) multiple modes of piezoelectric actuators with empirically verified properties and coupled motion in two directions at the end of actuator; 2) rigid body analysis of the robot chassis with 3 degrees of freedom at minimum (vertical, forward and

turning motions); 3) interaction between the robot chassis and multiple legs with transient motions for all components; 4) air viscosity at micro-scale. The dynamic model of a micro-robot is first validated with small-scale robot prototypes. These prototypes have similar characteristics as their micro-scale partners. Prototypes are actuated with piezoelectric actuator embedded with polymer materials, to generated dual directional coupled motion. A relatively rigid chassis of prototype is moved by multiple actuators. Prototypes are designed at different scales to study the scaling effect.

The third task of this work is to extend the dynamic model for robot locomotion to a millimeter-scale walking micro-robot. Hexapedal millimeter-scale micro-robots were fabricated to characterize robot parameters and validate the micro-robot locomotion and dynamic model. The micro-robots are formed from silicon with integrated thin-film lead-zirconate-titanate and high-aspect-ratio parylene-C polymer micro-actuation elements. The challenges of this task are to: 1) characterize the time-domain and frequency-domain response of the robot when electrical actuation is provided through the suspension structure on the chip; 2) extend the validated small-scale dynamic model with micro-scale phenomena such as adhesion and air-damping; 3) validate the dynamic model with a detached micro-robot, which has no power supply, using an external excitation approach. The time- and frequency-domain response at several locations of the micro-robot is characterized, to study the mode shape of the micro-robot at different frequencies. After the detachment of the robot, external vibration is provided to move robot in a testing bed, to validate the dynamic model modified from small-scale and considering external actuation.

After we have an overall understanding of the robot dynamics in small scale, the fourth task of this work is to study the benefits of the understanding of robot dynamics. The first objective is to develop an optimization algorithm based on the dynamic model and on-board sensing, to evaluate whether an on-board sensing is advantageous and to what extent on-board sensing should be provided to enhance robot locomotion. The challenges of this work are to search for and realize power-efficient sensing approaches on the robot and to develop algorithms that can optimize robot performance with and without on-board sensing information. The other objective is to discover other potential

locomotion gaits of the micro-robot designed for planar fabrication with thin-film piezoelectric materials and polymer structures. This study can help to evaluate any other potential locomotion in the micro-scale and to build a design approach that can use centimeter-scale fast prototyping techniques for micro-fabricated robot validation. The challenge is to extend the locomotion of existing robots to different actuation conditions for the same robot, and to explain and predict additional locomotion behaviors with this understanding of robot dynamics.

CHAPTER 2 Dynamic Modeling of a Bidirectional Magnetoelastic Rotary Micro-Motor

2.1 Introduction

Chip-scale rotary micro-motors based on magnetoelastic transduction have recently been demonstrated [8]. These motors join other transduction mechanisms for realizing chip-scale rotary motion, including electrostatic, piezoelectric and others [9, 65]. In general, micro-motors based on smart materials and fabricated by MEMS technology have demonstrated better efficiency than chip-scale versions of traditional electromagnetic motors [65].

Chip-scale rotary micro-motors are useful in a broad range of applications [66-70]. One emerging opportunity is to integrate rotary motion with a MEMS gyroscope and control electronics to realize on-chip calibration of long-term gyroscope gain and bias drift [1, 71]. However, such an application requires exceptionally high motion accuracies; a representative gyroscope calibration requirement is rotation at up to 1000 degree/s over arbitrary angles with a resolution better than ±10 milli-degrees. To reach such accuracy, the dynamic behavior of a micro-motor must be well understood and distilled into an analytical or numerical model. A model that captures essential behaviors, including transient and steady-state stator motions, stator-to-rotor momentum transfer mechanics, and energy loss mechanisms, is important for predictive design. Such a model is also needed for improving motion estimation accuracy using Kalman filters or other estimation and control schemes. This chapter describes the first detailed dynamic modeling of a rotary micro-motor based specifically on magnetoelastic excitation.

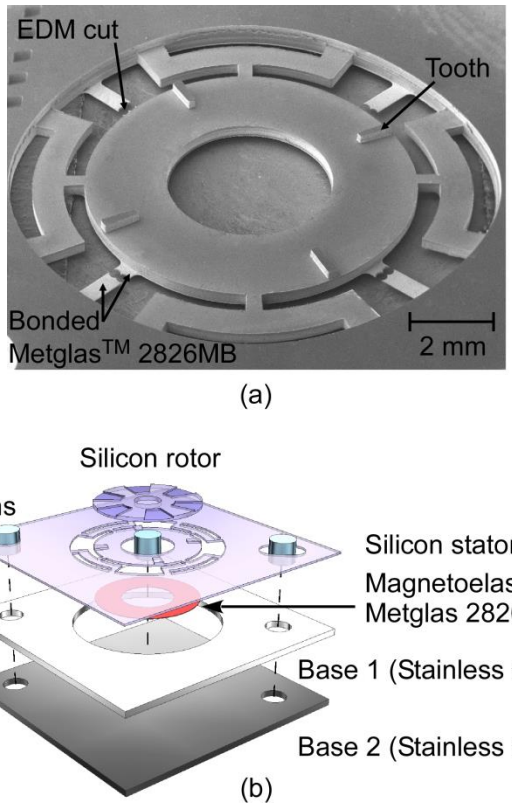

Figure 8 Prototypes of the magnetoelastic micro-motor (a) SEM of the stator layer; (b) Schematic of the magnetoelastic micro-motor.

Magnetoelastic rotary micro-motors [8] can be driven with a larger payload than other motors at the same scale; this feature is helpful for carrying on-chip gyroscopes for calibration. Magnetoelastic motors can also be remotely, wirelessly actuated without coupling circuitry. The direction of rotation is selected by changing the electromagnetic field input frequency between well-defined resonant modes. The model presented in this chapter focuses on a micro-motor designed for the *in situ* gyroscope calibration task described above. Figure 8(a) shows a scanning electron microscopy (SEM) image of a magnetoelastic micro-motor stator and Figure 8(b) shows the schematic of the device.

Many studies have been completed on rotary micro-motor dynamics based on other transduction mechanisms. Electrostatic micro-motors [9, 72], for example, have been extensively studied [16-18]. These motors are actuated through non-contact interactions that are significantly different from the stator-rotor interaction in a

magnetoelastic micro-motor. Piezoelectric micro-motors are more closely related, being based on contact between stator and rotor, as in the magnetoelastic motor. Many piezoelectric motor models have been proposed; types of these models include: 1. Dynamic models based on nonlinear stator-rotor contact, without considering the reaction of the stator to contact with the rotor [19]; 2. Models based on the Rayleigh-Ritz assumed mode energy method, without considering shear and rotary inertia effects [20]; 3. Models applying a linearized impact force as a change in the stator's vibration frequency [21]; 4. Finite element methods applied by assuming the stator and rotor are in constant contact [22, 23]. The piezoelectric micro-motors described were all designed for travelling wave actuation, which eases control. More recently, nonlinear dynamics of rub-impact-actuated micro-motors have been studied via classical impact theory and dry friction models; however, to date these studies are without experimental validation [73, 74].

While both piezoelectric ultrasonic and magnetoelastic motors are actuated by high frequency stator vibration, which makes contact with a rotor, the two most prominent differences are: 1) the forcing mechanism is magnetoelastic rather than piezoelectric, thus relying on in-plane magnetic fields rather than through-the-thickness electric fields, and 2) the suspended nature of the magnetoelastic stator along with the high intended payloads means that the stator motion – not just the rotor motion – is substantially affected by contact interactions. As a result, considering both the driving magnetostrictive force and the stator-to-rotor impacts from the stator perspective can give a better prediction of motor motion than existing micro-motor models. Thus, a model accounting for linear and angular momentum transfer during the contact process has been developed. This is coupled with the rigid body dynamic response of a rotor to model the complete magnetoelastic motor behavior. In the present work, this coupling is analyzed for a standing wave in the stator, which also varies from most prior rotary motor models. Modeling results are presented under various design and operating parameters, and compared to experimental results for a prototype motor.

2.2 System Description

2.2.1 Device architecture and actuation concept

The micro-motor consists of the following key components (Figure 8): a stator (with four teeth located on the top surface), a rotor, and a hub. The stator is suspended in a recessed base that allows stator vibration and provides locations for alignment pins and the hub. The stator is a flexible structure that includes a layer of magnetoelastic material, the component driven by the magnetic field directly. For best response, the driving magnetic field should be oriented in the same plane as the magnetoelastic layer. The teeth on the stator transfer energy from stator vibration into the rotation of the rotor. The ring-shaped stator is suspended by four crab-leg springs, which are stiff in the rotational direction but flexible in the out-of-plane direction; these prevent stator rotation during rotor actuation while allowing large vertical deformation required for actuation. The rotor may rotate arbitrarily large angles about the hub, while the hub limits the lateral and/or vertical motion of the rotor.

The generation of rotary motion is similar to that for piezoelectric ultrasonic rotary motors [12]. A vibratory wave, either a standing wave (as in this work) or a travelling wave, is generated in the stator. The resulting vibratory mode shape of the stator has antinodes at which maximal out-of-plane deflection occurs. For the standing wave motor, the teeth are located on the stator such that they are offset from the antinodes, resulting in tangential and vertical motion of the teeth tips. In the design presented, the suspension has two useful modes with different resonant frequencies and antinodes separated by 45º. By selecting either resonant frequency when driving the stator, the tangential direction of the teeth oscillations may be switched, thereby reversing the rotation. When the stator is driven magnetoelastically, a series of collisions between the teeth and the rotor occurs. Because the teeth are moving both vertically and tangentially, each collision will, in general, impart both a vertically-oriented and a tangentially-oriented impulse force between the contacting teeth and the rotor. Tangential motion from a pair of opposing teeth results in rotation about a central hub, while the vertical motion of the rotor resembles rigid body ballistic motion between collisions. Meanwhile, the impulse force delivered to the stator by the collisions results in a transient dynamic response superposed with the steady-state resonant response.

2.2.2 Device fabrication

Magnetoelastic motors to be modeled were fabricated by Dr. Jun Tang based on designs developed by Dr. Tang and Dr. Scott Green. The stator and rotor are fabricated side-by-side from a 350 μm thick silicon wafer using a two-mask deep reactive-ion etching (DRIE) process. At the end of this process, the ring-shaped stator is fully etched out, and the teeth are defined on the top surface of the stator. The silicon rotor has a through hole at the center for placement on the hub.

The magnetoelastic layer is batch-patterned using photochemical machining (PCM) [75] from Metglas™ 2826MB foil, a nickel-iron-molybdenum-boron alloy with desirable magnetostrictive properties [76]. The ring-shaped stator is patterned with an inner diameter of 4 mm and an outer diameter of 8 mm, and with a thickness of 25 μm. The ring is held in a frame by simple connecting tethers. The recessed base is formed using two layers that are also fabricated using PCM from 0.5 mm thick stainless steel foils.

The patterned Metglas™ 2826MB foil is bonded to the silicon stator using Au-In transient liquid phase bonding (TLP) [77, 78]. After bonding, the connections between the ring and frame in the Metglas™ 2826MB layer are cut using micro-electro-discharge machining [79]. An SEM image of the silicon stator with bonded ring-shaped Metglas™ 2826MB is shown in Figure 8 (a). As the final step before testing, the silicon stator, stainless steel bases, and a hub (ø2 mm stainless steel pin) are aligned, stacked and fixed to each other with epoxy. The silicon rotor is placed directly above the stator and is constrained by the hub while touching the stator only at the teeth.

2.3 Dynamic Rotary Motor Model

2.3.1 Modeling Approach and Setup

Modeling Method

To understand and predict the dynamic motion of the motor, both a parametric modal model (PMM) and a finite element model (FEM) are used. The PMM is based on geometric parameters and physical properties of the stator and rotor (certain of which must be measured experimentally), which can be used to predict the dynamic motion of the motor. The PMM captures the major features of the motor motion, and is especially useful in simulating long durations of operation with many stator-to-rotor collisions, and is the focus of this chapter. The FEM is based on a COMSOL Multiphysics model developed by Dr. Scott Green, and was used to predict additional behavior of the stator, including mode shapes, driven stator amplitude, and residual deformation from fabrication processes.

Flow of the Parametric Modal Model

The flow chart (Figure 9) of the model summarizes how the dynamic model operates. The first step is to determine the parameters of the device (geometrical parameters, modal frequencies, damping factors), and then initialize the model. Subsequently, in each step, the motions of the rotor and stator are estimated by a transient model until a collision between the stator and rotor is determined to occur. If a collision occurs, the states after collision are calculated. If these states are such that rotor and stator separation occurs, transient motion is again calculated until the next collision point. If the states indicate that no separation occurs, further instantaneous collisions are simulated until separation does occur.

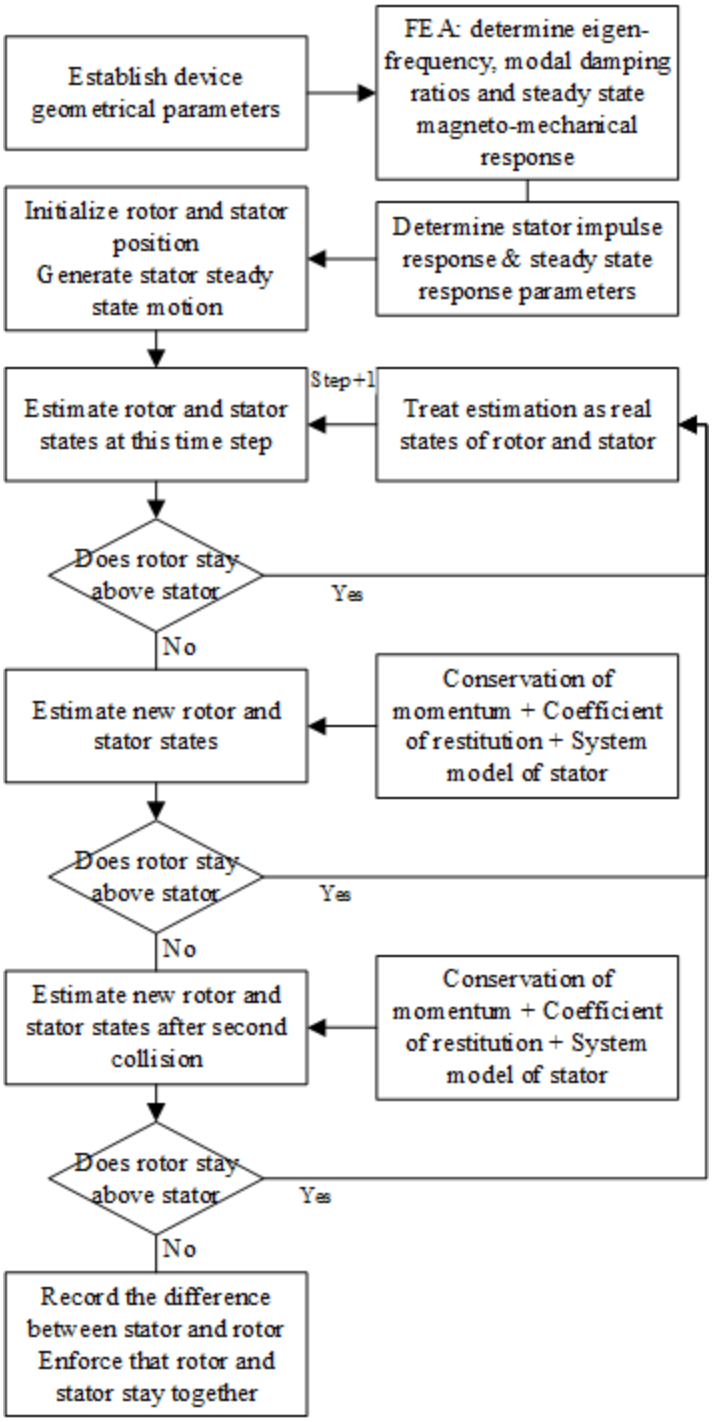

Figure 9: Flow chart of the dynamic model

PMM Assumptions

In addition to information from the FEM, the following assumptions are made in deriving the dynamic PMM:

1. Teeth are treated as rectangular bodies with a negligible moment of inertia.
2. Collisions occur at the inner edges of the teeth.
3. During contact, slippage could occur between the teeth and the rotor. If slippage is calculated to occur (based on the contact angle), the tangential force is proportional to the normal force (i.e. a dry Coulomb friction model).
4. A pair of teeth, each tooth located on opposite sides of the stator, collides with the rotor at the same time with identical velocities. (Some randomness in the vibration amplitude of each pair of teeth will later be introduced to account for non-uniformity of the fabricated system.)
5. The mass distribution of the stator is uniform.
6. The damping coefficients and spring rates of the stator are mode-dependent constants.

Variable Definitions

Variables used in the dynamic PMM are introduced here (Figure 10). First, the velocities of the stator teeth, denoted by subscript *s*, and rotor, denoted by subscript *r*, are defined as shown in Figure 28, in tangential (θ) and vertical (z) directions. Velocities before collisions are further denoted by subscript *o*, after collision by subscript *f*, and in steady-state (no rotor or collisions) by subscript *ss*. Four different forces are defined. F_f is the friction between the stator and rotor in the tangential direction and F_n is the normal force between the stator and rotor in the vertical direction. f_m is the magnetic force acting on the stator, generated by the coils, resulting in the out-of-plane driven stator motion. f_i is the impulse force, and appears only when a vertical collision occurs between the stator and rotor. In this case, $F_n = f_i$. Finally, $u(\theta, t)$ is defined as the distributed vertical displacement of the stator as a function of time (t) at the angular position on the stator (θ).

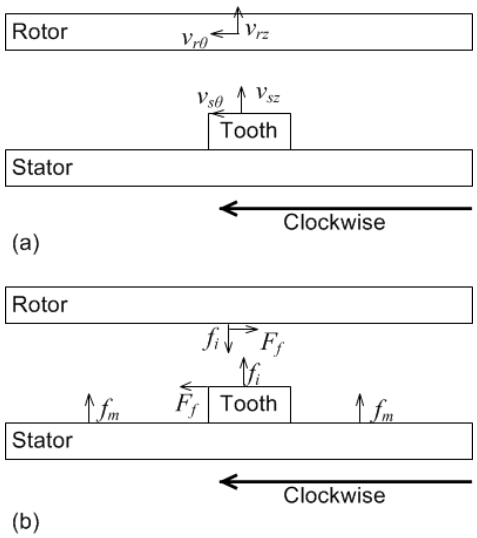

Figure 10: (a) Velocity definitions and (b) forces acting on the micro-motor.

Stator geometry and dynamics

Geometric parameters describing the stator are illustrated in Figure 11. These include stator radii (inner, R_i, outer, R_o, and inside of teeth, R_t), and tooth angular locations, θ_t. The teeth are offset from the locations of maximum motion for both actuation modes, so that the teeth will move in opposite directions in the two actuation modes.

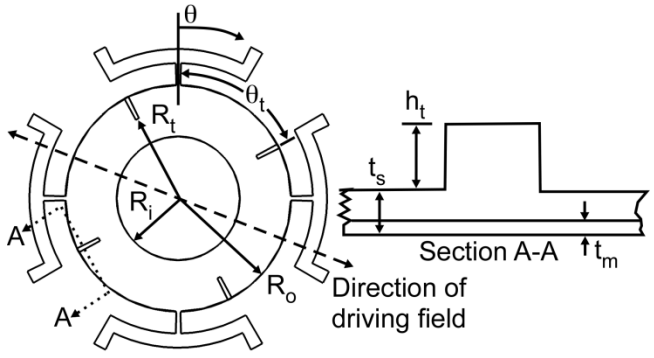

Figure 11 Stator geometry and key dimensional parameters.

2.3.2 Dynamic Model Derivation

FEM results: Resonant mode shapes, static deformation and mode misalignment:

The dynamic PMM is based on a stator undergoing a magnetoelastically-driven standing wave, with transient effects introduced by impact events with the rotor. Via the applied magnetic field or as a result of collisions between the teeth and the rotor, different vibration modes can be excited (Figure 12). The excited mode with the lowest frequency, referred to as mode A in this chapter, is a pseudo-rigid-body motion of the entire stator ring. The magnetolastically-driven modes are those used to generate the rotary motion and are referred to as modes B and C in this chapter. Two other tilting modes exist between mode A and modes B and C; however, these are not strongly excited by the symmetric collisions and driving magnetic field. In the prototype micro-motor studied, mode B occurs at about 6.3 kHz and has its maximum vibration position located between the suspension connections; this mode shape causes the rotor to rotate clockwise. Mode C occurs at about 7.4 kHz and has its maximum vibration position at the connections of the stator to the suspension; mode C causes the rotor to rotate counter-clockwise.

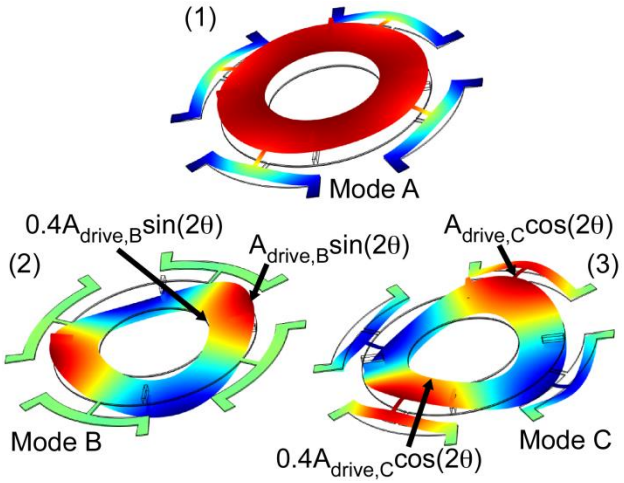

Figure 12 The modes of the motor: (1) pseudo-rigid-body mode (first mode, mode A); (2) first actuation mode (fourth mode, mode B); (3) second actuation mode (fifth mode, mode C) (Dr. Scott Green)

Stator Model

The stator is treated as a ring with uniform mass distribution. Once the inertia of the teeth is assumed to be negligible, it is reasonable to model the stator as a linear mass-spring-damper system with respect to angle (θ) and time (t):

$$m\ddot{u}(\theta,t) + b(\theta)\dot{u}(\theta,t) + k(\theta)u(\theta,t) = f_m + f_i \tag{3}$$

in which mass (m), damping coefficient (b), the spring constant (k), and both forces f_m (magnetic force from the coil) and f_i (impulse force from rotor) are given in units per angle. For example, m is defined as $\frac{m_s}{2\pi}$, in which m_s is the mass of the stator.

The stator displacement at the inner tooth radius (R_t) as a function of time and angle ($u(\theta,t)$) can be decoupled into a combination of the three previously described modes,

$$u(\theta,t) = g_A(t) + g_B(t)sin(2\theta) + g_C(t)cos(2\theta) \tag{4}$$

The actuation (magnetic) force can also be modeled over the two excitation modes as

$$f_m(\theta,t) = f_{mB}\, sin(2\theta)\, sin(2\pi f_B t) + f_{mC}\, cos(2\theta)\, sin(2\pi f_C t) \tag{5}$$

in which f_B and f_C are the actuation frequencies and either f_{mB} or f_{mC} (amplitude of the magnetic force) is set to be zero because only a single frequency will be used to actuate the device at any given time.

The interaction force between the stator and the rotor, acting on the stator, can be determined by linear momentum conservation at the rotor. Describing the impulse force f_i as force per angle, the expression for momentum transfer in the vertical direction from a collision between the rotor and stator is as follows:

$$f_i = -\frac{m_r(v_{rf}-v_{ro})\delta(t-t_c)}{2\Delta\theta} \tag{6a}$$

Here, the interaction force is placed at tooth position θ_t and determined by the rotor velocity before (v_{ro}) and after (v_{rf}) collision. $\delta(t-t_c)$ is the Dirac delta function defined to occur at the collision time (t_c). When wobble and tilting of the rotor are insignificant, the two teeth in each set are assumed to collide identically with the rotor. The interaction force is assumed to act on the entire arc length of the tooth in the angular direction at its lateral surface, occupying angle $\Delta\theta$. Therefore the force can be expressed

as a function of a pulse train having amplitude $-\frac{1}{2}m_r(v_{rf}-v_{ro})$ and spatial duty cycle θ and period π.

Expanding that spatial distribution of the interaction force in a Fourier series, the spatial distribution of the impulse force is a summation of a spatially independent term and an infinite number of terms that are circumferentially periodic. Thus, the only mode shapes that are excited by such a force are modes A, B and C as described previously, as well as higher order modes with an even number of antinodes. The terms relating to these higher order modes are neglected, as their high resonant frequencies result in negligible displacement amplitudes relative to modes A-C. The interaction force is thus reduced from (6a), for $\Delta\theta \ll \pi$, to:

$$f_i \approx -\frac{1}{2}m_r(v_{rf}-v_{ro})\delta(t-t_c)[\frac{1}{\pi}+\frac{2}{\pi}cos(2\theta)\,cos(2\theta_t)+sin(2\theta)\,sin(2\theta_t)] \quad (6b)$$

From the assumption that the damping coefficient (b) and the spring constant (k) are mode dependent constants, the second order linear equation of the stator can be decoupled into three second order linear differential equations in time, one per mode shape, with different damping coefficients and spring constants. Substituting (4), (5), and (6b) into (3) and decoupling:

$$m\ddot{g}_A(t)+b_A\dot{g}_A(t)+k_Ag_A(t)=-\frac{1}{2\pi}m_r(v_{rzf}-v_{rzo})\delta(t-t_c) \quad (7a)$$

$$m\ddot{g}_B(t)+b_B\dot{g}_B(t)+k_Bg_B(t)$$
$$=-\frac{1}{\pi}m_r\big(v_{rzf}-v_{rzo}\big)\delta(t-t_c)\,sin(2\theta_t)+f_{mB}\,sin(2\pi f_Bt) \quad (7b)$$

$$m\ddot{g}_C(t)+b_C\dot{g}_C(t)+k_Cg_C(t)$$
$$=-\frac{1}{\pi}m_r\big(v_{rzf}-v_{rzo}\big)\delta(t-t_c)\,cos(2\theta_t)+f_{mC}\,sin(2\pi f_Ct) \quad (7c)$$

The response of each equation can be superposed as the sum of responses under the magnetic force and interaction forces. The magnetic force produces the steady-state stator response to a second order linear equation and the interaction force response is the impulse response.

Solving (7), the steady-state motion in the vertical direction is:

$$u_{ss}(\theta,t) = \begin{cases} A_B sin(2\theta)\, sin(2\pi f t) & mode\ B \\ A_C cos(2\theta) sin(2\pi f t) & mode\ C \end{cases} \tag{8a}$$

in which A_B and A_C are the vertical steady state motion amplitudes.

Meanwhile, the vertical displacement response when collisions occur is modeled as the sum of the impulse responses of each mode shape (7a-c):

$$u_i(\theta,t) = \frac{2\pi F_n}{m_s \omega_{d,A}} e^{-\xi_A\, \omega_A t} \sin\left(\omega_{d,A} t\right) + \frac{4\pi F_n}{m_s \omega_{d,B}} e^{-\xi_B\, \omega_B t} \sin\left(\omega_{d,B} t\right) sin(2\theta_t) \sin(2\theta)$$

$$+ \frac{4\pi F_n}{m_s \omega_{d,C}} e^{-\xi_C\, \omega_C t} \sin(\omega_{d,C} t)\, cos(2\theta_t)\, cos(2\theta) \tag{8b}$$

in which, from integrating (6b) over time at $\theta = \theta_t$,

$$F_n = -\frac{1}{2} m_r (v_{rf} - v_{ro}) \frac{1}{\pi} \tag{8c}$$

and $\omega_n = 2\pi f_n = \sqrt{\frac{k_n}{m}}$, $\omega_{d,n} = \omega_n \sqrt{1-\xi_n}$, $\xi_n = \frac{b_n}{2m\omega_n}$, and n = A, B or C.

Likewise, the tangential response can be found as a combination of three responses. During vibration, the tooth tilts through an angle of amplitude θ_{tilt}. Because the vertical and the tangential motion of the tooth are related through the rigid geometry of the tooth, the tangential motions in the clockwise direction of the stator at the tooth position can be obtained from the derivative of vertical motion with respect to rotor angle ($\partial u/\partial\theta$), giving:

$$u_{ss,tangential}(\theta,t) = \left(\frac{t_s}{2}+h_t\right) sin(\theta_{tilt}) \approx \left(\frac{t_s}{2}+h_t\right)\frac{\partial u_s(\theta,t)}{\partial r\theta}$$
$$= \begin{cases} A_B \dfrac{(t_s+2h_t)}{r} cos(2\theta)\, sin(2\pi f t) & \text{mode B} \\ -A_C \dfrac{(t_s+2h_t)}{r} sin(2\theta) sin(2\pi f t) & \text{mode C} \end{cases} \tag{9a}$$

$$u_{i,tangential}(t)\left(\frac{t_s}{2}+h_t\right) sin(\theta_{tilt}) \approx \left(\frac{t_s}{2}+h_t\right)\frac{\partial u_i(\theta,t)}{\partial r\theta} =$$
$$\frac{4\pi F_n}{m_s \omega_{d,B}} \frac{(t_s+2h_t)}{r} e^{-\xi_B\, \omega_B t} \sin\left(\omega_{d,B} t\right) \cos(2\theta_t)$$
$$-\frac{4\pi F_n}{m_s \omega_{d,C}} \frac{(t_s+2h_t)}{r} e^{-\xi_C\, \omega_C t} \sin(\omega_{d,C} t)\, cos(2\theta_t)\, sin(2\theta) \tag{9b}$$

2.3.3 Collision model

To complete the collision model, the coefficients of restitution and friction are defined.

Coefficient of restitution: The coefficient of restitution is defined as the ratio of the relative velocity in the normal direction after collision to the relative velocity in the vertical direction after collision:

$$e = \frac{v_{rzf} - v_{szf}}{v_{szo} - v_{rzo}}. \tag{10}$$

Coefficient of friction: A dry (Coulomb) friction model is assumed making the relationship between the (vertical) normal force (F_n) and the (tangential) friction force (F_f)

$$F_f = \begin{cases} \mu F_n & if\ \mu < \tan(\alpha) \\ tan(\alpha) & if\ \mu > \tan(\alpha) \end{cases} \tag{11}$$

in which μ is defined as the coefficient of friction, and α is the angle between the vertical direction and the interaction force acting on the rotor. The α at each collision is defined as the ratio of the tangential and vertical displacement of the stator at the tooth position.

Alternative friction models were also considered [73, 80-82], but it was found that these more complex models did not significantly affect the outcome of the model.

2.3.4 Rotor dynamics

After determining the analytical solution of the stator motion, the change of velocity at the tooth position (θ_t) from before to after a collision can be derived from (8b) in analytical form:

$$\delta\dot{u}_i(\theta_t, 0) = \frac{2\pi F_n}{m_s} + \frac{4\pi F_n}{m_s} sin^2(2\theta_t) + \frac{4\pi F_n}{m_s} cos^2(2\theta_t) = \frac{2\pi F_n}{m_s} + \frac{4\pi F_n}{m_s} \tag{12a}$$

Substituting (12a) into (8c) and defining a mass ratio, r_m, as $\frac{3m_r}{m_s}$, the relation between the velocities of the stator/rotor before/after collision becomes:

$$\left(v_{szf} - v_{szo}\right) = \delta\dot{u}_i(\theta_t, 0) = -r_m(v_{rzf} - v_{rzo}) \tag{12b}$$

Given the definition of the coefficient of restitution from (10) and the equation (12b), the expression for v_{szf} (stator velocity after collision at tooth position) and v_{rf} can be derived:

$$v_{szf} = \frac{v_{szo} - r_m(ev_{szo} - (e+1)v_{rzo})}{1 + r_m} \tag{13a}$$

$$v_{rzf} = e(v_{szo} - v_{rzo}) + v_{szf} \tag{13b}$$

Finally, the tangential velocity of the rotor after collision, $v_{r\theta f}$, can also be written as a function of the tangential velocity of the rotor before collision, $v_{r\theta o}$, depending on whether the friction exceeds the maximum allowance:

$$v_{r\theta f} = \begin{cases} v_{r\theta o} + \frac{\mu m_r(v_{rzf} - v_{rzo})r}{J} & if\ \mu < \tan(\alpha) \\ v_{r\theta o} + \frac{tan(\alpha) m_r(v_{rzf} - v_{rzo})r}{J} & if\ \mu > \tan(\alpha) \end{cases} \tag{13c}$$

To verify the appropriateness of the above approach, the FEM model was used. The transient response of the stator to a single collision is simulated by applying identical

downward Gaussian impulses to the top surfaces of the two colliding teeth in a time domain analysis. The response of the stator is calculated and compared to the impulse response predicted by the PMM with identical parameters to those of the FEM; this comparison shows excellent agreement. This agreement and the PMM's relative computational efficiency explains the utility of the PMM in simulating large rotor motions where many hundreds of stator-rotor collisions occur.

In the basic actuator, the rotor is just an annulus with some small features on the top surface for optical testing purposes, so only the mass (m_r) and the radius of the collision point (r, the same as the radius of collision position on stator) are considered in the vertical direction model and the moment of inertia (J_r) in the tangential direction.

After a collision, the transient motion of the rotor is a ballistic motion affected by the gravity force, squeeze film damping force and the drag force. The upward and clockwise directions are defined as positive vertical and tangential motion. The vertical velocity (v_{rz}) and tangential velocity ($v_{r\theta}$) can be written as follows:

$$m_r \dot{v_{rz}} = -m_r g - b_z v_{rz} \tag{14a}$$

$$J_r \dot{\omega_{r\theta}} = -b_\theta \omega_{r\theta} \qquad \text{with} \quad \alpha_{r\theta} = \dot{\omega_{r\theta}} \qquad \omega_{r\theta} = \frac{v_{r\theta}}{r} \tag{14b}$$

in which b_z and b_θ are the damping coefficients in the vertical and tangential directions.

2.3.5 Parameter identification

Before the PMM can generate numerical results, several system parameters must be defined. Parameters can be determined either from prior literature, such as coefficient of restitution and coefficient of friction, or experimentally, such as rotor mass or stator steady-state vibration amplitude. If the model is to be used predictively, the stator vibration characteristics and associated parameters can be estimated using the FEM.

Coefficient of restitution: In general, coefficients of restitution may range from 0 to 1. These coefficients depend on the speed of collision, the materials, and the geometries of the surfaces involved in the collision. Previous studies have shown the coefficient of restitution of collisions between poly-silicon and silicon micro-geometries

to range from 0.57 to 0.642 [83, 84]. Within that range, Coefficient of restitution can be used as a tuning parameter to better match the measured results.

Coefficient of friction: The coefficient of friction (μ) for silicon-on-silicon interaction has been shown to vary widely depending on the exact conditions of the interaction, from 0.03 to 0.69 [85, 86]. This coefficient thus can also be considered as a tuning parameter for this model.

Rotor mass: The mass of the rotor can be measured accurately as a discrete component. It is measured to be 46±0.5 mg. The mass of the stator is estimated from the stator geometry to be 10.7 mg.

Squeeze film damping and drag coefficients: From previous literature, squeeze film damping coefficient (damping coefficient b_z) can be approximated by a few different models [87, 88]. First, from [87], b_z is estimated at $0.6\ \mathrm{mNs/m}$. b_z, while from [88], at about $3.6\ \mathrm{mNs/m}$. Due to the wide range of reasonable damping coefficients, this parameter was also treated as a tuning parameter for the model.

The viscous drag coefficient (drag coefficient b_θ) from air acting to oppose tangential motion was estimated to be $43\ \mathrm{pNs/m}$, by integrating drag forces about the circumference of the hub [89].

Mode shift: the modes of the stator can be shifted in orientation by asymmetries in stator fabrication or the materials themselves. Because the exact value of this shift could not be measured accurately; an estimated range of the mode shift angle (θ_m) is given as -3 to +3° based on the FEM results. θ_m is defined to be positive in the counterclockwise direction. The shift would be same for both actuation modes. In simulation, θ_m is picked to be -2.5°.

Table 1(a): Motor geometric parameters in simulation (Methods used to determine parameter values are denoted as “M” for measured, “E” for estimated, “C” for calculated.)

Parameter (Symbol)	Nom (Var)	Method

Stator inner radius (R_i)	2.125 (±0.02) mm	M
Stator outer radius (R_o)	3.89 (±0.02) mm	M
Tooth inner radius (R_t)	3.063 (±0.02) mm	M
Stator thickness (t_s)	70 (±10) µm	M
Tooth height (h_t)	260 (±10) µm	M
Tooth location angle (θ_t)	62.635 (±0.2) °	M
Mode shift angle (θ_m)	-2.5°	E

Table II (b): Motor parameters of frequency response in simulation

Parameter (Symbol)	Nom (Var)	Method
Mode A frequency (f_A)	2150 (±10) Hz	FEM
Mode A damping ratio (ξ_A)	22.5 (±1.4) mN/m	FEM
Mode B frequency (f_B)	6.30 (±0.01) kHz	M
Mode B tooth amplitude	20.72 (±1.24) µm	M
Mode C frequency (f_C)	7.46 (±0.01) kHz	M
Mode C tooth amplitude	1.81 (±0.11) µm	M
Mode B & C damping ratio (ξ_B, ξ_C)	ξ_B 0.0063 (±0.002) ξ_C 0.0075 (±0.002)	M

Table II (c): Motor properties used in simulation

Parameter (Symbol)	Nom (Var)	Method
Rotor mass (m_r)	46 (±0.5) mg	M
Stator mass (m_s)	10.7 (±1.0) mg	C
Coefficient of restitution (e)	0.6 (±0.04)	[83, 84]
Coefficient of friction (μ)	0.4 (±0.37)	[85, 86]
Damping coefficient (b_z)	3.6 mNs/m	C

Drag coefficient (b_θ)	4.3×10^{-11} Ns/m	C

For the prototype motor, the steady-state motion of the stator in magnetic field can be measured experimentally, rather than estimated from the FEM. The mode frequencies and amplitudes of the stator are measured experimentally by giving a frequency sweep to the sinusoidal voltage input and measuring the motion response of the stator.

The full description of the system parameters obtained are shown in Table 1 (a-c). The values of parameters used in nominal simulations are listed as "Nom" and their variation.

2.3.6 Simulation Features

Using the parameters in Table 1(a-c), simulation code was implemented in MATLAB to predict dynamic motor behavior. The simulation includes a 0.5% random variation in stator vibration amplitude, similar to that measured from an unloaded stator using Laser Doppler Vibrometry (LDV). Figure 13-17 show sample results from the simulated rotor motion. The vertical motion of the rotor can be recognized as a ballistic motion between collisions (Figure 13, Figure 14), with the vertical velocity having a sudden change at impacts and otherwise affected only by gravity and squeeze-film damping. The tangential velocity increases from rest at the beginning of the simulation and eventually oscillates around a stable value (Figure 15).

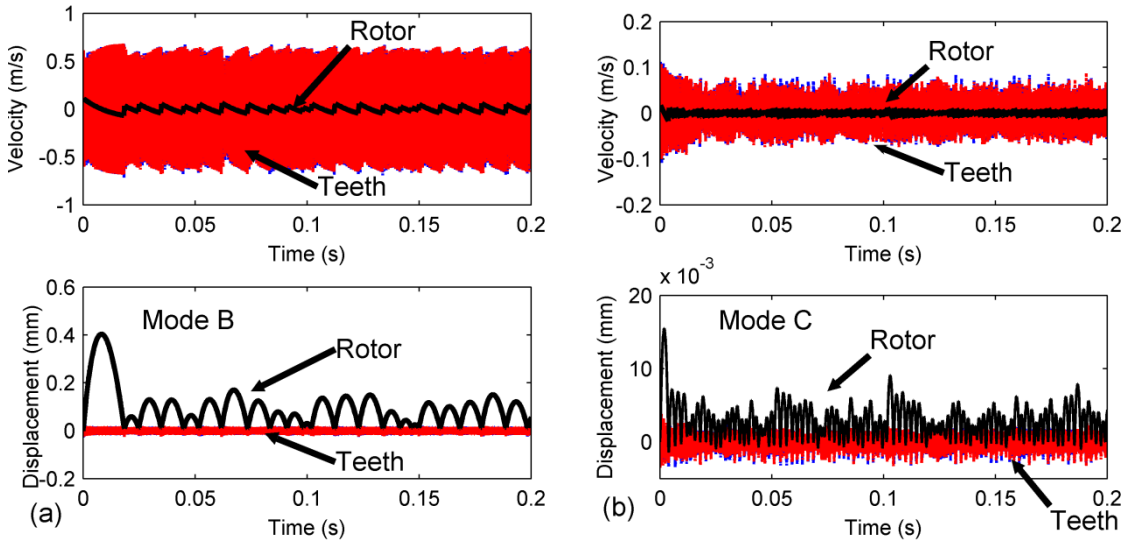

Figure 13 Sample simulation of vertical velocity and displacement in the time domain: (a) Mode B and (b) Mode C.

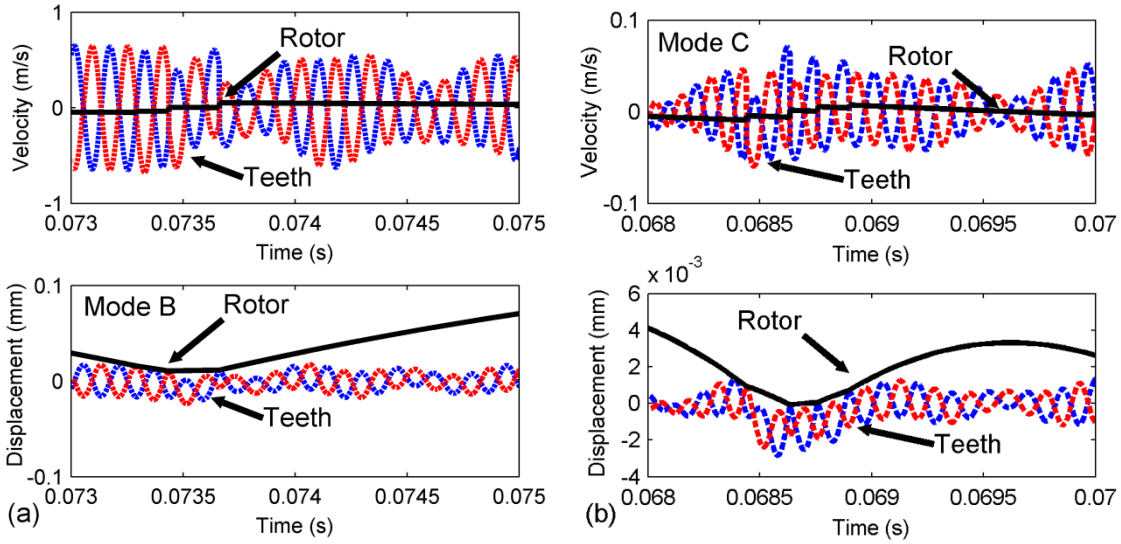

Figure 14 Detail view of simulation in the time domain: (a) Mode B and (b) Mode C.

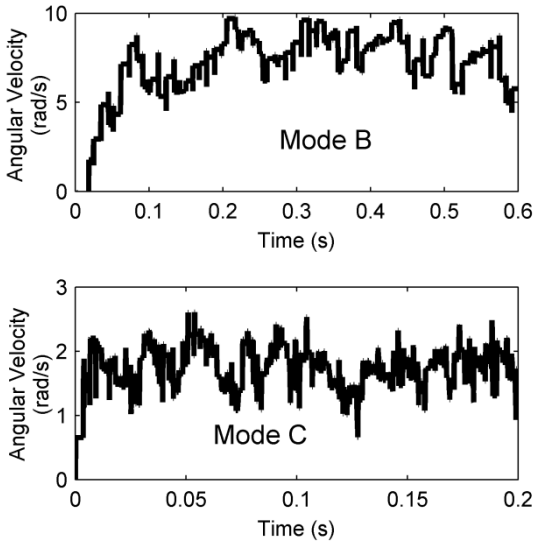

Figure 15 Sample simulations of angular velocity of the rotor (Mode B and Mode C).

A Fast Fourier Transform (FFT) was applied to the generated time-domain results to obtain a frequency spectrum of the motion (Figure 16), which can used to check the reliability of the model quantitatively against experimental results. Because stochastic variation prevents a one-to-one comparison of experimental and simulated time domain data sets, statistical comparisons are made to validate model predictions against experimentally observed behavior. These comparisons are made by first applying a Fast Fourier Transform (FFT) algorithm to each data set. In the frequency domain, collision frequency distribution and peak vertical motion amplitude are the key descriptors of the model output. Detailed simulation results will be further discussed in section III, especially in comparison to experimental measurements.

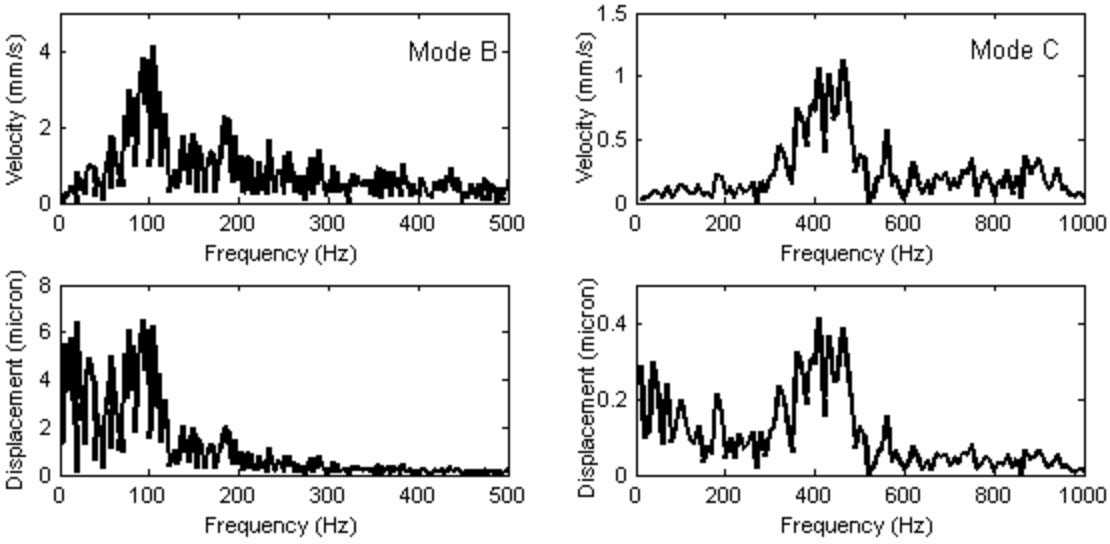

Figure 16 Frequency domain velocity and displacement from simulated rotor motion (Mode B and Mode C).

2.3.7 Suitability of the Fast Fourier Transform in capturing model output

The stochastic nature of the collision behavior makes direct comparison of the simulation time domain output to experimental measurements difficult. Frequency results may be more suitable, and as shown previously the Fast Fourier Transform is the method used to switch from the time domain to the frequency domain. To determine whether the FFT is appropriate for quantifying the model output, the simulated time domain data was first parsed and each period between successive collisions was determined. Plotting this data versus collision number (Figure 17) illustrates groupings of collision periods; these groupings correspond very closely with the peak frequencies determined with the FFT method. Thus, the similarity between the FFT output and a more careful accounting of collision events suggests that the FFT method is appropriate for capturing the essential features of the model output. Beneficially, the FFT method deals with noisy experimental data much more robustly than the parsing method.

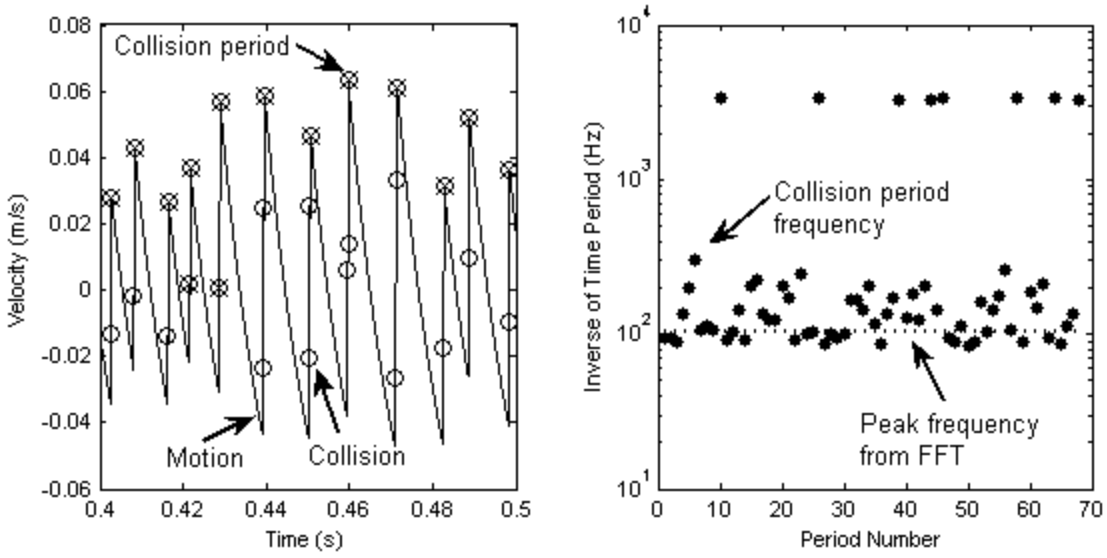

Figure 17 (Left) time series simulation results from the dynamic model, with collision points (circled points) and collision period points (crossed points) figured out (partial time period of the entire simulation is shown here); (Right) band figure of the collision period (dash line is 104 Hz, which is the peak frequency of the velocity (Figure 16) from FFT);

2.3.8 Parameter sensitivity analysis

As noted above, exact values for some parameters in the model are unknown, such as coefficients of restitution and friction. In addition, it is desirable to understand the effect of parameters over which the motor designer has control. By tuning the parameters over their possible range, it is possible to check which dominate the system performance. When checking the influence of single parameter, all the other parameters are held constant at the nominal value (Table 1). For conciseness, only effects on Mode C are presented here. Mode C is selected because this mode has smaller stator vibration amplitude, which in practice reduces the rotor wobble and tilt, the effects of which are not included in the model. The results (Table 2) show the sensitivity of the model output to the parameters of interest. The average and standard deviation of the output reported in Table 2 are calculated from five simulations, each with a random 0.5% variation in stator vibration amplitude. According to the simulations, increasing the stator mass will reduce the collision frequency but increase tangential velocity, with greater energy imparted on the rotor at each impact. In reality, the stator thickness and tooth height both affect the

stator mass; however, in the trend analysis these parameters are treated as independent and tuned separately to better understand physical behavior. Thus, while increasing stator thickness (and thus stiffness) without increasing stator mass has only a minor effect on performance, in practice increasing stator thickness would also lead to larger stator mass, with the effects noted above. Other parameters in Table 2 show much smaller effects on motor performance.

An additional factor that influences rotor behavior substantially is the position of the rotor teeth with respect to the stator mode shapes of Mode B and Mode C. If the tooth position is not accurately aligned with respect to its actuation mode, the simulation will give significantly different results. This misalignment can be due to fabrication errors (photolithography mask misalignment, non-uniform etching, over-etching, etc.) and can be represented in the model with either a deviation from the designed tooth angle or with a deviation of the location of the mode shape antinodes from their ideal location. Because both tooth location angle (θ_t) and mode shift angle (θ_m) will affect the model output in the same way, the sum of the angles is considered. For example, in mode B, shifting the total angle from 62.135° to 58.135° changes the collision frequency from 101 to 85 Hz, and the rotor tangential velocity from 9.05 to 7.14 rad/s. Similarly, in mode C, shifting the total angle from 62.135° to 58.135° changes the collision frequency from 705 to 314 Hz, and the rotor tangential velocity from 0.75 to 3.03 rad/s.

Table 2 Comparison of vibration Mode C simulation results under different value of parameters

Parameter (Symbol)	Parameter value	Collision frequency (Hz)	Tangential velocity (rad/s)
Output with nominal parameter values	See Table 1	448 ±22	1.72 ±0.09
Stator mass (m_s)	9.7 mg	591 ±170	1.36 ±0.17
	11.7 mg	402 ±36	1.96 ±0.15
Stator thickness (t_s)	60 μm	434 ±72	1.67 ±0.13
	80 μm	440 ±42	1.72 ±0.10

Tooth height (h_t)	250 µm	440 ±32	1.67 ±0.13
	270 µm	432 ±52	1.75 ±0.16
Coefficient of restitution (e)	0.57	450 ±37	1.73 ±0.15
	0.642	413 ±55	1.64 ±0.07
Coefficient of friction (μ)	0.03	430 ±49	1.80 ±0.07
	0.69	430 ±20	1.68 ±0.18
Squeeze film damping coefficient (b_z)	0.6 mNs/m	416 ±59	1.72 ±0.13
	3.6 mNs/m	448 ±22	1.72 ±0.09

2.4 Experimental Validation

2.4.1 Experimental Design & Setup

An experimental system was used to check the reliability of the simulation for the prototype micro-motor (Figure 18). The magnetoelastic layer was actuated with dual Helmholtz coils that directed an oscillating magnetic field in the same plane as the magnetoelastic layer. The magnetoelastic layer was magnetically biased using small permanent magnets oriented in the same direction as the oscillating field. Vertical motions of multiple points on the unloaded stator are measured by a Laser Doppler Vibrometer (LDV, Polytec OFV 303 sensor head and a Polytec OFV 3001 S vibrometer controller) to check the accuracy of the stator FEM model. The amplitude of the magnetic field generated by the coils at the position of the motor is measured by a gaussmeter (F.W. Bell model 5170) as 8 Oe, typically. A microscope with a high-speed camera (Photron FASTCAM MC2.1 & LEICA 104459290.5x) was used to track rotation of the rotor. The resolution of the camera, when used in conjunction with a microscope, was approximately 2 microns. The frame rate of the camera was as high as 10000 frames per second.

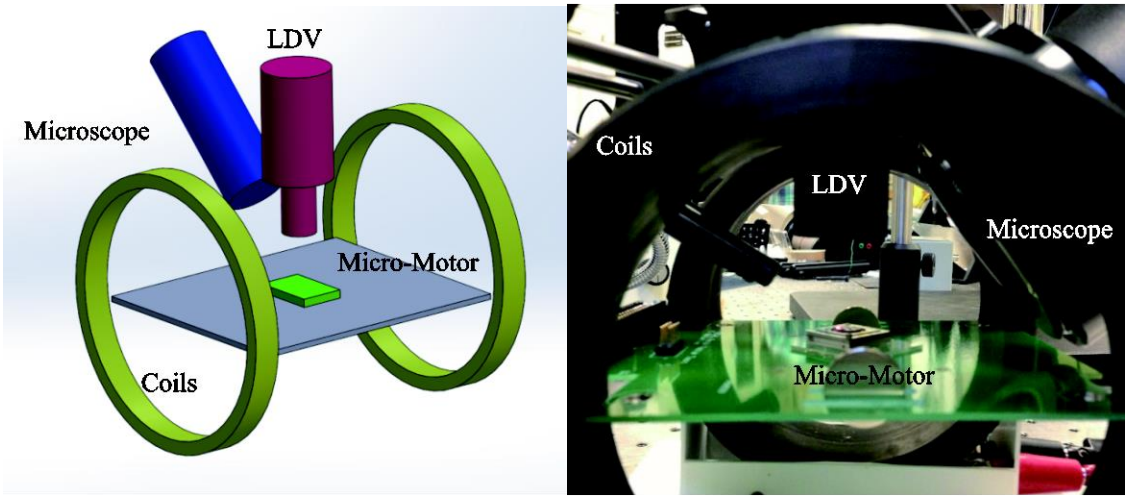

Figure 18 (a) Schematic of the experimental set-up with LDV (red) and microscope (blue). The micro-motor (green) is actuated by the magnetic field generated in the coils (yellow). (b) Photograph of the experimental set-up.

2.4.2 Experimental Results

Velocity and displacement

Results from experimental measurement of vertical rotor velocity are shown in Figure 19 for modes B and C, respectively. The displacement of the rotor is calculated by integrating the velocity over time (shown in Figure 19). As for simulations, an FFT is applied to the experimental measurements. The peak frequency in the resulting FFT spectrum is considered the representative collision frequency for the data set. The amplitude at the peak frequency is also a point of comparison between the simulated and measured results. Tangential velocities are measured by the high-speed camera at frame rates of 5000 fps (mode B) and 10000 fps (mode C).

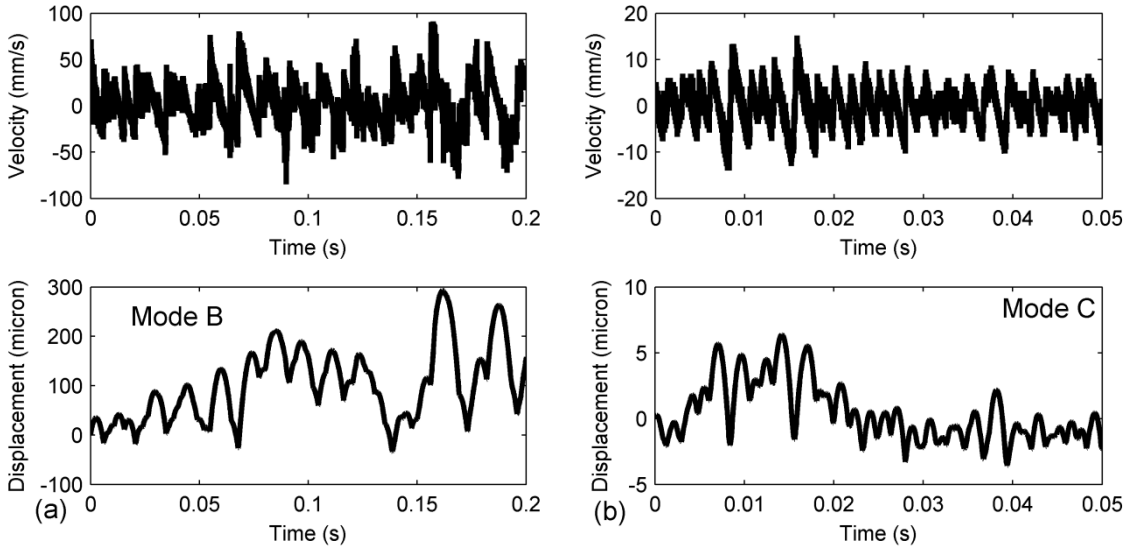

Figure 19 Typical time domain experimental velocity and displacement under (a) mode B; (b) mode C.

Tuning of parametric model

As shown in Table 2, the output of the model is relatively insensitive to shifts in many of the available tuning parameters – coefficient of friction, coefficient of restitution, and squeeze film damping coefficient. However, one tuning parameter that does have significant influence on the model output is the mode shift angle. For mode B, in steady state the frequency of the vertical motion is always around 80 Hz regardless of the mode shift angle. Meanwhile, for mode C, the frequency decreases while the shift angle increases. Considering that the measured collision frequency for mode C is around 400 Hz, tuning the mode shift angle to a value between -2.5° and -3° results in a good match between simulated and experimentally measured collision frequencies. Therefore, in the following comparison, the mode shift angle in the simulation is set to -2.635°, which makes the sum of the tooth position angle and mode shift angle 30°. The collision frequency and frequency spectrum of vertical motion is well predicted for both mode B and mode C, as shown in Table 3 and Figure 20. The averages and standard deviations of the presented data are based on the sampling of five simulated and three experimental data sets. The average simulated vertical rotor velocities of both mode B and mode C are larger than average of the experimental results, although standard deviations do

significantly overlap. These small differences may be caused by not including in the model all sources of friction on the rotor (e.g., friction between the hub and the rotor).

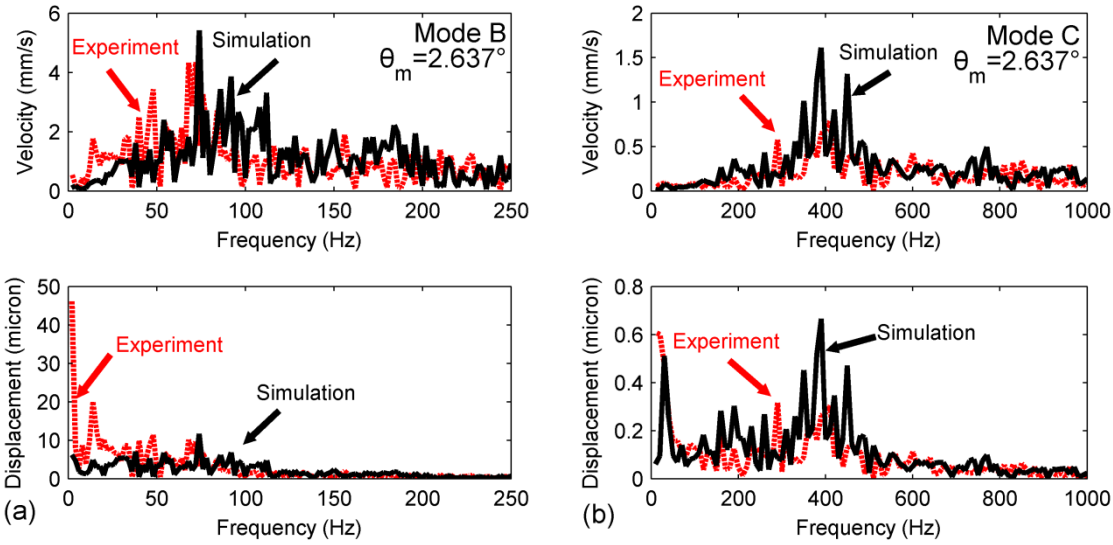

Figure 20 Frequency spectrum of simulated (black solid line) and experimental (red dash line) velocity and displacement; Mode shift angle is 2.635° (a) mode B; (b) mode C.

Table 3 Simulation and experiment comparison

Rotor behavior	Simulated	Experiment
Mode B collision frequency	88.8 ± 7.13 Hz	76 ± 20 Hz
Mode B collision amplitude	4.08 ± 1.17 mm/s	3.94 ± 0.57 mm/s
Mode B tangential velocity	8.16 ± 0.80 rad/s	~1 rad/s
Mode C collision frequency	422 ± 51.8 Hz	400 ± 104 Hz
Mode C collision amplitude	1.48 ± 0.26 mm/s	0.88 ± 0.28 mm/s
Mode C tangential velocity	1.72 ± 0.22 rad/s	~1.4 rad/s

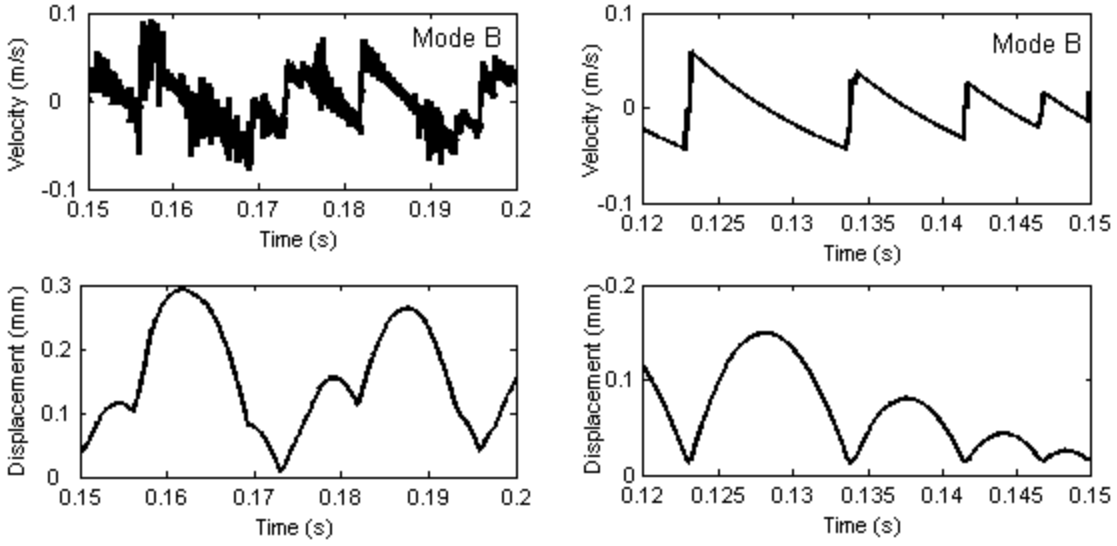

Figure 21 Mode B: (a) Evidence of rotor-to-hub collisions in the experiment results; (b) simulation results without hub collision

Meanwhile, the tangential velocities of modes B and C are not equally well predicted. For mode C, the predicted tangential velocity is slightly smaller than the measurement. This is within expected errors due to the sensitivity of simulated results to the exact mode shape and mode shift angle. However, tangential velocity for mode B is substantially over-estimated. This is believed to be due to the stator motion of mode B (about 20 μm amplitude) being much larger than the motion of the mode C (about 1.8 μm amplitude), which leads to non-ideal effects such as rotor wobbling and tilting. Rotor wobble, tilt, and hub collisions are effects not included in the dynamic model; the presence of these effects in the experimental measurements, much more prominently for mode B, are believed to be the primary cause of the discrepancies between the experiment and simulations (Figure 21).

2.4.3 Sensitivity to payload and stator amplitude

Using the parametric modal model, it is possible to predict the collision frequency and tangential velocity of the rotor under varying actuation conditions including a different payload (rotor mass) and different driving magnetic field strength (tooth

amplitude) for the two actuation frequencies. By using the parameters defined in last section, collision frequencies and tangential velocities are simulated, as shown in Figure 22 and Figure 23, with different rotor masses and tooth amplitudes.

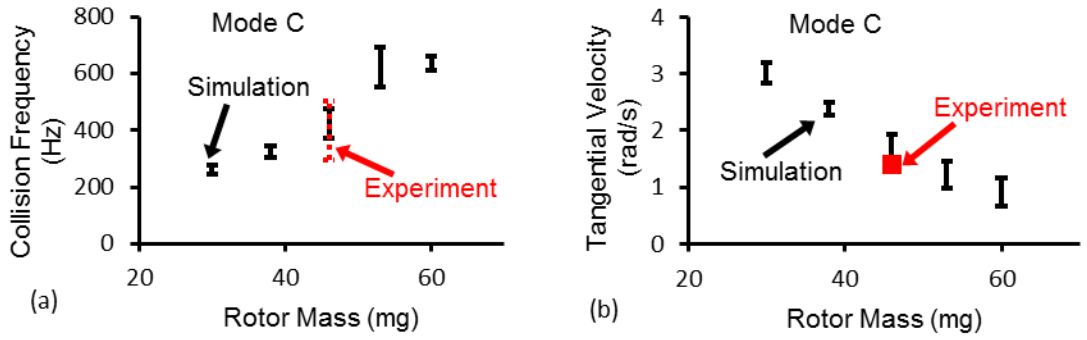

Figure 22 Mode C (a) collision frequency with different rotor mass; (b) tangential velocity with different rotor mass.

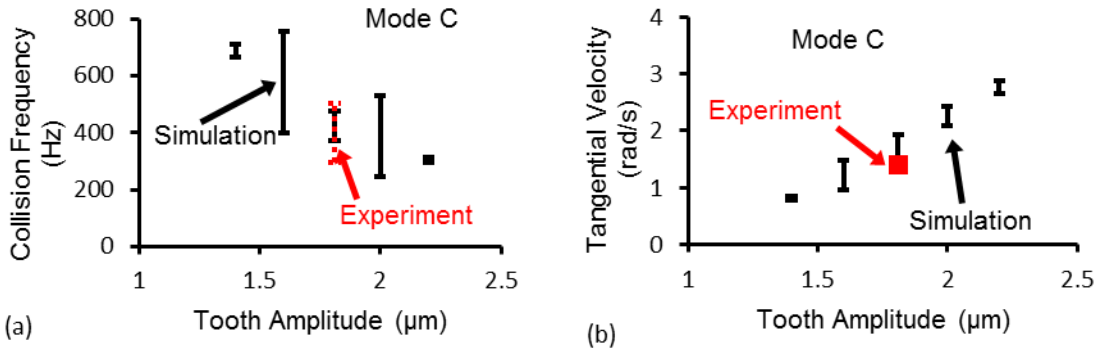

Figure 23 Mode C (a) collision frequency under different tooth amplitude: simulation (black solid line) and experiment (red dash line); (b) tangential velocity under different tooth amplitude: simulation (black solid line) and experiment (red dot).

For mode C (Figure 22 and Figure 23), the collision frequency has a roughly linear relationship with rotor mass and tooth amplitude; the collision frequency increases with increasing rotor mass and decreases with increasing tooth amplitude. The tangential velocity also has a linear relationship with rotor mass and tooth amplitude, and the relationships are the inverse of those for collision frequency. The experimental results fit

the simulation within the range of error, indicating that the parametric modal model can be a useful tool for predictive design.

2.5 Sensor Design

The purpose of developing the simulation model for magnetoelastic rotary stage motion described in the previous section is to provide a means to evaluate and improve state estimation algorithms for tracking stage motion during gyroscope calibration. The remainder of this chapter examines the performance of a Kalman smoother as the estimator for stage motion when sensor measurements are taken from a set of symmetric capacitive electrodes on the rotor and stator.

2.5.1 Capacitive Sensing Geometry

A challenge for the use of sensing in a MEMS-type actuator for calibrating a MEMS gyroscope is that the sensing elements on the actuator may be subject to variation over time as large as or greater than that in the gyroscope. Thus, the capacitive sensing system designed for this system is intended to have certain invariant features. Furthermore, for a continuously rotating actuator about a central hub, it is desirable to minimize sensor sensitivity to off-axis motion (i.e., to displacements r_x or r_y, which are lateral displacement of the center of the robot in the x- and y- directions, respectively).

The proposed sensor geometry consists of a two pairs of circular electrodes that connected in series, with one plate of each pair on the rotor and one plate on the stator, as shown in Figure 24. The capacitance between the electrodes reaches a peak value when the rotor electrodes are at exactly the same angle as the stator electrodes, which for simplicity in this analysis occur at an angle of 0 rad. Due to symmetry, any angular displacement from that critical angle will cause a decrease in capacitance, even when the rotor is not perfectly centered over the stator, as shown in Figure 25 for 0.25 mm diameter electrodes centered 2.5 mm from the hub. The one exception to this is the case

when displacement in there is rotor translation in x- alone ($r_y = 0$, $r_x \neq 0$), when there is a symmetric but flat plateau in total capacitance.

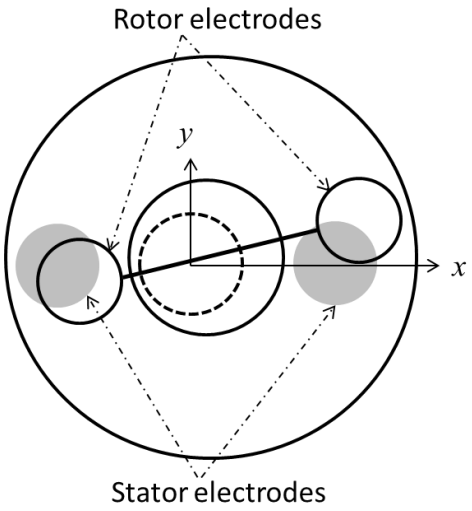

Figure 24 Symmetric, paired electrodes, such as the circular electrodes shown here, produce maximum capacitance at their angle of maximum overlap, which is largely insensitive to translational displacement of the rotor relative to the hub.

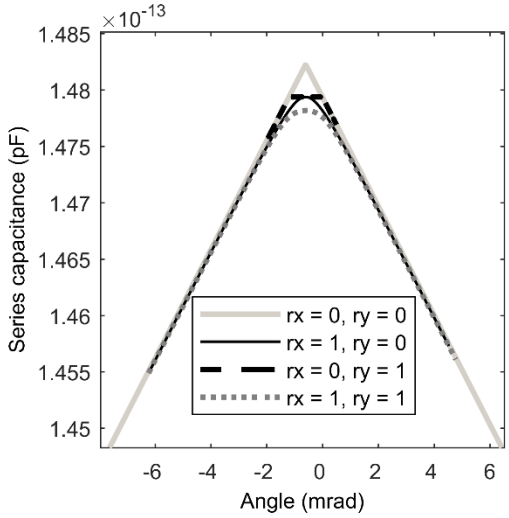

Figure 25 Capacitance versus angle for translational perturbations in r_x and r_y using symmetric, circular electrodes, showing constant peak capacitance angle except when only r_y perturbation present, in which case capacitance plateaus.

2.5.2 Smoothing results with capacitance model

Given the plant model and capacitive sensing model, an extended Kalman smoother is presented in [90]. Rotary stage motion was simulated under a variety of disturbance scenario. Model detuning parameters were selected from a uniform random distribution with 5% variance, and Kalman smoother estimation error was averaged over 20 runs for each tested scenario of disturbance and noise variance.

Two sample runs of simulated stage rotation and then estimated stage rotation using the extended Kalman smoother are shown in Figure 26.In both cases, and typical of estimation results using the smoother, estimation tends to be poor away from the peak capacitance angle at 0 rad due to unknown detuning of capacitance gain and angular velocity. However, near the peak capacitance angle of 0 rad, estimation accuracy is much more accurate. This is attributed to the large ratio of capacitance to noise at that angle, as well as the fact that smoothing errors would become very large if the transition from a positive to negative slope of capacitance versus angle were not accurately placed by the minimization in numerical optimization.

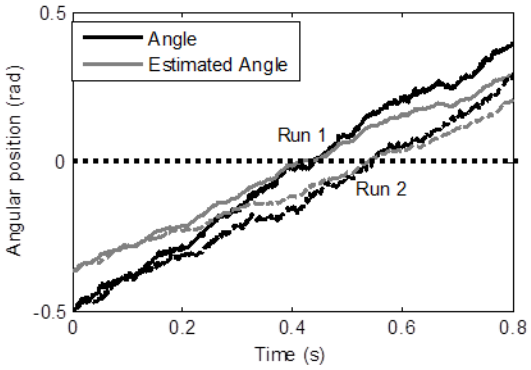

Figure 26 Two sample runs of the rotary stage motion simulator show estimation accuracy of the Kalman smoother is greatest near the critical capacitance overlap angle of 0 rad. Sensor noise = 1e-16 pF and approximately proportional relationship between rotational and translational variation.

The observed ability of the described smoothing algorithm to keep error small at the critical peak capacitance angle is further shown in Figure 27, which shows standard deviation of angular position estimates versus rotor angle with a selection of noise and correlation conditions. In this plot, normalized correlation of 1 indicates that there is a proportional relationship between angular and translational deviation. In all cases, estimation error is smallest near the critical angle of 0 rad. This is important because the peak capacitance angle is constant with respect to translation of the rotor relative to the hub, while absolute capacitance measures may vary due to the rotor translation and or circuit gain detuning.

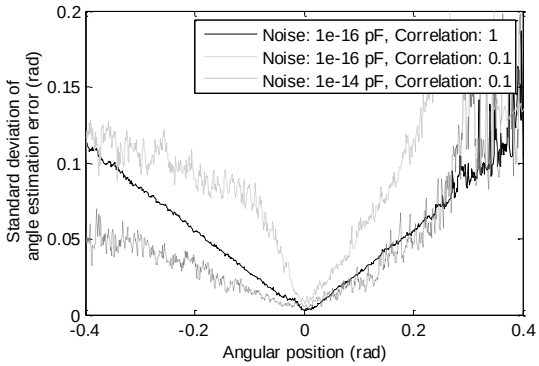

Figure 27 Standard deviation of angular position error versus rotor angle for 20 repeated simulations at various noise and disturbance conditions (equating to high or low correlation between rotary and translational deviation) consistently show best estimates of rotor position near the angle of maximum capacitance, 0 rad.

2.6 Conclusion

This chapter develops a dynamic model for a chip-scale magnetoelastic rotary motor actuated by generating a standing wave in a magnetoelastic stator, with momentum transferred to a continuously revolving rotor through collisions with a finite number of stator-located teeth. The stator is treated as a distributed second order linear system excited by a magnetoelastic field, and the response of individual vibrational modes are tracked and summated to determine the total movement of the stator in response to a driving magnetic field and to collisions with the rotor. The dynamic model demonstrated

in this chapter can qualitatively predict most features of the motor behavior observed in experiments. By tuning a small number of parameters, the model can also achieve a very good quantitative fit to experimentally-observed tangential and vertical motion of the rotor under certain actuating conditions. Furthermore, a capacitive sensor is developed to track the rotation of the device, with an estimator designed using the dynamic model for evaluation in simulation.

The dynamic model has substantial benefits for magnetoelastic rotary motor design in allowing the effects of various parameters to be quantified. The stator mass and the tooth height will affect the collision frequency most, while the tangential velocity is affected primarily by the stator mass and mildly by coefficient of friction. The stator thickness, coefficient of restitution and squeeze film damping coefficient are less important for the rotor dynamics.

However, the model still lacks some phenomena that influence motor behavior. For example, for mode B in the prototype system, the simulated and experimental results for tangential velocity do not match well, highlighting one limitation of the model: first, larger stator and rotor motion may lead to unbalanced rotor movement and hub collisions, which are not included in the model. In addition, certain model parameters are difficult to predict before building a motor, especially friction between teeth and the rotor or the hub and the rotor. Future modeling work may include tracking each of four teeth separately (and the necessary asymmetrical mode shapes). This modification could allow the model to include the tilting of the rotor, which may capture small but important aspects of the dynamic motor behavior. Modeling of the contact between the rotor and hub in the current motor design may be more complex; improving the motor design to mitigate this contact – either through a longer hub or by constraining the vertical rotor motion – may be a more practical approach.

CHAPTER 3 Modeling Legged Micro-Robot Locomotion based on Contact Dynamics and Vibration in Multiple Modes and Axes

3.1 Introduction

This work examines the interaction of structural and contact dynamics in locomotion of small (<10 cm), elastic terrestrial robots operated near resonance. Many approaches have been applied to the general study of robot walking dynamics, but small-scale and/or elastic behaviors can add complexity. For large-scale robots and structures, two approaches to dynamic modeling are extensively used: rigid body models and elastic models. Most dynamic models of large-scale robots use lumped mass, spring, and damper approximations [91, 92], though continuous elastic models have also been used for some structures with compliant behavior, typically robot arms described in modal form [93, 94].

While large-scale robots are more likely to be actuated with motors at distinct joint locations, small-scale robots often feature compliance throughout or over large portions of their structure. Additionally, locomotion is influenced by light damping compared to larger systems, large fabrication uncertainties relative to the size of structural features, and relatively high resonant frequencies [44, 47]. This is especially prevalent in robots based on smart materials and/or micro-machined structures. Integrating the resulting vibration behavior with other dynamic interactions encountered by small-robots, such as foot-terrain impact, has yet to be studied in detail.

Understanding the dynamics of walking micro-robots is important for design, estimation and control of efficient locomotion [6]. However, what work has been done on dynamic, small-scale robot locomotion has varied dramatically based on robot design,

actuation principles, and operating environment. For example, a previous small-scale (millimeter- to centimeter-scale) robot study showed the importance of dynamic analysis for a type of walking micro-robot with multiple pairs of legs, but the study was performed under assumptions of ideal foot-ground contact with excitation from an external vibration field [24]. Other works have measured dynamic performance without detailed analysis [42]. Works focusing on small-scale effects in micro-robots using an analytical framework have addressed more limited types of gait or operation, including 1) stick-slip walking on a smooth surface [43]; 2) multi-axis, multi-layer elastic leg dynamic operation in air [48, 95] ; 3) ground contact of a single leg [63]. Studies of small robot dynamics at a full-robot level have included finite element analysis [34] and use of lumped parameter models dictating interaction between legs and body [44, 47], including with some foot-terrain interaction [64]. A summary of the above combinations of robot and ground contact dynamic modeling techniques are compared in Table 4 for various walking robots with sizes ranging from tens of centimeter to tens of microns.

Table 4 Comparison between existing modeling of small-scale robots (MKB stands for mass-spring-damper; DOF stands for degrees of freedom)

	Size	Leg	Dynamic Model	Contact Dynamics	Comments
[96]	53 cm; 7 kg	Motor actuation; 6 legs	Rigid body and lumped MKB leg model	Restrict contact angle	
[91, 92]	155×116×70 mm	Motor actuation; 6 legs	Rigid body leg model	Qualitatively analyze legs	mimic cockroach locomotion
[97]	10 cm; 16.2 g	Motor actuation; 6 legs	NA	NA	survive under large impact;
[98]	~10 cm; 90 – 190 g	Motor actuation; 4 legs;	NA	NA	overcome 3.8 cm obstacle
[99]	9 cm long	Motor actuation; 4 legs	NA	NA	overcome large obstacle

[49]	~3 cm; 2.4 g	Shape memory alloy actuation; 6 legs; 2.4 g	NA	NA	all parts on board
[34]	30 x 20 mm^2	Seismically vibrational actuation; 3 legs; 2 arms	FEA modal analysis; motion not modeled	Bouncing; not modeled	frequency up to 2k Hz
[46, 100]	NA	Piezoelectric actuation	Multi-layer beam piezoelectric actuated leg	NA	focused on the swarm control pattern
[44]	< 10 cm; 2.2 g	Piezoelectric actuation; 20 legs	Horizontal plane; Euler Lagrange Equation; low frequency; rigid body lumped MKB system for segmented robots	Two States: stance and swing; undulatory gaits	low frequency actuation
[47]	3.5x3.5x1 cm; 750 mg	Piezoelectric actuation; 6 legs			
[24]	1.5x0.7 mm	External vibration resonant actuation; 6 legs	Lumped MKB system; 2DOF; w/o motion prediction	Impact; not modeled	supporting legs always stay on ground
[25]	15x5 mm;	Thermal actuation; 8 legs	NA	NA	2500 mg Payload; 1DOF; ~100 Hz
[42]	1x1x0.5 cm; 127.5 mg	Electrothermal actuation; 96 legs; 127.5 mg	NA	Stick and slip micro-robot without dynamics model	Stick and slip micro-robot; 2DOF
	5x5x0.5 mm; 32 mg	Electrothermal actuation; 90 legs			1 DOF
[43]	12x12x10 mm; 4.5 g	Electrothermal actuation; 8 legs;	Stick and slip; 1DOF; lumped MKB system	Coulomb friction model	Li-polymer battery; Payload <

					9g
[48]	NA	piezoelectric actuation;	Moments of inertia leg model	NA	Not a full robot

Unlike these existing works on dynamic locomotion of small-scale walking robots, this chapter focuses on the problem of how to effectively account for elastic behavior in miniature robot legs with ground contact. Specifically, we identify an appropriate model for interaction between an elastic robot leg and contact dynamics from ground impact, and highlight some notable resulting phenomena that have influence on the effectiveness or speed of robot locomotion. The model is then verified experimentally using two different centimeter-scale prototypes.

The prototypes used in this study employ piezoelectric actuators bonded to 3D-printed bodies. Their geometries are designed with legs that have coupled in-plane and out-of-plane dynamics, range-of-motion, and operating frequencies representative of even smaller, millimeter-scale piezoelectric micro-robots made with silicon-micromachining [48]. In addition, the two prototypes were fabricated at different size-scales, where the larger robot has dimensions of 4 x 7 x 1 cm^3, and the smaller robot has dimensions of 1.6 x 3.0 x 0.4 cm^3. These small-scale robots have a combination of rigid and compliant structures as well as significant influence of ground contact behavior, resulting in dynamics which demonstrate greater complexity than has been analyzed in prior walking robots of similar size. The proposed model captures motion across multiple legs having multi-axis modal behavior, building upon prior studies of small-scale appendage and single-foot ground contact [63, 64]. The experimental behaviors of the centimeter-scale 3D-printed prototypes are compared with simulations from the dynamic model. Key results include predictions of the direction and amplitude of robot motion under different actuation signal conditions, with more detailed measurements and simulations of vertical motion of the legs. Sensitivity of robot motion over different robot parameters is also analyzed to provide a basis for the design of robot locomotion and parameter optimization.

3.2 Model Description

3.2.1 General Robot Architecture

Robots studied in this chapter include small-scale (<10 cm) walking robots with multiple pairs of elastic legs connected by a rigid body. Figure 28 shows a schematic view of a robot with *2n* legs, each of which may be modeled using stiffness and compliance matrices. The motion of each foot in the *y*-*z* plane is examined (in the directions of robot forward and out-of-plane motion from ground). Motion in these two degrees of freedom under proper operating conditions may produce locomotion against friction and gravity forces acting on the robot. In Figure 28, parameters $k_{j,i}$ and $b_{j,i}$ represent the spring constant and damping coefficient of the *i*-th mode of the *j*-th leg. In addition, each leg is taken to have a known nominal gain with respect to voltage and ratio between motion in y- and z- directions for relevant vibration modes.

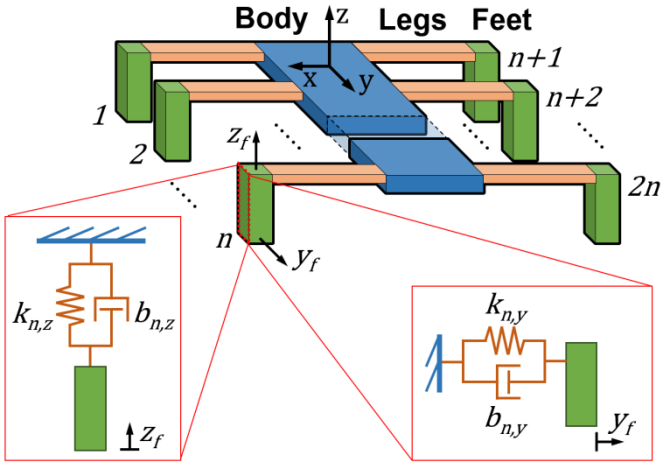

Figure 28 Schematic of a generic micro-robot with 2n elastic legs connected to a rigid body. The motion of each foot in the y and z-directions is modeled by two separate mass-spring-damper systems.

This general architecture is inspired by a type of millimeter-scale, piezoelectric and polymer thin-film robot fabricated with micro-machining, shown in Figure 29 (a), with a rigid body and multiple pairs of legs on both sides of the body. The legs are made of parylene and silicon microstructures actuated by thin-film lead-zirconate-titanate (PZT)

[48]. Figure 29 (b) shows legs designed with two degrees of freedom, vertical and in-plane, that are connected in series to produce approximately elliptical motion from each appendage. To date, these robots have only been successfully actuated within the silicon chips on which they are built [48]. However, they have shown relatively large ratios of actuation force to the amount of electrical energy required to drive the piezoelectric actuator, making them promising for future autonomous locomotion.

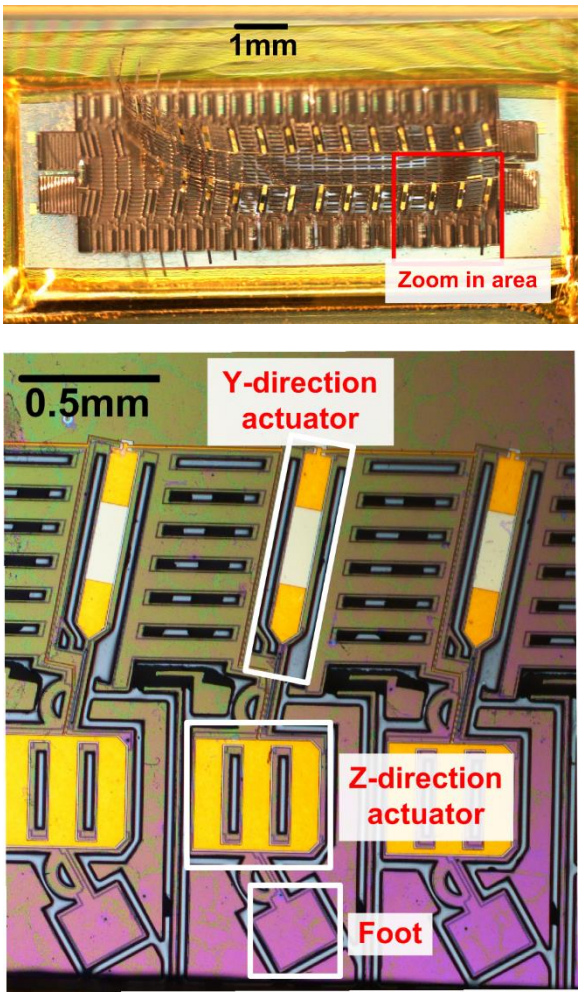

Figure 29 Photo of a) a silicon micro-machined millimeter-scale micro walking robot; b) legs detail of the micro robot.

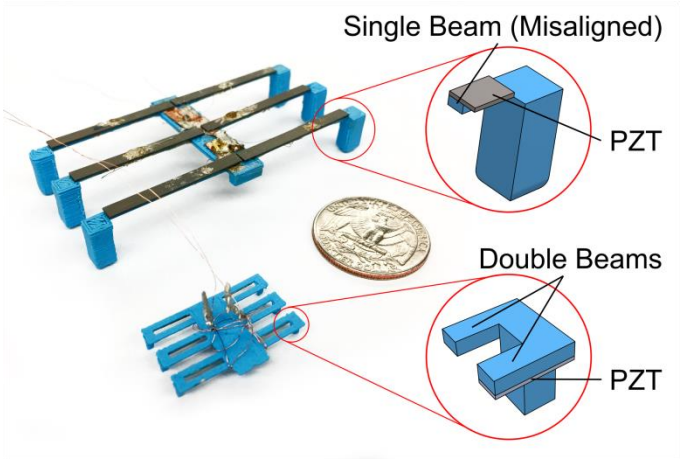

Figure 30 Photograph of both centimeter-scale walking robot prototypes with schematics of leg construction for each. The 80 mm prototype (top) uses a single-beam leg design with a misaligned PZT actuator, and the 30 mm prototype (bottom) uses a double-beam leg design with a PZT actuator on one beam and the other beam left unactuated.

The same robot modal behavior may be realized through other robot designs, which can allow for rapid prototyping and evaluation of dynamics over more varied surfaces and operating ranges. The current study is performed using two different centimeter-scale 6-legged prototypes, made with a 3D-printed polylactic acid (PLA) frame bonded with piezoelectric ceramic strips as actuators (Figure 30). The asymmetric leg actuation of both robots can be modeled with coupled modal dynamics in two directions, the model framework inspired by the millimeter-scale robots [48].

3.2.2 Leg Model

General Description

Actuation from embedded piezoelectric actuators operating near resonance is intended to generate leg displacements in pseudo-elliptical trajectories, driving the robot forward as contact is made with ground. The current analysis assumes that equal numbers of legs are being actuated in- and out- of phase at the operating frequency, i.e., exchanging between sets of three legs in a simple hexapod gait.

In the centimeter-scale prototypes developed in this study, the compliant leg takes the form of a misaligned or an asymmetric cantilever beam. Uniform deformation of

piezoelectric cantilever microactuators has been studied in some detail [101] [102], and beam dynamics are compiled into a conventional modal format in this analysis.

Leg Dynamics

The uniformly distributed piezoelectric actuation force within the beam and point contact force acting on a robot foot, as functions of time, cause the time response of the beam. The analytical solution of the forced response of such a beam, in the vertical direction, is given in a previous study (eq8.110-eq8.116 [103]). The effective force (Q_i) acting on the *i*-th mode could be derived as:

$$Q_i = \frac{\int_0^L f(x) w_i(x) dx}{\rho A \int_0^L w_i^2(x) dx} \tag{1}$$

in which *f(x)* is the force as a function of position, *x*, along the cantilever beam, ρ is the density of the beam, and *A* is the cross sectional area. With the effective mass for point impulse force ($m_{i,imp}$) and uniformly distributed pulse force ($m_{i,pls}$), the final form of the impulse ($Q_{i,imp}$) and pulse ($Q_{i,pls}$) effective force is:

$$Q_{i,imp} = \frac{w_i(L)}{\rho A \int_0^L w_i^2(x) dx} f_{imp} \delta\left(t - t_{imp}\right) = \frac{1}{m_{i,imp}} f_{imp} \delta(t - t_{imp}) \tag{2}$$

$$Q_{i,pls} = \frac{\int_0^L w_i(x) dx}{\rho A \int_0^L w_i^2(x) dx} F_{pls} = \frac{1}{m_{i,pls}} F_{pls} \tag{3}$$

in which w_i is the displacement function of *i*-th mode; ρ is the area density of cantilever beam; *A* is the cross section area of the beam; f_{imp} and f_{pls} are the impulse force acting on the end of beam and the equivalent piezoelectric force acting on the entire beam.

For derivation of the leg model, modes for each robot leg and foot system are assumed to be independent from each other due to the assumption of a rigid central robot body. Leg models are derived from standard multilayer beam analysis [101] such that a state space form can present the system behavior as follows:

$$\begin{bmatrix} \dot{X}_{j1} \\ \vdots \\ X_{jn} \end{bmatrix} = \begin{bmatrix} A_{j1} & & 0 \\ & \ddots & \\ 0 & & A_{jn} \end{bmatrix} \begin{bmatrix} X_{j1} \\ \vdots \\ X_{jn} \end{bmatrix} + \begin{bmatrix} B_{j1} \\ \vdots \\ B_{jn} \end{bmatrix} \begin{bmatrix} f_{imp} \delta(t - t_{imp}) \\ f_{pls} \end{bmatrix} \tag{4}$$

$$z_j = [1 \quad 0 \quad \dots \quad 1 \quad 0] \begin{bmatrix} X_{j1} \\ \vdots \\ X_{jn} \end{bmatrix} \tag{5}$$

$$A_{ji} = \begin{bmatrix} 0 & 1 \\ -k_{ji} & -b_{ji} \end{bmatrix}; \quad B_i = \begin{bmatrix} 0 & 0 \\ \frac{1}{m_{i,imp}} & \frac{1}{m_{i,pls}} \end{bmatrix} \quad X_{ji} = \begin{bmatrix} x_{ji} \\ \dot{x_{j\iota}} \end{bmatrix} \tag{6}$$

in which j is the leg number, k_{ji} and b_{ji} are the spring constant and damping coefficient, normalized by effective mass, with respect to each mode for leg j; z_j is the j-th foot displacement in the vertical direction; x_{ji} and $\dot{x_{ji}}$ are the displacement and velocity for the i-th mode of the j-th leg; f_{imp} is the impulse force acting on the tip of leg; f_{pls} is the pulse force acting uniformly on the entire leg; $\delta(t\text{-}t_{imp})$ is the Dirac delta function representing when impulse force occurs (t_{imp}); $m_{i,imp}$ and $m_{i,pls}$ are the effective mass for the i-th mode for the impulse and piezoelectric forces. In simulation, the state space form is discretized. Gravitational force on the leg and the internal piezoelectric actuation force are treated as uniformly distributed, while ground contact force and the weight of the robot's foot are treated as acting on a single point at the tip of the leg.

The actuation architecture is confirmed with finite element analysis in COMSOL Multiphysics [104, 105], as shown in Figure 31. To perform multi-axis modeling, it is assumed that: 1) motion in z- and y- directions is coupled, which means their systematic parameters (modal frequency and damping) are identical; 2) the actuation force in z- and y= direction is different, but related by a constant proportionality coefficient.

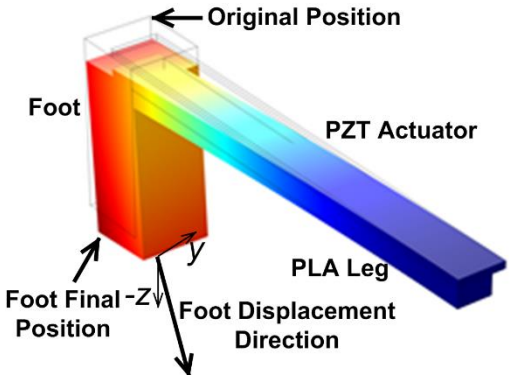

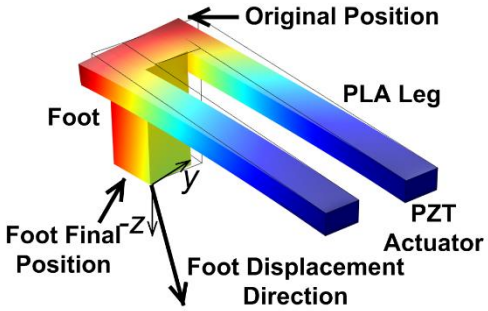

Figure 31 Finite element analysis (FEA) illustration of leg displacement in Y- and Z-direction of 30 mm centimeter-scale prototype (bottom) and 80 mm centimeter scale prototype (top).

Contact Model: Friction and Restitution

The contact dynamics of micro-robotic appendages at the current size scale was previously studied in [106]. A continuous contact model is chosen because it is a force-based model for use with the leg dynamics from (4). To relate contact behavior with measurable velocity data, the robot is modeled with Newton's restitution model, in which the coefficient of restitution is related to the change of velocity before and after contact.

A basic modeling method of restitution and friction is applied. Both forces are assumed to happen during a short period of time. The contact between a foot and ground is modeled simply by the coefficient of restitution (c_r) from Newton's model and the coefficient of friction (c_f) from the dry friction model [106]. Considering the velocity in y- and z-direction before (v_{yo}, v_{zo}) and after contact (v_{yf}, , v_{zf}), behavior during contact is modeled as:

$$v_{zf} = -v_{zo}c_r \tag{7}$$

$$v_{yf} = \begin{cases} max\left(0, v_{yo} - c_f\left(v_{zf} - v_{zo}\right)\right) & if\ v_{vo} > 0 \\ min\left(0, v_{yo} + c_f\left(v_{zf} - v_{zo}\right)\right) & if\ v_{vo} \leq 0 \end{cases} \tag{8}$$

It is assumed that the ground has infinite mass and negligible compliance, and that the friction does not influence vertical motion. The lateral change in velocity (8) is derived by treating the effective impulse force implied by (7) as the normal force in friction calculation. The coefficients of certain sample ground surfaces will be identified for simulation in later section.

3.2.3 Body Model

5-DOF vs. 3-DOF Interactions

The robot body could be considered as a rigid body with six degrees of freedom. The standard moments of inertia in three directions (I_x, I_y, I_z) quantify rotational inertia. The forces acting on the body arise from the spring and damper equivalents in the leg/foot model, acting on the connection points between the legs and the body. Since six legs are symmetrically connected to the body, their forces in two (z- and y-) directions are considered, but lateral (x-axis) forces are omitted from this analysis.

First, the distances from the body's center of mass to the legs are given in vector form (x, y, z). When calculated for the small-scale robots, this takes the form

$$\boldsymbol{x} = [l_{x,1}\ l_{x,2} \cdots\ l_{x,2n}],\ \boldsymbol{y} = [l_{y,1} \cdots\ l_{y,2n}],\ \boldsymbol{z} = [l_{z,1} \cdots\ l_{z,2n}] \tag{9}$$

in which $l_{x,i}$, $l_{y,i}$, and $l_{z,i}$ are the x-, y- and z-direction distances from the exterior $2n$ legs to the body center of mass (the geometry is considered symmetric, which means the two middle legs have y-directional distance equal to zero). The total forces transmitted from the legs for the centimeter-scale robot prototypes are enumerated by vectors:

$$F_{yl} = [F_{1,y}\ F_{2,y}\ \cdots F_{2\mathrm{n},y}],\ F_{zl} = [F_{1,z}\ F_{2,z}\ \cdots\ F_{2\mathrm{n},z}] \tag{10}$$

with $F_{i,y}$ and $F_{i,z}$ being the forces from the i-th leg acting on the body in the y- and z-directions, respectively, for an n-legged robot. Total moments and forces acting on the body are simply:

$$M_x = \sum F_{zl}.{*}\, y,\ M_y = \sum F_{zl}.{*}\, x,\ M_z = \sum F_{yl}.{*}\, z \tag{11}$$

and

$$F_x = 0, F_y = \sum F_{yl}, F_z = \sum F_{yl} - mg - c_d v_z^2 \tag{12}$$

Here, F_x, F_y, F_z are the summed forces acting on the body in x-, y- and z-direction; m is the mass of the body and g is the gravitational constant. $c_d v_z^2$ is an air viscosity term, which is small, influenced by the air viscosity and the body z-direction velocity. F_x is assumed to be zero since the x-directional translational motion is relatively small from both calculation and experiments. Furthermore, the tilting in the x- and y- direction only has small displacement compared to the overall motion of robots. However, the randomness and uncertainty in x- and y-directional tilting have large influence on the forward motion of the robot since they would change the moments of foot-terrain interaction and when individual leg impacts. Therefore, a 3-DOF interaction between body and legs is sufficient to describe the robot at small scale.

Relative Motion

The relative motion between a foot and body, foot and ground, and body and ground dictate the effects of foot impact with ground. The body motion relative to ground is important to reflect body states, which is measured experimentally over a long duration of time. The foot motion relative to ground is necessary for contact performance calculations. The foot motion relative to the body is applied to calculate the force between leg and body. During simulation, for example, once the foot motion relative to the ground is calculated, the foot motion relative to the body is needed to find the influence of foot motion on the body.

Assuming body motion and foot motion relative to ground are known from simulation, the foot motion relative to robot body is determined by the following equations:

$$z_f = z_{fb} - (z_b \pm x_b sin(\vartheta_{b,y}) \pm y_b sin(\theta_{b,x})) \tag{13}$$

$$v_{z,f} = v_{z,fb} - (v_{z,b} \pm v_{x,b} cos(\vartheta_{b,y}) v_{\vartheta,by} \pm v_{yb} cos(\theta_{bx}) v_{\theta,bx}) \tag{14}$$

$$y_f = y_{fb} - (y_b \pm x sin(\vartheta_{b,z}) \pm y sin(\theta_{b,x})) \tag{15}$$

$$v_{y,f} = v_{y,fb} - (v_{y,b} \pm xcos(\vartheta_{b,z})v_{,\vartheta bz} \pm ycos(\theta_{b,x})v_{\theta,bx}) \quad (16)$$

in which x_b, y_b, z_b, $v_{x,b}$, $v_{y,b}$, $v_{z,b}$ are the body displacement and velocity in x-, y- and z-directions relative to ground; θ_{bx}, θ_{by}, θ_{bz}, $v_{\theta,bx}$, $v_{\theta,by}$, $v_{\theta,bz}$ are the body rotation and angular velocity in x-, y- and z-directions relative to ground; z_{fb}, $v_{z,fb}$, y_{fb}, $v_{y,fb}$ are the z-directional foot displacement and velocity and y-directional displacement and velocity relative to ground; z_f, $v_{z,f}$, y_f, $v_{y,f}$ are the z-directional and y-directional foot displacement and velocity, relative to body; and x, y, z are the perpendicular distances between the body mass center and foot location, which is different for each foot. The ± signs in the equations are determined by the positive rotational direction of each axis and the location of each foot.

If the body motion relative to ground and the foot motion relative to body were given, the calculation of foot motion relative to the ground would be the backward calculation of the equations shown above. In simulation, the model is implemented using a *for* loop. Inside each loop, each foot's states determine whether that foot is in contact with ground. If so, the contact simulation is active, otherwise, the simulation mimics the free in-air motion of robot.

3.3 Model Validations

3.3.1 Parameters: Material Properties, Friction, Restitution; Identified Parameters

Detailed Prototype Design

Both centimeter-scale prototypes are designed with six legs connected to a rigid body, however each prototype employs a different design for leg geometry. The large centimeter-scale prototype (referred to as the 80 mm prototype in later sections), is designed with single-beam legs actuated with bimorph piezoelectric ceramic strips, where each beam has a foot at the tip. The piezoelectric ceramic actuators are intentionally

misaligned with the PLA leg frame (Figure 30), which generates a bending moment in the leg with vertical and lateral components. The small centimeter-scale prototype (referred to as the 30 mm prototype in later sections), uses a different leg design, where two beams are connected with a single foot at the tip. Only one of the beams is bonded with a unimorph piezoelectric ceramic strip, again causing foot motion in two directions. The major characteristics of the 3D-printed centimeter-scale robot prototypes, in comparison to a millimeter-scale version, are described in Table 5. The dynamic model for the millimeter-scale version will be modified from the work presented in this chapter. Major parameters of the millimeter-scale version are listed to show the scale difference compared to the prototypes.

Table 5 Major characteristics of the mesoscale robots and a sample micro-fabricated prototype.

Features	80 mm prototype	30 mm prototype	Millimeter-scale robot
Mass	4.4 g	379 mg	2.1 mg (unloaded) 200 mg (w/ payload)
Length	36.4 mm	16.5 mm	10 mm
Leg Number	6	6	30
Leg	27.9 x 2.2 x 2.0 mm^3	9.4 x 0.95 x 0.59 mm^3	30 μm thick
Piezo-Strip	31.8 x 3.2 x 0.48 mm^3	11 x 0.95 x 0.12 mm^3	0.9 μm thick
Foot	10.7 x 4.7 x 4.7 mm^3	3.4 x 1.4 x 1.4 mm^3	150 x150 x 70 μm^3

Vertical motion of the legs lifts the robot body against gravity, while the in-plane motion is the key feature to move the robot forward. The actuation force tilts the legs about their neutral axis to generate coupled dual-directional motion. The coefficient between the motion amplitudes in the two directions is determined experimentally. For example, the 80 mm prototype with 60V input has a vertical deflection of about 166 μm near resonance. As shown in Figure 31, the finite element analysis confirms this actuation behavior for both prototypes. The FEA gives the leg deformation within the same range of measurement. However, due to limited resolution when fabricating protoypes, the FEA

is unable to predict the exact dynamics of each individual leg. Therefore, empirically determined parameters are used to model the resonant modes of each leg.

In the full robots, a simple tripod gait is produced by actuating legs 1, 3, and 5 with the same voltage signal while the other three are actuated with the signal out of phase. For the 80 mm prototype, the actuation signal is nominally a 60V peak-to-peak square wave with 0V offset, labeled by its 30V amplitude in later discussion. For the 30 mm prototype, the actuation signal is nominally a 30V peak-to-peak square wave with no offset.

Prototype Fabrication

The robot prototypes were fabricated using a combination of 3D printed parts and off-the-shelf components. The frames of the prototypes were 3D printed with PLA. Next, six piezoelectric ceramic strips (bimorph for the 80 mm and unimorph for the 30 mm prototype,) were bonded to the robot frames with epoxy. Additional silver epoxy was used to bond wires to the piezoelectric ceramic strips for actuation. The finished prototypes are shown in Figure 30

Leg Parameter Identification

The material properties of the 3D printed legs are experimentally identified from frequency sweep testing without ground contact. This test is used to identify parameters such as elastic modulus and density of the legs as fabricated. The prototype is fixed with three different boundary conditions: 1) held from both ends on prototype body; 2) held from single end of body; 3) held at middle of the prototype body. A Laser Doppler Vibrometer (LDV) and LabVIEW are used to record the frequency response of each foot and two points on the body in vertical direction. Experiments are repeated three times.

Figure 32 shows body vertical motion and two different leg motions under constant boundary condition. Even with some coupling effects between the body and leg, the robot body has relatively little motion in the vertical direction at low frequencies, including through the first three modes of the legs. This allows the assumption of rigid body motion of the prototype body to be used in modeling. The frequency measurement of the same leg under different holding conditions (boundary conditions) appears to have

a less than 5% difference in frequency and less than 10% difference in resonance magnitude. With these two holding conditions showing similar frequency responses, this is taken to approximate the free behavior of the robot during locomotion.

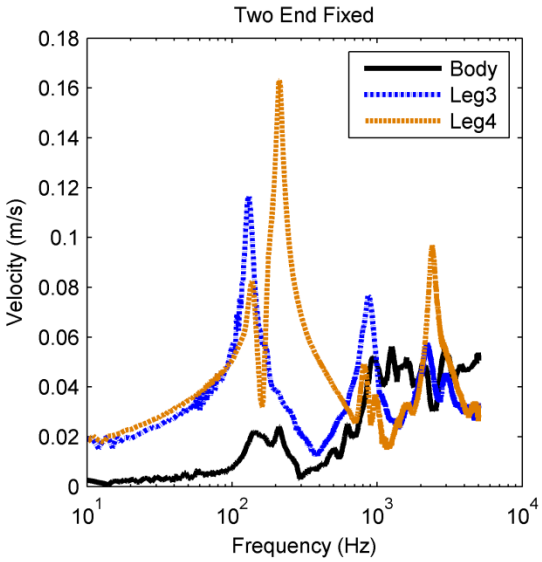

Figure 32 Frequency response of 80 mm robot body (solid line) and two legs (dashed lines) with different actuation phases under same boundary conditions, without ground contact.

Table 6 Normalized spring constant and damping coefficient for the first resonance of the 80 mm prototype robot legs.

Parameters	Normalized Spring Constant (kN/m/kg)	Normalized Damping Coefficient (Ns/m/kg)
Leg 1	752	276
Leg 2	752	358
Leg 3	678	151
Leg 4	740	207
Leg 5	1195	465
Leg 6	645	188

The leg parameters of the 80 mm prototype (found experimentally) identify the dominant resonant frequencies for six legs (Table 6), one arising in each leg. Due to fabrication variation, the response of each leg is slightly different, so the measurements were used to reconstruct the spring constant and the damping coefficient of each leg. For

this study, only the first two resonant frequencies of the legs are considered in the model simulation. The relationship between vertical and lateral motion of the legs is also characterized for the four outer legs by measuring dynamic motion in the lateral direction with the LDV. A similar identification process is applied to the 30 mm prototype.

Coefficient of Friction and Restitution

The contact properties of two types of materials (wood and metal) were tested as the ground for the robot prototypes. The coefficient of friction is determined with a simple sliding test on surfaces of different materials (Table 7). The coefficient of restitution is determined via measurement with LDV. The prototype is trapped by placing a large mass in front of robot to prevent motion in all other directions besides the z-direction (vertical). Sudden changes in z-direction velocity are recorded at least five separate times for each prototype leg, and all data is combined to calculate the average value of coefficients (Table 7).

Table 7 Coefficients of friction and restitution for two types of surface materials

Surface Materials	Coefficient of Friction	Coefficient of Restitution
Wood	0.27	0.59
Metal	0.21	0.57

3.3.2 Model Results vs. Experimental Results

To validate the dynamic model, the simulation results for leg and body motion based on the parameters in section 3.1 for are compared to experimental results for both 80 mm and 30 mm prototypes under several forcing conditions. The 80 mm prototype is used primarily to validate the vertical motion of the legs and overall walking speed, and the 30 mm prototype is used primarily to validate the vertical motion of the body. The walking speed of each robot is characterized by actuating near resonance and recording the resulting motion with a camera. From the videos, the position of the robot is tracked in each frame, and the numerical derivative is computed to calculate the average forward velocity, with error range. These measurements are then compared to simulation results.

Supplementary Video S1 shows a representative sample of robot walking and subsequent velocity measurements for both prototypes. The validation study begins with the robot leg motion in the vertical direction, using the 80 mm prototype, where body motion is largely uniform. Robot body motion in vertical direction then shows some interesting phenomena in the 30 mm prototype, discussed next. Finally, the robot walking velocity predicted from the dynamic model is assessed using the 80 mm prototype, which is less effected by external wiring than the 30 mm robot. The comparison shows the influence from many design parameters towards the robot motion.

Leg Vertical Motion

The time domain contact responses of one leg of the 80 mm prototype under different input voltages are shown in Figure 33 from experiments and simulation. The robot model accurately captures general trends in contact duration, timing, and foot step amplitude in the vertical direction, for which high fidelity measurement can be made directly with the LDV. The largest source of disagreement is the repeatability of motion amplitude at 30 V input, which may be influenced by body vibration modes not included in the current model. Small variance in motion amplitude between model results and test results with 40 V actuation is potentially caused by the influence of body motion.

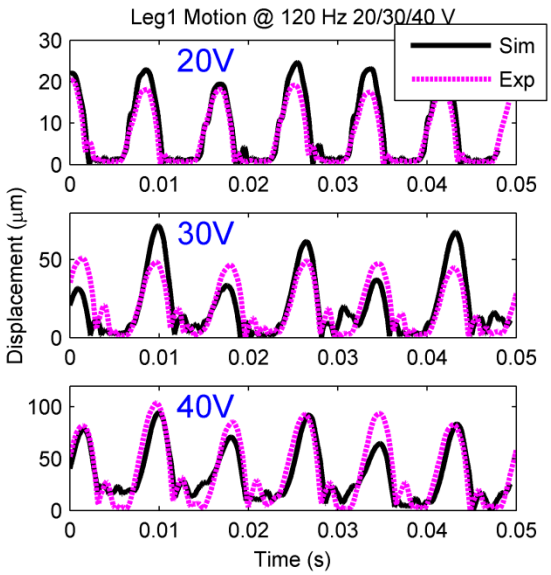

Figure 33 Sample experimental (black solid line) and simulated (pink dash line) time response of the 80 mm robot prototype vertical leg motion at different actuation voltages (20/30/40 V).

Robot Body Motion

The 80 mm prototype has a larger mass, which leads to very small body motions, so modeling of the body's vertical motion is validated with the 30 mm robot prototype. Characteristic time domain responses of the vertical body motion of the 30 mm prototype are shown in Figure 34. The measurement was performed with a square wave actuation signal at 1400 Hz with an amplitude of 30 V. Notably, as robot mass is reduced, the manner in which the robot's feet and ground interact is changed dramatically. Rather than producing foot impact at each actuation cycle, (which occurred consistently for the 80 mm prototype), both simulation and experiments show that the body of the robot will stay in air for several leg cycles between foot impacts. Due to the extended time the body spends in air, the air damping term in (12) is considered for the 30 mm prototype. However, simulations for 80 mm prototype show that the air damping is negligible due to large prototype weight and limited vertical in-air motion. When the experimental and simulated results are compared, the amplitudes match for both the fast leg and slower body oscillations. To better quantify the in-air phase of the motion, a Fast Fourier Transform (FFT) is performed on the time series data, as shown in Figure 35. The first peaks of the FFT from the simulation and experiments are both located within the range of 50 to 100 Hz. In other words, the model successfully predicts the approximate range and frequency of impact events, even as robot scaling leads to more complex interactions between the robot and the ground. This phenomenon is similar to behavior previously observed in a magnetoelastic impact motor with similar modeling applied, which also showed bouncing of the rotor every few cycles of stator vibration [6].

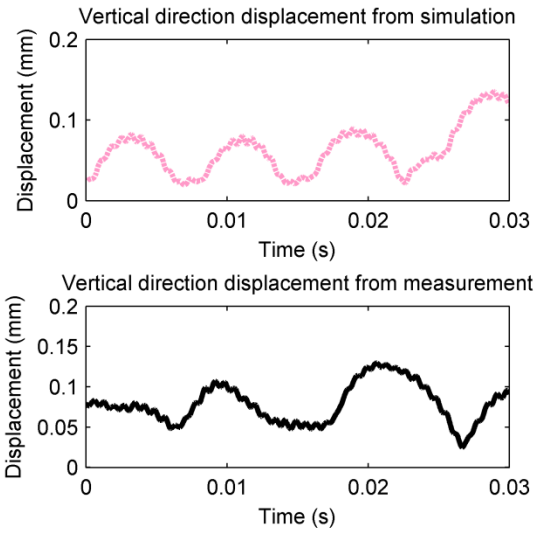

Figure 34 30 mm prototype body vertical motion: measurement (lower) and simulation (upper).

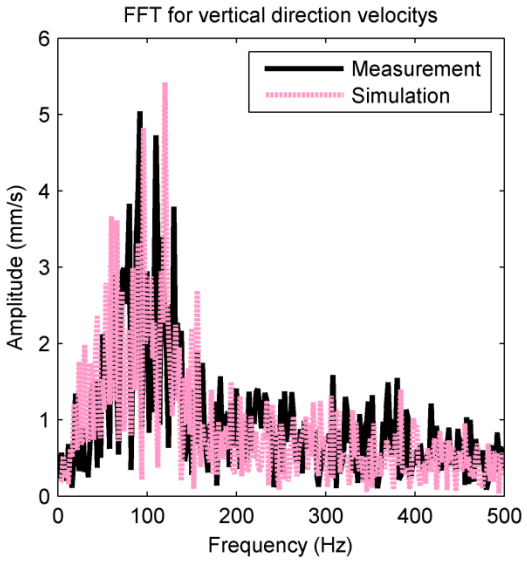

Figure 35 Fast Fourier Transform of 30 mm prototype body vertical motion: measurement (lower) and simulation (upper) shows similar distribution of frequency content, with large body "bouncing" motion at lower frequency than leg actuation.

Robot Velocity

Locomotion experiments are designed to measure the relationship between actuation voltage, actuation frequency, ground condition, and average robot velocity. The forward motion of the 30 mm prototype is significantly influenced by its power cable, so forward velocity of the 80 mm prototype is primarily examined. However, the simulated

forward velocity of the 30 mm prototype, 4 mm/s, does lie well within the experimentally-observed velocity range, 2 mm/s to 10 mm/s.

The forward velocity of the 80 mm prototype was characterized using input frequencies primarily between 110 Hz and 140 Hz, because the first resonance modes of all six legs are located close to or in this range. The input voltage amplitude ranged from 15 V to 45 V. Less than 15V produced minimal movement from the robot, and 45V was the upper limit of the experiment setup. Simulations using the dynamic model were also generated in these ranges. Comparison between simulations and experimental results shows that the direction of robot motion is the same. Error bars in simulation results are generated by 10 simulations with randomly generated individual leg spring constants and motion amplitudes, distributed according to the variability in the motion of experimentally-observed legs, as measured during testing without ground contact. These error bars are intended to illustrate the potential variability in robot locomotion given the limitations of the accuracy with which nominal robot leg dynamics could be identified.

Figure 36 shows the simulated and measured velocities on the wood surface under different actuation frequencies, when the actuation voltage was fixed at 30 V. Figure 37 compares behavior on the metal surface, showing representative trends with respect to voltage, when the actuation frequency was fixed at 140 Hz. Predictions for robot velocity generally capture key trends in robot performance, though behavior is not as closely captured as was observed for vertical motion alone. Most importantly, velocity trends near the primary resonant peak are well-captured, but un-modeled dynamics take on more substantial roles at other frequencies. With respect to voltage, both experiments and simulation predict a local maximum for velocity. The existence of this local maximum is attributed to body motion starting to influence leg interaction, as shown in the previous leg contact measurements (Figure 33). Body motion breaks up the timing between sets of legs in the tripod gait, but speed increases again as a function of voltage when individual leg displacements become sufficiently large to overcome this effect. Also Figure 37 shows the importance of multi-mode leg modeling, as a single mode model produces a completely different velocity trend.

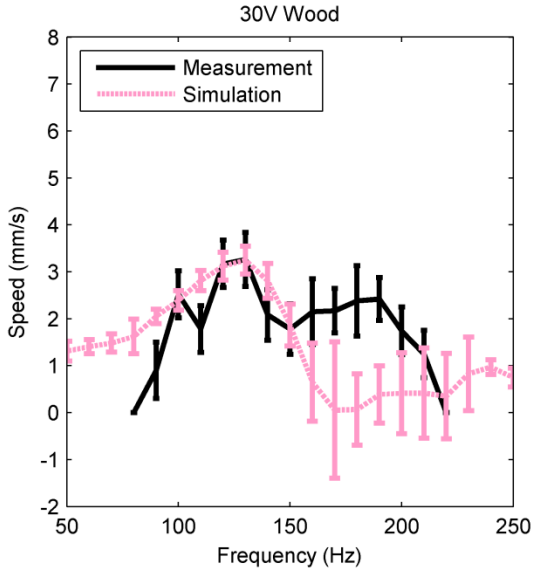

Figure 36 The relation between actuation frequency and robot average velocity at 30 V; black solid line is the measurement and red dash line is simulation.

The importance of including the second resonance mode in the dynamics is also illustrated in Figure 37. The trend in velocity with respect to actuation voltage follows a completely different trajectory than experiments when simulated using only the first resonance mode. The addition of the second resonance mode to the simulation resulted in more accurate dynamics estimation. Additionally, higher frequency modes (from third resonance) contribute a negligible portion of the overall motion for the robot size scales investigated, especially for displacement. If a hypothetical robot design did show sensitivity to higher modes, it should be noted that the dynamic model in this work is capable of including any further resonance.

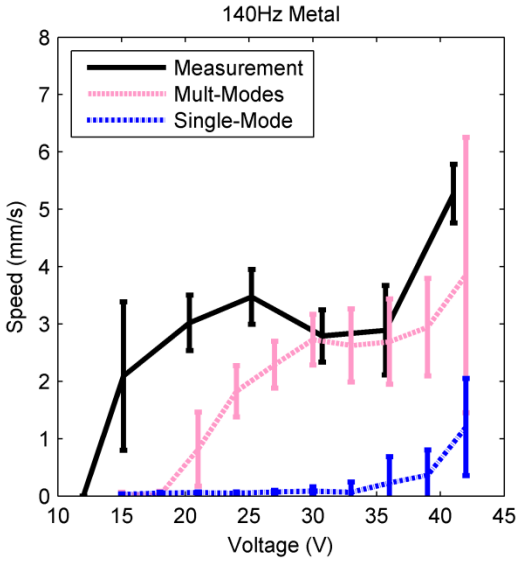

Figure 37 The relation between actuation voltage and robot average velocity at 140 Hz; black solid line is the measurement, red dashed line is the simulation with multiple modes and lowest blue dotted line is the simulation with first resonance only.

Furthermore, the effect of a payload is measured and simulated (Figure 38). The 80 mm prototype is loaded with payloads of various mass, with walking conditions chosen to be 130 Hz, 30V actuation on a wood surface. The mass ratio is the total mass including payload and prototype itself over the mass of prototype alone. Based on our measurements, when the 80 mm prototype is unloaded sitting on the ground, only 4 feet of the prototype have good contact with ground to take nominal gravity load. If we apply load to the prototype, more feet will have contact with ground under nominal gravity load, until all 6 feet have solid ground contact. Therefore, the measured robot velocity should sit in the range limited by these two conditions, 6 feet or 4 feet with nominal gravity load. These two simulation trends are shown along with experimental results in Figure 38. From both simulated and measured results, the prototype could achieve a payload more than its own mass by trading off forward velocity. This ensured its potential to be further integrated with power and control system.

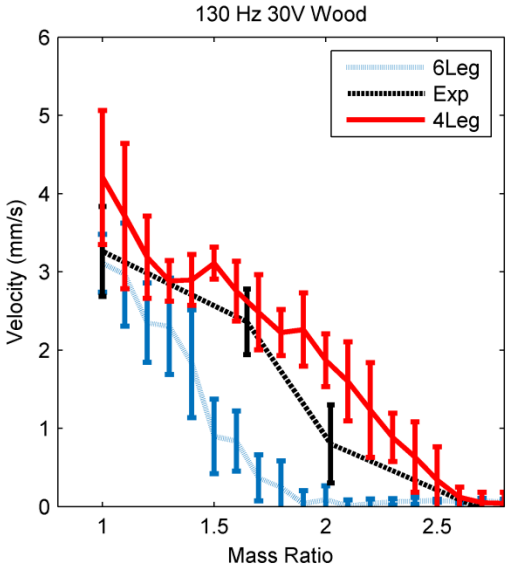

Figure 38 The relationship between payload mass ratio and average robot velocity at (80 mm robot, wood surface, 30 V actuation amplitude, 130 Hz actuation frequency); black dash line is the measurement, red solid line is the simulation with 6 legs under nominal gravity load and lowest blue dotted line is the simulation with 4 legs under nominal gravity load.

The path of both prototypes is curved in experimental tests since the legs are not perfectly symmetrical in the fabricated prototypes. Simulation results shown in this chapter assume uniform leg geometries but require material properties be measured experimentally for good agreement with walking experiments. Including leg variation has a very limited effect on forward and vertical velocity predictions (less than 10%), but can predict direction of curved walking paths (though with less accuracy).

These results do highlight some of the limitations of the proposed model. First, the discrepancy of the velocity in the frequency domain mainly occurs around 180 Hz, as shown in Figure 36, where an additional peak appeared for a subset of the legs (Figure 32). This peak appears to be a body mode of the robot chassis, as opposed to vibration modes local to the individual legs. Conceptually, treating the entire robot as a compliant body would allow this mode to be captured and improve predictions of robot behavior. However, this increase in accuracy would come at a substantial increase in model complexity due to a larger number of modes to be accounted for at each leg, and

difficulty of analytically modeling chassis deformation. Second, with respect to voltage, while the qualitative behavior of local maxima is successfully captured and velocities are mostly within the margin of error, the predicted locally optimal voltage is significantly different. This could be due to neglecting nonlinearities in the piezoelectric actuator response or some adhesion effects at the robot foot.

In addition to actuation voltage and frequency, the motion amplitude ratio between vertical and axial motion was examined, as shown in Figure 39. The ratio of y- and z- direction motion is determined as the maximum free motion amplitude in z-direction over y-direction. Given a fixed vertical motion, an increase in axial motion is correlated with an increase in the robot's forward velocity, as expected, but with a more pronounced local optimum. These results indicate the importance of characterizing the correct ratio between two directional motions. The influence of variations in spring constants and damping coefficients of each leg are shown as error bars in Figure 35 to Figure 39Figure **38**. Higher actuation voltage generally produces a large error range since the absolute value of the motion amplitudes is larger with the same error range. Also, the error in actuation frequency away from resonance is larger than the one around resonance. Moreover, the robot is able to move in the reverse direction as indicated by simulation. This phenomenon was also observed in experiments, but not quantitatively measured.

Similarly, the effect of foot-terrain interaction parameters is shown in Figure 40. The robot's velocity drops substantially if the coefficient of friction drops under 0.1, which indicates the existence of slippage between the robot foot and ground. Above this threshold, the exact coefficient of friction has little influence, as the stationary friction force between the feet and ground is nearly always less than the maximum friction force that could be provided. Meanwhile, low coefficients of restitution are predicted to lead to higher robot velocities, because lower vertical velocities after contact will cause the foot to stay in contact with ground longer. Longer ground contact allows friction to actuate the robot forward, provided that the in-plane and out-of-plane motion are coupled in the axes assumed by this work. Low coefficients of restitution are also related to plastic contact between the foot and ground. Regarding the coefficient of restitution and friction, both types of materials we used as ground condition share close value.

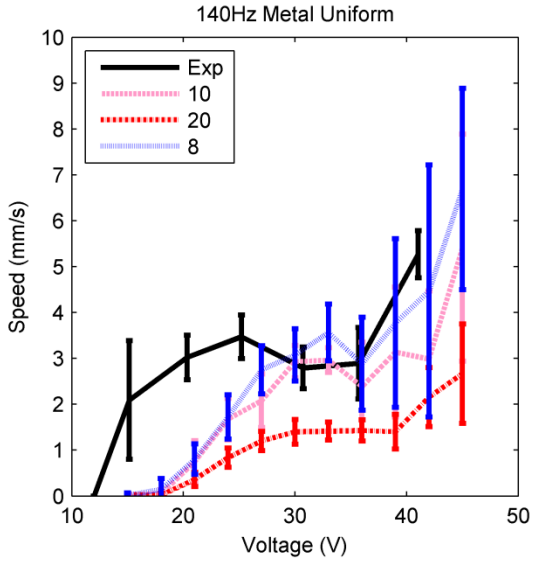

Figure 39 Simulated relationship between the ratio of y- and z- direction motion on robot average velocity (80 mm robot, 140 Hz, metal surface).

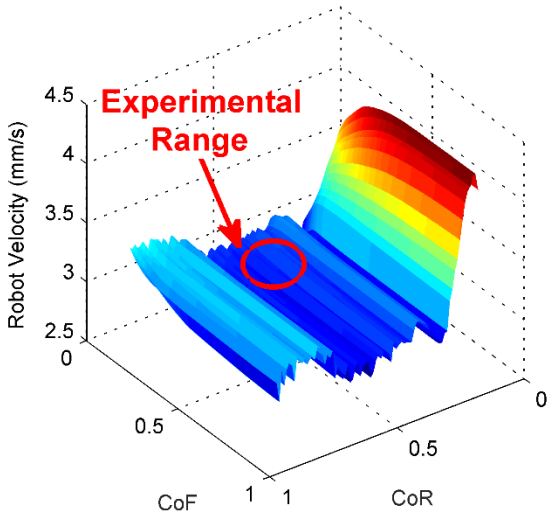

Figure 40 Simulated relationship between coefficient of friction (CoF), coefficient of restitution (CoR), and average robot velocity (80 mm robot, 120 Hz); experimentally validated coefficient range is indicated.

3.4 Discussion and Conclusion

A model is presented for dynamics of small, elastic walking robots. The model includes 3-DOF rigid body motion and 2 DOF flexible leg motion with multiple modes to capture trends in robot leg motion and velocity. The interaction between the robot and the ground is modeled using simple coefficients of friction and restitution. To validate this model, two different centimeter-scale robot prototypes are fabricated, both of which can be represented by the model. The prototypes are actuated by piezoelectric ceramic strips bonded to a 3D printed body, and are experimentally characterized in terms of leg and body dynamics as well as walking speed. The velocities of the robot prototypes under varying actuation voltages and frequencies near the legs' resonant frequencies are measured to be around 3 mm/s for both prototypes, which are in the same range as those simulated by the dynamic model after robot parameters are identified experimentally. The payload effect is also considered and validated with this model.

Other experimentally-observed features that are captured well by the model include: 1) vertical leg motion trajectories and ground interaction trends; 2) bouncing effects, where large vertical body motion has multiple significant frequency components at frequencies lower than the leg actuation frequency, as exhibited in the 30 mm prototype; 3) velocity trends with changing voltage, when a sufficient number of vibration modes are accounted for in the leg model; 4) the existence of a local maximum velocity with respect to voltage at some frequencies, though the maximum occurs at slightly higher voltages in simulation than in experiments. Simulated robot velocity trends with respect to the robot legs' vertical-axial motion ratio, coefficient of friction, and coefficient of restitution, are also reported. Limitations of the model include omitting the possibility for body deformation to simplify the model, and the need for a significant amount of leg and terrain model information to accurately predict robot behavior.

As a structure for future micro-robot development, this work provides: 1) a generalized model for multiple-legged systems that includes both rigid body and compliant actuation motion; 2) accommodation of leg motion with multiple modes and DOF while body motion has multiple DOF; 3) good performance with high-frequency, lightly-damped actuation. These features are anticipated to be common in future millimeter-scale robots based on microfabrication processes, when operated in dynamic walking or running gaits.

Other phenomena that may be added in future work for even smaller robots include effects such as squeeze-film damping, adhesion or stiction forces at robot feet, and other small-scale forces.

CHAPTER 4 Dynamic Structural and Contact Modeling for a Silicon Hexapod Micro-Robot

4.1 Introduction

Microscale walking robots, typically with maximum dimensions on the order of a centimeter or smaller, have been proposed or developed over recent decades based on a variety of electromechanical actuation principles, including electrostatic [41], electrothermal [25, 107, 108], magnetic [35], shape-memory alloy [50] and piezoelectric [45] transduction. Thin-film piezoelectric ceramic actuators [48], as a class of smart materials for micro-electromechanical systems (MEMS), share several advantages with bulk piezoelectric materials. These include large work densities and substantial force generation. As thin-film, piezoelectric actuation can also be achieved with modest actuation voltages (typically 5-20 V) and over comparatively large deflections via beam bending. Drawbacks of thin-film piezoelectric microactuators include complicated fabrication requirements, limitations on material compatibility with some processes or other materials, and relative fragility compared to many semiconductor or polymer materials. Recently, it was shown that some degree of fragility and processing complexity could be compensated by integrating lead-zirconate-titanate (PZT) thin-films with high-aspect ratio polymer microstructures and coatings based on parylene-C after PZT deposition [45]. Parylene-C films and micro-beams were shown to help protect the fragile piezoelectric layer and amplify actuator stroke in compliant mechanisms, producing more robust thin-film PZT micro-robots than previously demonstrated.

A further benefit of thin-film piezoelectric actuation for micro-robotic applications is that these actuators can achieve high bandwidths with low damping ratios,

which raises possibilities for dynamic or resonant gaits during robot locomotion. However, it has been previously observed that the interaction of elastic resonant behavior in micro-structures and impact dynamics between small micro-actuators or micro-robotic legs and underlying terrain can give rise to highly varying, complex, and sometimes even nearly-chaotic dynamic behavior [43, 44, 63, 109]. The authors have previously described a multiple-modes model to explain the dynamics of micro-robots with similar actuation principle and materials selection, but at the centimeter-scale where small-scale forces have limited effect on foot-terrain interaction [109]. The modeling process in this work is guided by previous models for centimeter-scale robots, but converts the system dynamics to a hybrid dynamic model that can account for the distribution of modal motion in two directions for each mode and additional microscale ground interaction phenomena that become significant at micro-scales. Preliminary modeling based on this approach had shown reasonable agreement between identified robot properties and global robot motion (body vertical and lateral displacements), but model refinements and new validation based on experimental measurements of individual robot foot behavior in this work provide further insight into the influence of individual foot-terrain contacts on cumulative robot locomotion.

There have been several prior studies of fundamental dynamic concepts related to small-scale walking or running locomotion. This includes studies originating in locomotion of biological organisms, such as insects [110], as well as tests of robots intended to operate on these principles, typically at the size-scale of several centimeters [110, 111]. These works typically develop a lumped-parameter model for leg dynamics, and apply it with relatively simple ground interaction modeling, alternating between firm contact and motion of the robot feet in air. This reflects basic concepts of legged robot dynamics such as their foot-terrain and foot-body interaction, which have some different features when examining dynamics of even smaller, silicon-micromachined robots. Regarding the former, foot-terrain interaction can be characterized regardless the number of legs in a robot, but it is significantly influenced by the scale of robots. At the microscale, nonlinear air damping and adhesion become significant factors that should be modelled accurately to estimate the robot dynamics. The foot-body interaction, meanwhile, in micro-machined structures depends significantly on elastic structural

resonances. These may exhibit coupling between vibration modes in the legs and the body itself, or at least coupling of resonances in multiple legs that may vary based on the number and location of legs with respect to robot body. Again at scales of several centimeters, elastic vibration has been used to generate piezoelectric robot locomotion, but the further coupling of these dynamics with foot-ground interaction at small-scales has not been studied in detail [44, 47, 111-113].

Several contributions toward the understanding of millimeter-scale micro-robots are then included in this work. At a high level, while prior works have explored effects of small-scale forces and impacts of individual micro-robot legs or meso-scale representations, those works had yet to validate modeling of multi-legged dynamic impact behavior on millimeter-scale, resonance-driven micro-robot locomotion with significant small-scale force contributions. To effectively capture robot motion, multiple vibration modes are included in this model at all legs: three modes in the robot structure evaluated here, with further extension of modes possible with this modeling technique. Also, for each vibration mode, the direction of motion is considered, so the motion in lateral and vertical directions are coupled, where prior modeling assumed minimal directional coupling between modes. The dynamics of adhesion and rest between the feet and ground are further distinguished for a better understanding of the adhesion influence on micro-robot dynamics. From this model, the robot forward motion and individual foot motion of future autonomous robots may be better predicted given specific design parameters and pre-fabrication analysis.

Model validation during this study is performed using a millimeter-scale micro-fabricated hexapod robot prototype. Figure 41 shows examples of these micro-robots before and after detachment from a silicon chip. To interpret both active and passive micro-robot dynamics, a dynamic model is constructed that includes: nonlinear foot-terrain interactions, coupled structural resonances of the robot's actuators and structures, and rigid body motion of the robot chassis with multiple degrees of freedom. The micro-robots as initially fabricated in the silicon chip are suspended by silicon tethers used to support the micro-robots through their fabrication process, which also provide electrical signals for characterization. Several locations on micro-robots are measured under

different loading conditions to identify robot structural dynamics. For ground interaction testing, the micro-robot is detached from its chip and motion is excited on other surfaces. Since the detaching process breaks the electrical connection to the micro-robot, out-of-chip dynamics are measured under external vibratory actuation from a shaker. The robot motion simulated by the dynamic model is compared with the empirical results to evaluate the model with respect to robot translation due to vibratory response of its legs and with respect to small-scale force effects on this motion.

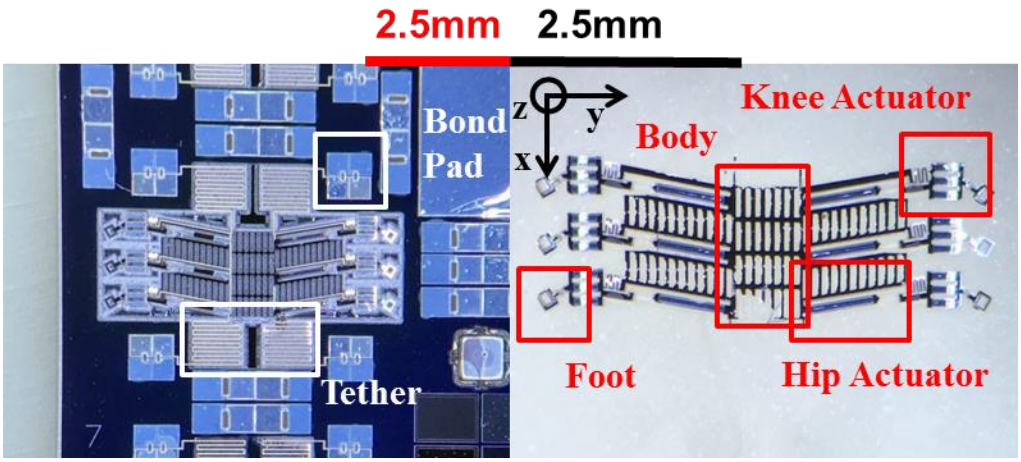

Figure 41 Photo of (Left) a silicon die containing tethered hexapod micro-robots; and (Right) sample hexapod micro-robot detached from its wafer; the coordinate system for dynamic model is also labeled; with the z-direction pointing out of plane.

4.2 Robot Design

An example of the micro-robot design used for dynamic testing is shown in Figure 41, both before and after removal from the silicon wafer in which it is fabricated. Details on robot actuator design, fabrication, and testing have been presented in [48, 114]. In brief, the robot consists of a central silicon chassis or body (30 μm thick silicon), surrounded by six nominally identical legs. Each leg contains two actuation elements based on thin-film piezoelectric actuators. The piezoelectric actuators are formed on a silicon dioxide base layer (0.5 μm) with two electrode layers of platinum (0.1 μm and 0.2 μm) on either side of the PZT thin-film layer (1.0 μm). The hip actuator consists of a PZT

unimorph constrained to act in lateral contraction [45, 115], coupled to a high-aspect-ratio parylene-C microbeam that leverages contraction into in-plane rotation. The knee actuator consists of three PZT unimorphs acting in pure bending to rotate the robot foot out-of-plane. In-plane and out-of-plane actuators are connected in parallel electrically and thus must actuate simultaneously, while legs are addressed either individually or in-pairs from electrical interconnects on the robot body. Conceptually, robot locomotion would be based on alternating actuation of legs, say in a tripod gait, using variations in natural frequency and response time between lateral and vertical motion at the foot to create elliptical-type foot motions. Conceptual foot motion with ground contact when the PZT elements in each leg are actuated in parallel is demonstrated with Figure 42. In a prototypical cycle, the robot foot will spend time both in contact with ground and moving in air within a single actuation cycle, or robot "step," though substantial variation in behavior will be seen in the presence of contact dynamics and small-scale forces. Tested static amplitudes at the robot foot are about 50-100 μm at actuation voltages of 10-20 V. Much larger foot displacements are possible near resonance, as measured damping ratio for the leg structures is near 0.05, but maximum range-of-motion before failure has not been evaluated.

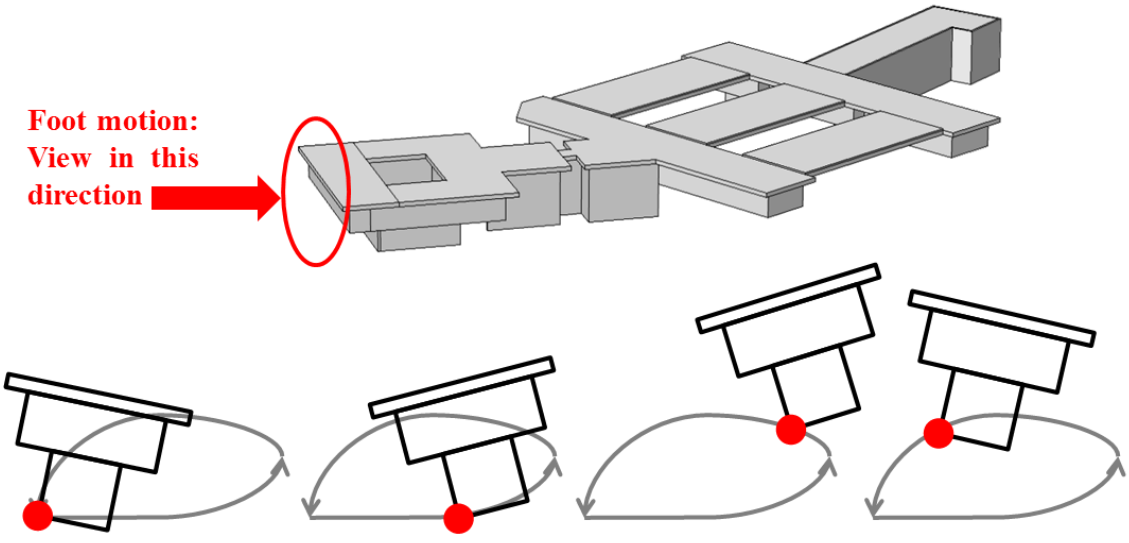

Figure 42 Side view of nominal robot foot motion when ground is present; the foot remains stationary with respect to the ground for a certain period of time when actuated downward and moves in air when actuated upward.

As fabricated in a silicon chip, serpentine silicon springs or tethers support the robot body and provide electrical signals to the robot legs. This allows characterization of active robot leg motion, but does also influence robot dynamics, as compliance of the robot body or chassis itself is constrained by the tethers, and a rigid body mode of the entire robot oscillating on the tethers is introduced. The following sections examine the various resonant vibration behaviors that occur across the robot legs and body, and use this information to interpret forward robot locomotion in passive walking on a vibrating field after silicon tethers have been severed and the robot is permitted to translate freely across a surface.

4.3 Dynamic Model

A model for micro-robot dynamics is generated as a hybrid dynamic system. In this process, micro-robot dynamics are first studied with finite-element analysis (FEA) at the individual leg level. Using FEA results and in-chip characterization of the micro-robots, the full dynamic model is built to account for multiple resonant modes of the leg-foot system, nonlinear foot-ground interactions, and body motion in five degrees of freedom. The resulting dynamic model includes two parts to completely describe the robot motion. The first part is a leg-foot model with three different dynamic motion modes ("dynamic modes" used here in a hybrid system sense as opposed to "vibration modes" or "resonant modes" associated with the elastic compliance of the robot). These dynamic modes are an in-air mode, an impact mode and an adhesion mode, to cover possible robot foot motions. The second part is a body model to describe the robot body/chassis motion in five degrees of freedom, requiring appropriate motion state transformations between relevant reference systems. The dynamic model is then used to predict and compare robot in-plane and out-of-plane motion when actuated by external vibration from a shaker.

4.3.1 Preliminary FEA Modeling

A dynamic model of the micro-robot's legs is first constructed in COMSOL finite element analysis software to understand the frequency response of both hip and knee actuators. Both actuators are simulated to predict the structural resonance. With nominal robot design parameters and fabrication results as reported in [114], the first lateral resonant frequency of the hip actuators is simulated to be 498 Hz; the first vertical frequency of knee actuators is 3671 Hz. Figure 43 shows the simulated structural deformation of these first two modes of the robot legs. It is worth recalling that both actuators in an individual leg are connected electrically and thus are actuated simultaneously. While it is not possible to stimulate both actuators at their maximum motion amplitude simultaneously with a single-frequency actuation signal, it is possible to actuate the robot leg-foot system various vertical and lateral motion ratios by choosing the actuation frequency carefully. The ratio of vertical to lateral motion at each resonance, as motions of the two actuators are not perfectly orthogonal at their respective resonances, and thus vertical to lateral motion ratio at other frequencies, is a critical factor in generating robot locomotion from this architecture. The vertical to lateral motion ratio was determined with COMSOL to be 1:15 at the first lateral resonance and 17:1 at the first vertical resonance. These ratios are used to model the dynamics of micro-robots when associated leg resonances are excited by impact after the robot is detached from the wafer.

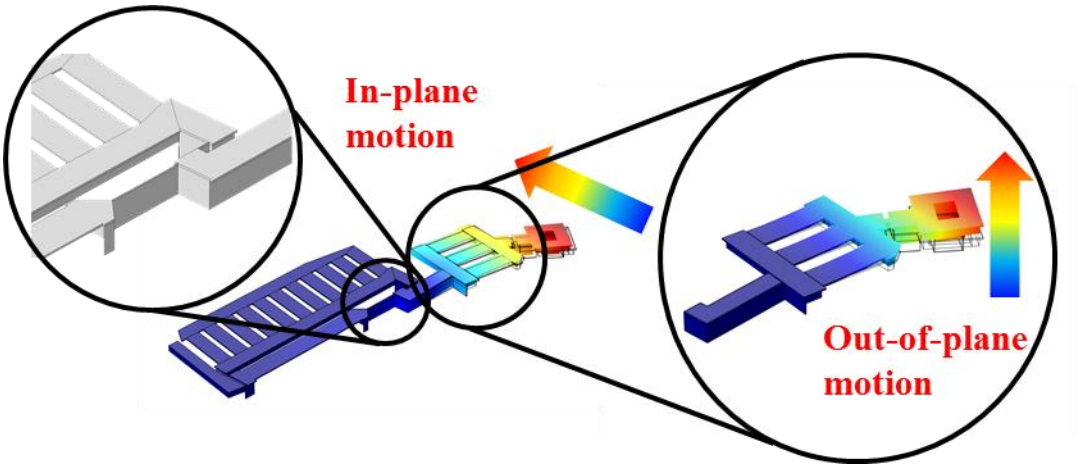

Figure 43 (left) The compliant structure of a sample robot leg with a high aspect ratio link connecting the hip and knee actuators; also shown are the COMSOL-simulated mode shapes of the first lateral mode of the leg (middle), originating in pivot about the hip

actuator, and the first vertical mode of the leg (right), originating in bending of knee actuators.

4.3.2 Hybrid Leg Dynamics

Individual robot foot motion in the time domain is distributed into 3 dynamic or hybrid modes. The first dynamic mode describes the free, in-air motion of a robot leg. This mode shows up in both in-chip and out-of-chip motion. No foot-terrain contact is included in this mode, so the dominant external force from ground interaction is the air damping force at the microscale, i.e. squeeze-film damping. Mode 2 describes the impact phenomena of the robot foot. If the robot foot is not capable of leaving the ground because of adhesion forces or gravity, modes 3 and 4 are used to describe leg motion. Again we note that structural dynamics in each mode originate in the modal vibratory dynamics of the system; as such, when referring to modal dynamics associated with specific resonances, we will refer to "vibration modes," and to "dynamic modes" when referring to the three modes of motion comprising the hybrid system model.

Mode 1: Leg motion in air

The free in-air motion of the robot foot is described with a state-space model. The in-air motion represents the foot motion when tested in-chip, as well as out-of-chip motion after bouncing (mode 2) or release from ground after adhesion (mode 3). The vertical and lateral motion for each mode is coupled with a relation defined by preliminary FEA results. The state-space form in both lateral and vertical directions shares a similar format as follows:

$$\begin{bmatrix} X_{1,j+1} \\ \vdots \\ X_{n,j+1} \end{bmatrix} = \begin{bmatrix} A_1 & & 0 \\ & \ddots & \\ 0 & & A_n \end{bmatrix} \begin{bmatrix} X_{1,j} \\ \vdots \\ X_{n,j} \end{bmatrix} + \begin{bmatrix} B_1 \\ \vdots \\ B_n \end{bmatrix} F_{ext} \tag{1}$$

$$A_i = \begin{bmatrix} 0 & 1 \\ -k_i & -b_i \end{bmatrix};\ B_i = \begin{bmatrix} 0 & 0 \\ \frac{1}{m_{i,imp}} & \frac{1}{m_{i,dis}} \end{bmatrix};\ X_{i,j} = \begin{bmatrix} x_{i,j} \\ v_{i,j} \end{bmatrix} \tag{2}$$

$$\begin{cases} z_i = C_{z,i} x_i & v_{zi} = C_{z,i} v_i \\ y_i = C_{y,i} x_i & v_{yi} = C_{y,i} v_i \end{cases} \tag{3}$$

in which k_i and b_i are the spring constant and damping coefficient for resonance i, normalized by the effective mass of that vibration mode; $x_{i,j}$ and $v_{i,j}$ are the displacement and velocity for the i-th vibration mode at j-th time step. Vibration mode matrices A_i are constructed independently for vertical and lateral directions based on resonant frequencies with dominant influence in those directions. It should be noted here that the robot motion states in the state space form represents the robot foot motion with respect to the robot body. The displacement and velocity in the lateral (y-) and vertical (z-) directions (respectively: z_i, v_{zi}, y_i, and v_{yi}) are expressed as proportional to a combined modal displacement and velocity, x_i and v_i, using motion coupling coefficients $C_{z,i}$ and $C_{y,i}$. The motion coupling coefficients measure the amount of motion in lateral and vertical direction contributed by i-th mode of the leg: C_z is the ratio of motion in the vertical direction to the overall motion of the i-th mode, and C_y is the ratio of the motion in the lateral direction to the overall motion of the i-th mode.

$\mathbf{F}_{ext}$ is a vector of external forces acting on the leg and foot, divided into those that are concentrated at the foot and those that are distributed over the leg; and $m_{i,imp}$ and $m_{i,dis}$ are the effective mass for the i-th mode with respect to those point and distributed external forces. Forces able to be approximated as distributed over the leg and/or foot include gravity on the leg (m_l) and foot (m_f), nonlinear air damping ($\mathbf{F}_{damp}$), and effective internal piezoelectric force ($\mathbf{F}_{act}$):

$$\mathbf{F}_{ext} = [\mathbf{F}_{act} + \mathbf{F}_{damp} + m_l\mathbf{g} \quad m_f\mathbf{g}]' \tag{4}$$

in which $\mathbf{g}$ is a gravitational vector. Robot foot velocity (v_{zfb} and v_{yfb}) and displacement (z_{fb} and y_{fb}) relative to the robot body arising from the combined effect of vibration modes included in the model are expressed as:

$$\begin{cases} v_{zfb} = \sum_i v_{zi} & z_{fb} = \sum_i z_i \\ v_{yfb} = \sum_i v_{yi} & y_{fb} = \sum_i y_i \end{cases} \tag{5}$$

The foot velocities (v_{zfg} and v_{yfg}) and displacements (z_{fg} and y_{fg}) relative to ground take the body motion into account as well. Equations 13 -16 in prior work [109] explains the conversion between velocity and displacement with respect to ground (referred to as

vz_{fg}, vy_{fg}, z_{fg}, and y_{fg}) versus motion relative to the body (v_{zfb}, v_{yfb}, z_{fb}, and y_{fb}, as above).

At the current millimeter robot scale, some other nonlinear and/or small-scale forces may affect robot dynamics, even in the absence of ground contact. The most influential of these is found to be nonlinear effects of air flow during motion of the leg near the ground (**F*damp***), which is modeled as an air drag force (F_{db}) and an effective squeeze film damping force (F_{sb} for the robot body and F_{sf} for the robot foot), acting in the vertical direction and nonlinearly dependent on distance from ground [62, 87]. The air damping affects both the robot feet and body, calculated with different geometrical parameters and velocity profiles. The coefficients for the robot body and each foot are calculated separately. These forces are expressed as:

$$\begin{cases} F_{sf} = \frac{b_{gf} v_{zfg}}{z_g - z_{fg}} \\ F_{sb} = \frac{b_{gb} v_{zb}}{z_g - z_b} \\ F_{db} = \alpha {v_{zfg}}^2 \end{cases} \quad (6)$$

in which v_{zfg} and v_{zb} are the vertical velocity with respect to ground for the robot foot and robot body, respectively; b_{gf} and b_{gb} are the coefficient of squeeze film damping for the robot foot and body, respectively, calculated from their component geometries, air properties, and nominal distance from ground; z_g is the ground height; and z_{fg} and z_b are the vertical height of robot foot and robot body.

Mode 2: Impact

Mode 2 represents impacts between foot and ground. Comparatively instantaneous foot-terrain interaction is the fundamental feature of this mode. The impact between foot and ground is approximated by a coefficient of restitution model:

$$v_{zfb,f} - v_{zg,f} = -(v_{zfb,o} - v_{zg,o}) c_r \quad (7)$$

in which the velocity of robot foot before ($v_{zfb,o}$) and after ($v_{zfb,f}$) impact are related to shaker ground velocity before ($v_{zg,o}$) and after ($v_{zg,f}$) impact according to a coefficient of restitution, c_r. In (7), the robot foot velocity is relative to the fixed ground condition,

which is calculated from robot body motion and foot motion with respect to the robot body, from (5).

Friction effects can influence contact interactions during this interaction, as sufficiently light vertical contact can result in slip of robot feet in the lateral direction during this interaction [109]. However, unlike robot motion with an electrical input, which can directly drive lateral actuation, shaker motion is in the vertical direction alone. As it excites the individual legs' motion, coupling between forces in the two axes produces lateral motion of the foot with little opportunity for slip, so friction is treated as sufficient to maintain fixed contact laterally during ground interaction in the current testing scenario. Therefore, the lateral velocity of a robot foot after impact is enforced to be zero when impact happens, as a combination of two non-zero lateral modal velocity. Because motion in the vertical and lateral directions is coupled, for a post-impact vertical velocity, the mode velocity is estimated as if only the first vertical and lateral modes are influenced by impact, following [63]. Using the motion coupling coefficients (C_z and C_y) for two modes (subscript 1 for first vertical mode and 2 for first lateral mode) and vertical velocity after impact ($v_{zfb,f}$), the overall velocity for the first vertical (v_z) and lateral mode (v_y) after impact are:

$$\begin{cases} v_z = -\frac{C_{z,2} v_{zfb,f}}{C_{y,1} C_{z,2} - C_{z,1} C_{y,2}} \\ v_y = \frac{C_{z,1} v_{zfb,f}}{C_{y,1} C_{z,2} - C_{z,1} C_{y,2}} \end{cases} \tag{8}$$

In which *the total velocities are related to the dominant modes in their respective directions, the* 1st mode *for* vertical *velocity* and the 2nd mode *for* lateral velocity. *D*isplacement *is* distribute*d* into these two modes *through a* similar calculation. *In other words*, instead of *a* force calculation based on normal or frictional forces, *state are* directly updated when impact occurs.

Mode 3: Sustained contact with adhesion

After each foot-terrain interaction in mode 2, one more check step is added to determine whether the robot foot is able to leave the ground afterward. In some situations, the robot foot will stay in contact with ground due to large ground upward velocity or large body downward velocity, while at other times it may be restricted by a small

downward adhesion force, hypothesized to occur due to small electrostatic and intermolecular adhesion forces between the robot foot and the underlying surface. From previous work, the adhesion force was found to be time dependent in microscale for similar geometries and materials [116]. Therefore, the adhesion force is linearized as:

$$F_{ad} = c_{ad,t}t + c_{ad} \tag{9}$$

in which t is the contact duration; $c_{ad,t}$ and c_{ad} are coefficients for adhesion force. If net upward force on the robot foot is smaller than threshold adhesion force, than the foot velocity ($v_{fg,j}$) and displacement ($x_{fg,j}$) in both vertical and lateral directions are enforced to be same as ground motion. Then the foot motion ($v_{fb,j}$ and $x_{fb,j}$) relative to body is inferred from body motion. To calculate the motion states ($X_{i,j}$), only the resonant mode with lowest frequency is actuated at Mode 3, as identified in [62, 87].

For practical purposes, in simulation an additional check is required at the beginning of a time step if at the previous time step the foot was in mode 3. This check step is to confirm whether the foot could leave ground, computed as:

$$\begin{cases} [K_1 \quad B_1 \quad \dots \quad K_n \quad B_n] \begin{bmatrix} X_{1,j} \\ \vdots \\ X_{n,j} \end{bmatrix} + F_{ext} - F_{net} > -F_{ad} \quad v_{zfb,f} < 0 \\ [K_1 \quad B_1 \quad \dots \quad K_n \quad B_n] \begin{bmatrix} X_{1,j} \\ \vdots \\ X_{n,j} \end{bmatrix} + F_{ext} - F_{net} < F_{ad} \quad v_{zfb,f} > 0 \end{cases} \tag{10}$$

in which K_i and B_i are spring constant and damping coefficient of the i-th mode, in this case not normalized by effective mass. The robot will remain in mode 3 if either of these two inequalities is fulfilled. Once a time step is determined to remain in mode 3, the robot foot displacement and velocity are forced equal to the ground condition during that time step.

Mode 4: Rest

The last mode for a robot foot is a rest or normal contact mode. In this mode, the robot foot rests on the ground with a positive normal force, because the net force on the

foot is downward. The dynamics of this mode are identical to those of mode 3. However, it is useful to distinguish this mode during simulation for the further study on the influence from adhesion force, so that behavior specific to the presence of adhesive forces can be easily assessed. In the dynamic model, if a robot foot would move below ground for a previous step while in mode 2, 3, or 4, the foot's dynamics remain in mode 4.

4.3.3 Robot body model

The robot body or chassis is treated as a rigid body having 5 relevant degrees of freedom; lateral translation in the y-direction is neglected. Based on the coordinate system defined in Figure 41, the robot rotation in x, y and z directions (ω_{bx}, ω_{by} and ω_{bz}) and translational motion in y and z directions (v_{by} and v_{bz}) are treated as being generated from the total moments in the z-direction and forces in x- and y-direction transmitted from the robot legs,

$$\dot{\omega}_{bx} = \frac{\sum F_{zl} y}{I_x};\ \dot{\omega}_{by} = \frac{\sum F_{zl} x}{I_y};\ \dot{\omega}_{bz} = \frac{\sum F_{yl} z}{I_z}; \tag{11}$$

$$\dot{v}_{by} = \frac{\sum F_{yl}}{m};\ \dot{v}_{bz} = \frac{\sum F_{zl} - mg - F_{db} - F_{sb}}{m}; \tag{12}$$

In (12), m is the mass of the robot body and I_x, I_y, and I_z are the moments of inertia in the x-, y- and z- directions. F_{db} and F_{sb} are the linear air drag and squeeze-film air damping terms of the robot body from (6); F_{yl} and F_{zl} are the force from each robot leg to body; x_j, y_j and z_j are the distances between the connection point of the body and the j-th leg to the position of the robot center of mass in the x-, y- and z- directions, respectively. Because of the finite gap between ground and the robot body, it is also possible that robot body can have contact with ground if the downward motion of body is large. This contact between robot body and ground is modeled with a coefficient of restitution, as for foot impact in the vertical direction.

The foot-terrain interaction is calculated based on the foot velocity with respect to ground as described under Mode 2 of the leg model. The body-foot interaction is the calculated from the foot velocity and displacement with respect to the robot body. Therefore the transformation between these two velocities is important during simulation of body dynamics, which was shown in previous work [109] as mentioned above.

4.4 Testing And System Identification

While initial FEA modeling provides a nominal set of parameters for model parameters associated with specific resonance modes (i.e. effective mass and stiffness parameters), completed robots may deviate from the model due to fabrication non-idealities, and a number of parameters associated with damping and external forces must be identified empirically. This section discusses dynamic frequency-domain testing.

4.4.1 Experimental Setup

Both in-chip and out-of-chip dynamics of micro-robots are measured, as excited by internal piezoelectric and external vibration stimuli, respectively. The experimental setup for in-chip characterization is shown in Figure 44 (left). A LabVIEW frequency sweep program interfaces a power supply to two micromanipulator probes, which apply the resulting voltage input to bond pads at the base of the silicon tethers to the piezoelectric actuators. A laser Doppler vibrometer, or LDV (Polytec OFV 3001S Controller & 303 Sensor head), and a stereoscope are used to acquire out-of-plane velocity and in-plane displacement measurements, respectively. The test setup for out-of-chip dynamics testing is shown in Figure 44 (right). Data acquisition is a performed as above, while a shaker (BK Vibration Exciter Type 4809) is used to excite motion of the detached micro-robot in a Teflon tray. The out-of-chip motion is measured with both the LDV and camera. The LDV measurement is used to understand the vertical motion of robot, and the video recorded with the camera is used to characterize the lateral speed of the robot. It is worth noting that the quality of the LDV measurement is dependent on the size and materials at the surface of the robot at various measurement points. As the polymer structures forming the foot do not reflect the LDV laser effectively, the motion of parylene-C foot cannot be directly measured. Thus, all experimental measurements of robot leg behavior are taken at least a short distance from the foot itself, for instance at the outer edge of the robot knee joint. When estimating foot displacement or relating simulated foot motion to experimental results, the displacement of the foot relative to the robot body is assumed to scale from measurements taken near the knee according to the geometries of mode shapes generated by FEA.

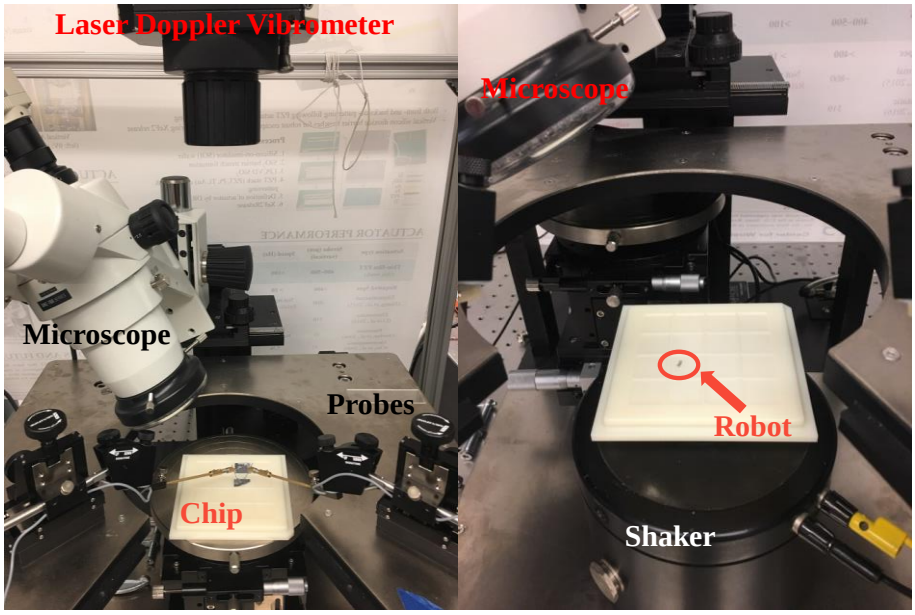

Figure 44 Photo of the experimental setup: (left) Laser Doppler Vibrometer measuring in-chip dynamics; (right) Robot out-of-chip measurement with shaker.

4.4.2 In-Chip Testing

First, functionality of micro-robot actuators during in-chip testing was assessed visually. Static displacement of individual robot feet was measured to be on the order of tens of micrometers using a 15 Vpp step input at 1 Hz. This step amplitude is observable with microscope. Therefore, it is convenient to identify the actuator functionality with a low frequency input (1 Hz or lower). Then, micro-robot in-chip characterization is focused on characterizing its dynamics under different frequencies and loading conditions.

Measurements of robot motion were taken at various locations on the robots during swept-sine excitation of the robot legs to verify and refine resonance behavior predicted by the FEA model. It was known that the silicon tether that connects the micro-robots to the wafer could also have a large influence on robot dynamics by introducing a mass-spring rigid body vibration mode to the system and stiffening the chassis structure; this was evaluated in part by examining the effects of constraining the vertical motion of the robot chassis with a micromanipulator probe.

Figure 45 plots the frequency response of out-of-plane velocity measured by the LDV at the robot chassis, at the robot “hip” (just after the in-plane actuator), and at the

robot “knee” (just after the vertical actuator). Although the elastic structure of the robot allows resonances to be transmitted throughout its structure, comparison of locations at which various resonances become most significant allows their sources to be verified. Testing results indicate that the robot chassis rigid body resonance on the tethers occurs around 830 Hz; the hip or primary lateral resonance is around 438 Hz (vs. 498 Hz from COMSOL); and the knee or primary vertical resonance is around 3.4 kHz (vs. 3671 Hz from COMSOL). The FEA and measured results matched well for both actuators in the frequency domain. The body or chassis resonance at 830 Hz was confirmed as a rigid body mode through comparison of velocities at additional locations on the chassis, showing nearly pure translation. These measurements also confirmed that elastic modes of the chassis itself are small below 3 kHz when constrained by the silicon tethers. Further confirmation was provided by adding additional stiffness supporting the robot with a micromanipulator probe, which increased the associated resonant peak from 830 Hz to 1.8 kHz, with negligible effect on the modes attributed to the individual legs.

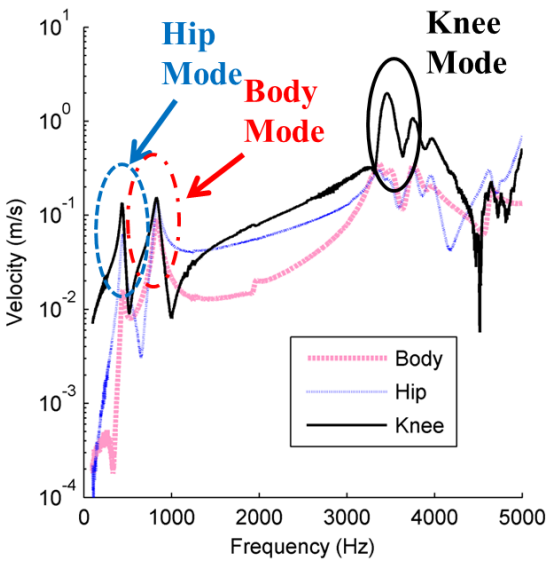

Figure 45 Resonance measurement of three different locations on the micro-robot: body (pink dash line), hip (blue dotted line) and knee (black solid line) indicate mode shapes associated with the hip near 438 Hz, uniformly generated on the body near 830 Hz, and most strongly associated with the knee near 3.4 kHz.

One significant difference between FEA modeling and experimental testing was observed with regard to vertical motion of the knee or out-of-plane actuator. The end

points of the three unimorph PZT beams comprising the knee actuator were measured and found to exhibit unequal velocity amplitudes, which indicates the existence of significant foot off-axis tilting motion. This had previously been predicted to be small during FEA analysis. While this was not intentionally designed for micro-robot locomotion, such motion has potential to be beneficial if it can supplement or be used in-place of originally-designed in-plane foot rotation originating in the hip actuator.

4.4.3 Out-of-chip Testing

Since the eventual goal of micro-robot motion is to realize autonomous, after characterization of in-chip dynamics one robot was detached to evaluate dynamic response during interaction with ground. As extracting the robot at this stage in development removes access to an active actuation signal, motion for out-of-chip testing was excited by a shaker. Figure 46 (left) shows the absolute motion amplitude of the tray, which is used as a reference to calculate the relative motion of three locations on the robot (chassis, hip, and knee), as shown in Figure 46 (right) under small amplitude ground excitation. It should be noted that the vibration velocity from the shaker decreases with frequency amplitude of robot motion is often small, such that only velocity measurements under about 3 kHz could be clearly distinguished from background noise. Unfortunately, given a finite availability of amplification settings for the current supply to the shaker, while a frequency sweep versus input voltage can be readily tested, only a small range of frequencies permit multiple ground amplitudes to be excited at the same frequency, and minimal robot motion could be observed at those settings.

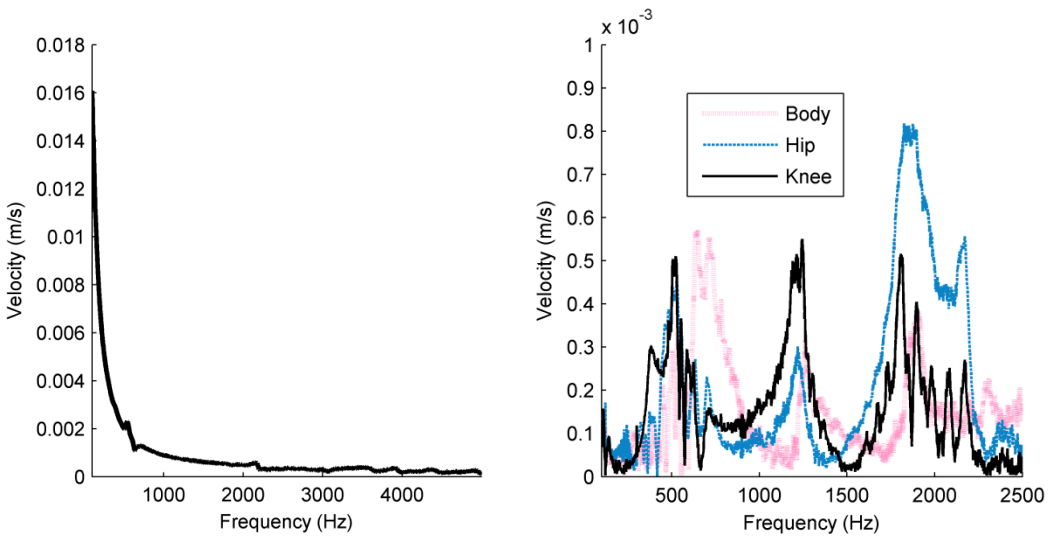

Figure 46 Frequency sweep results of a detached hexapod micro-robot: (left) the absolute velocity of the robot body; (right) the velocity of robot body (pink dotted line), robot hip (blue dashed line), and robot knee (black solid line) relative to the tray motion.

In Figure 46 (right), the relative velocities of three locations on the robots with respect to ground motion are plotted versus frequency. The largest motion amplitude is observed between 1.5 to 2.5 kHz. This mode is predominantly in the vertical direction as observable in the experimental setup. It is taken to be the primary vertical vibration leg of the mode after release from the wafer, being reduced from in-chip testing due to additional elastic chassis bending that is constrained by the silicon tethers when they were present in-chip. Additional vertical motion is measured around 800 Hz and 1.2 kHz, believed to be a resonance of body motion itself since these modes were not measured when a probe was pressed to the robot body in the chip.

4.4.4 Parameter Identification

The overall conclusion of frequency response testing was that after extraction from the wafer, the most significant resonant behaviors were present near 438 Hz, 1.2kHz, and 1.8 kHz, attributed to vibration modes associated with in-plane rotation at the hip, foot tilting motion, and out-of-plane leg bending due to compliance through the released body, leg, and knee, respectively. To simplify the dynamic model, an additional 800 Hz resonance was not considered in simulation because it was only found with in-chip testing, and attributed to robot oscillation on its tethers. The resonant frequencies and amplitudes

obtained were used to tune stiffness, mass, and input parameters in the state-space model for robot structural dynamics.

The squeeze film damping coefficients are calculated for both robot body and foot, as shown in Table 8, from models in [62, 87]. The coefficients for time dependent adhesion force are estimated from previous work [116].

Table 8 Table of coefficients for damping and adhesion

Coefficient	Value
b_g	1.5×10^{-19} Nm^2s (Body) 2.5×10^{-19} Nm^2s (Leg)
α	4.55×10^{-6} Ns^2/m^2
c_{ad}	50×10^{-6} N
$c_{ad,t}$	1×10^{-7} N/s

4.5 Dynamic Analysis Results

Using the identified system model and parameters generated through the experiments described in the previous section, the effectiveness of the proposed dynamic model at describing global robot motion in the presence of foot-ground interaction could be examined. The parameters used in simulation are listed in Table 9, including the mass of robot, resonant parameters. Two primary sets of data are available for model assessment: measurements of average lateral speed of the robot for various vertical ground excitation frequencies, and detailed time-domain measurements of vertical robot leg displacement, measured at the knee or hip.

Table 9 Table of simulation parameters in dynamic model

Parameter	Value
Total robot mass	0.33 mg
Robot body mass	0.28 mg
Normalized spring constant (N/m/kg)	Mode 1: 7.57×10^6 Mode 2: 5.68×10^7 Mode 3: 1.28×10^8
Normalized damping coefficient (Ns/m/kg)	Mode 1: 1.38×10^3 Mode 2: 1.76×10^3

Parameter	Value
Total robot mass	0.33 mg
Robot body mass	0.28 mg
	Mode 3: 2.97×10^3
Modal motion ratio, lateral to vertical motion	Mode 1: 15 Mode 2: 1/17 Mode 3: 1/15

4.5.1 Body lateral motion

At key frequencies, the detached hexapod micro-robot was found capable of fast lateral motion within the tray when excited by vertical vibration. Figure 47 shows two frames of sample motion recorded when the shaker was operating at 240 Hz with an amplitude of 25 μm. Sample robot motion video stills are shown with a time separation of 2 seconds. The speed of the robot is about 4 mm/s, with a small counter-clockwise turn observed, possibly due to one robot leg showing signs of damage during the detachment process. Because of the turn, the speed, instead of velocity, of robot is used for further validation of the dynamic model.

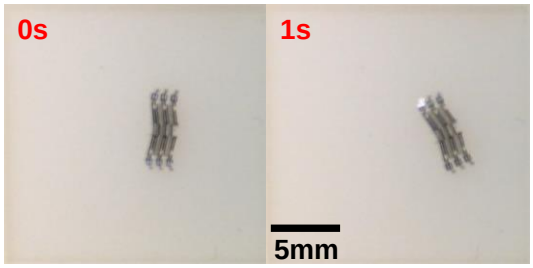

Figure 47 Hexapod micro-robot location at (left) time = 0s and (right) time = 1s when the tray is externally vibrated by the shaker at 240 Hz.

The existence of lateral motion of the robot near 300 Hz suggests that it's locomotion during ground excitation is generated by external vibration coupling to the hip actuation mode below its resonant frequency, which is also the mode of lateral foot actuation. Simulated robot motion at different frequencies was then compared with experimental measurement. Measured and simulated speeds are shown in Figure 48. The error bar of the simulation is generated from the uncertainty of robot parameters and the error of measurement is caused by the non-uniformity of robot motion speed. When the actuation frequency is higher than 400 Hz, no lateral motion was observed. The speed trends for

simulation and experiments are in qualitative agreement, showing a fast decline in speed from 200 Hz, and at around 300 Hz there was an increase in robot speed found both in simulation and experiments. The experimental setup (i.e. LDV and stereoscope supports) exhibits resonance when the shaker is actuated at a frequency lower than 150 Hz, preventing lower-frequency characterization using the current setup.

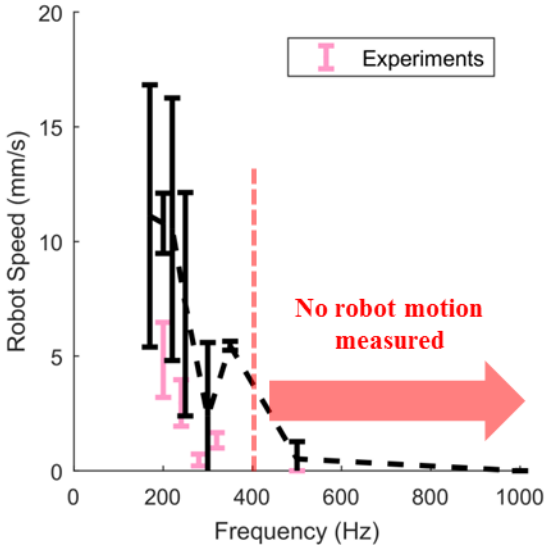

Figure 48 The relationship between shaker frequency and average robot speed; the simulations are shown as the black dashed line and the experimental results are shown as individual red data points with error bars.

Also shown in Figure 48, the simulation correctly predicts that no motion will occur at frequency ranges from 500 Hz up to 1.8 kHz, where experimental tests showed no measurable locomotion. This is despite the presence of various vibration modes in that region, but consistent with those vibration modes acting effectively out-of-plane with only small in-plane components. Ability to excite locomotion is also limited at higher frequencies because maximum amplitudes achievable by the shaker become smaller. The robot speed is mildly overestimated through the entire frequency range, which may indicate the existence of other micro-scale forces or more complex adhesion behavior beyond the contents of the current model. Nonetheless, the model does accurately estimate the overall speed trend.

4.5.2 Leg vertical motion

More detailed comparison of experimental and model results, and insight into effects of small-scale forces, was obtained from LDV measurements of vertical motion of individual robot legs. Different motion patterns were observed as characteristic for tests at varying frequencies and amplitudes. Three representative patterns are shown in Figure 49. The first example (Figure 49 (Top-left and top-right)) is a firm-contact pattern, in which the robot foot has constant contact with ground for small ground oscillations. Figure 49 (bottom-left) shows a partial firm-contact pattern at increased amplitudes: the robot stays in adhesion mode for some time length of each period, even beyond the point at which body motion would have otherwise pulled the leg free of the ground, but the foot does detach for an approximately uniform amount of time in each cycle. Figure 49 (bottom-right) is a jumping or bounding pattern when the shaker is actuated at higher amplitudes. Leg motion is stimulated to a much greater extent by the external vibration, and individual legs stay in the air for more than one actuation period, with substantially higher amplitudes (200μm) than the underlying ground amplitude (25μm). The appearance of different patterns depends on the actuation condition and initial condition of the robot in tray. The firm-contact pattern is measured when robot is only moving vertically when the shaker is actuated at 4V peak-to-peak; the jumping pattern is measured at a temporary pause within robot lateral in-tray motions when the shaker is actuated at 8V peak-to-peak.

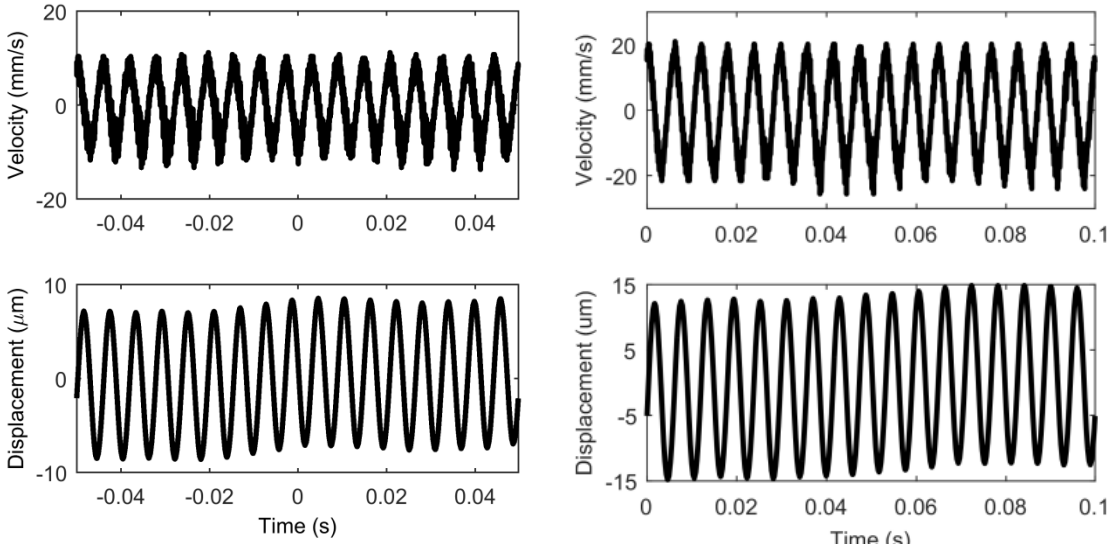

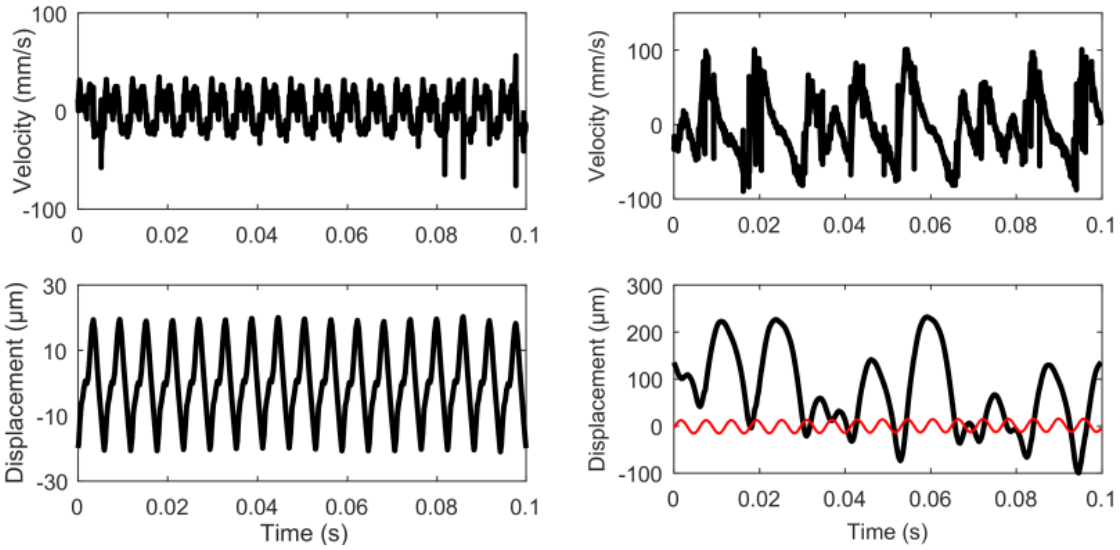

Figure 49 The vertical motion (velocity and displacement) of robot knees measured with the LDV at different legs, with commonly-observed motion patterns: (top left and top right) firm-contact pattern with constant foot-ground contact, (bottom left) partial firm-contact pattern with extended adhesion mode but eventual detachment from ground, and (bottom right) jumping pattern with long time in-air mode. The red line in the bottom right is a sample tray motion beside the measured location on the body. The shaker is actuated at 2V (top left), 4V(top right), 6V (bottom left), and 8V (bottom right), respectively.

Figure 50 compares the simulated vertical motion of robot knee with various external vibrating amplitudes, to support the assumption of distinct motion modes in the hybrid model. With small external vibration, the robot foot is accurately predicted to stays in contact with ground throughout motion. Larger external vibration could take off robot leg and show the in-air mode, in which the robot knee moves with a different velocity than the ground. By comparing them together, examples of adhesion mode behavior are identified. The abrupt velocity change from tracking ground to motion in-air mode is representative of a downward adhesive force that is broken suddenly when sufficient upward force is exerted from the body to the leg being observed.

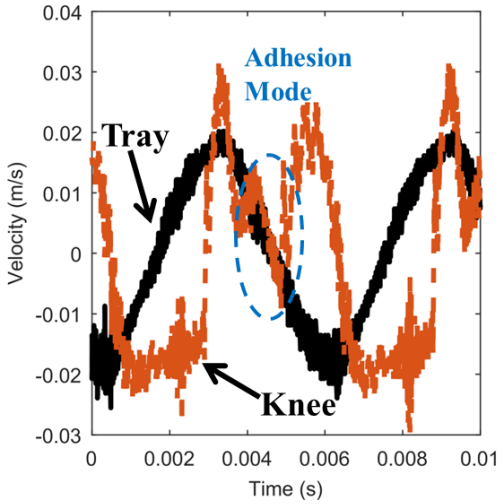

Figure 50 The vertical motion of the robot knee (dashed red) and tray (solid black), measured with the LDV when the shaker is actuated with 4V input voltage.

Figure 51 shows resulting motion profiles of firm-contact, partial firm-contact and jumping patterns appearing in the simulation. It should be emphasized that these conditions are only observed in simulation results when accounting for the three major out-of-chip vibration modes, external air damping identified from out-of-chip measurement, squeeze-film damping estimated from robot geometry, and adhesion forces estimated from prior works. Figure 11 (top-left) shows the firm-contact pattern when the shaker is acutated with 2 V peak-to-peak, as in experiments. Partial firm-contact starts to appear when the voltage signal increase to 4 V peak-to-peak (top-right plot in Figure 11). This similar motion pattern is observed in experiments, though it is first observed only above 4 V / below 6 V, again implying some additional adhesion behavior as inferred from robot speed comparisons. For 8 V peak-to-peak actuation (bottom-right plot in Figure 11), a jumping pattern with minimal adhesion time is observed in both experiments and simulation.

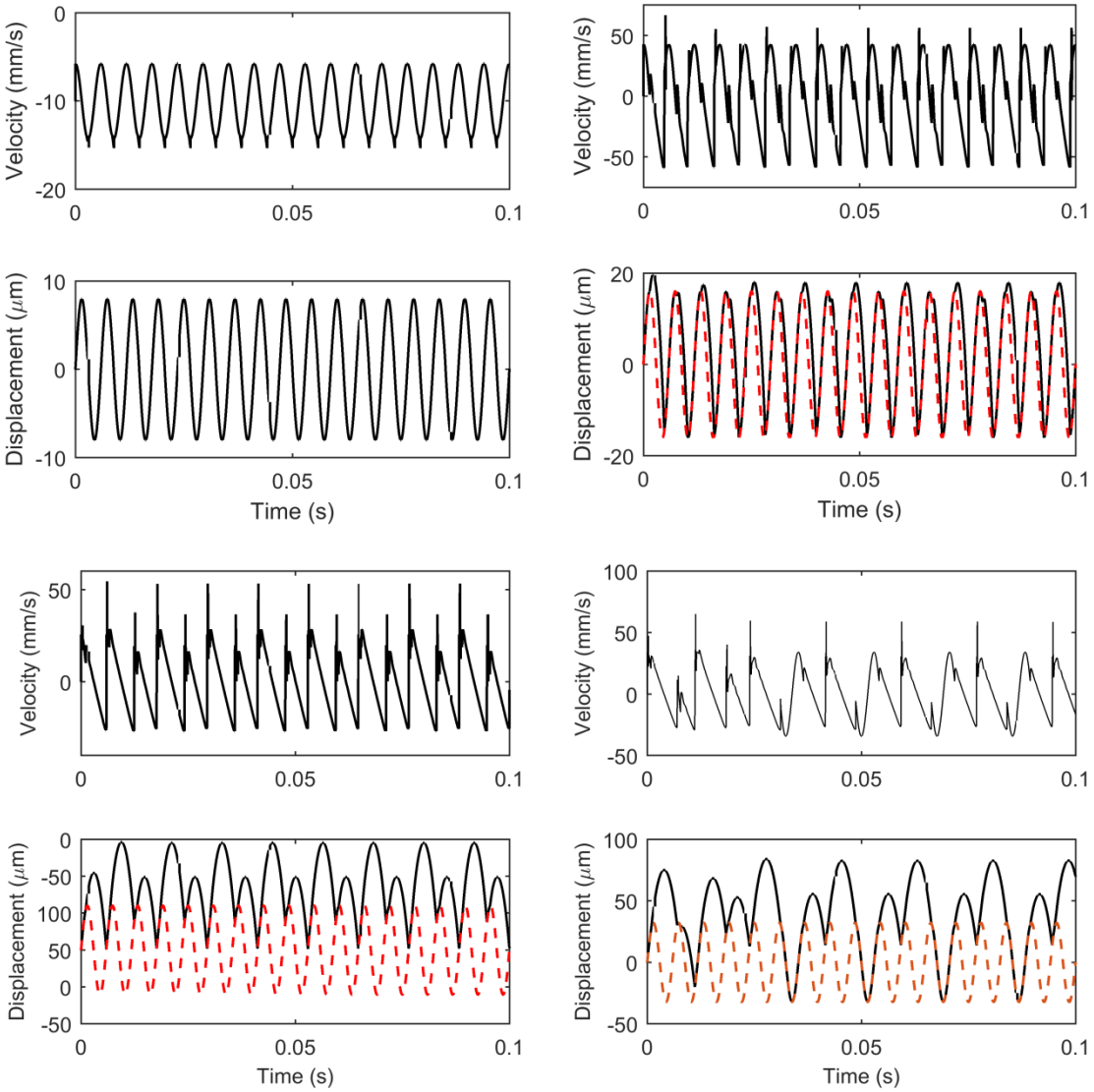

Figure 51 Robot leg vertical motion simulated with the proposed dynamic model: (top left) firm-contact pattern, (top right and bottom left) partial-contact and an intermediate, semi-periodic, pattern, and (bottom right) the jumping pattern. Red dash line in all plots is the tray motion in simulation. The shaker is actuated at 2V(top left), 4V (top right), 6V (bottom left), and 8V (bottom right), respectively.

4.5.3 Small-scale forces

The relative importance of various small-scale forces is also examined through comparison between full and simplified simulations. Sample predictions of foot vertical motion in the presence of various possible small-scale forces are shown in Figure 52. Both adhesion force and squeeze film damping force are small-scale, nonlinear factors

that substantially influence the simulated results for robot leg motion, and are critical to generating comparable foot motion patterns to those seen in experiments. Without the presence of a finite adhesion force, the partial firm-contact breaks the similarity between each actuation cycle, and no fully periodic foot motion is generated. It is important to note that "adhesion force" as treated in this work makes no distinction between various intermolecular forces that might influence its magnitude, but if even a small amount of adhesive attraction is present between the robot foot and its terrain, it is predicted to have a substantial influence on robot locomotion. At small locomotion amplitudes it can prevent effective movement, and at larger locomotion amplitudes, the adhesion force transfers the additional surface motion into the robot's compliant structure, which can be beneficial for forward motion. In contrast, squeeze-film damping reduces all individual leg motions to a substantial degree, so its collective influence is found to reduce robot speed. Therefore, understanding micro-scale forces are critical for the estimation of robot dynamics.

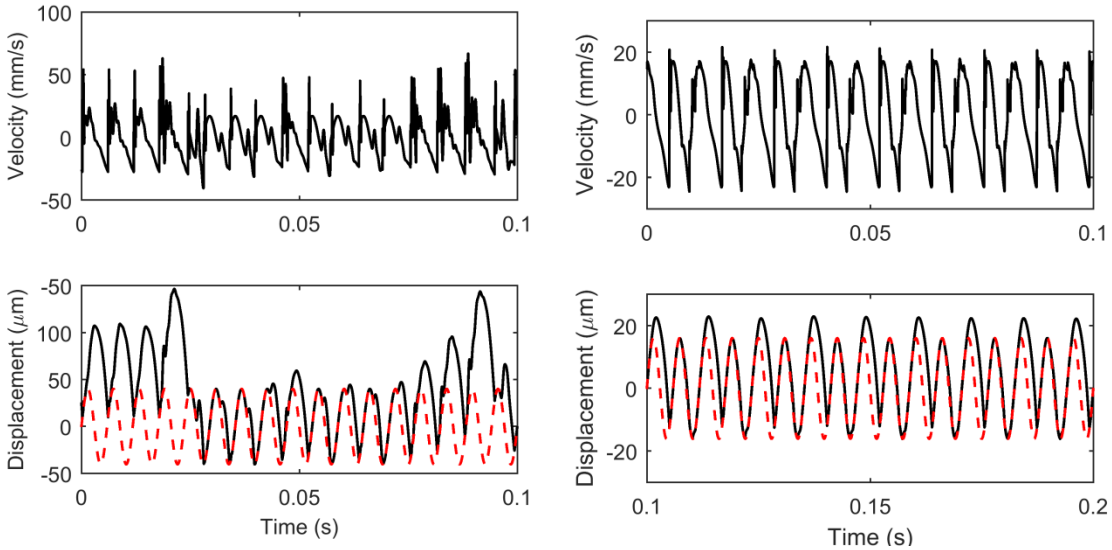

Figure 52 Robot leg vertical motion simulated with the dynamic model under different hypothetical micro-scale forcing scenarios: (left) Simulated without squeeze film damping force for neither robot leg nor body; (right) Simulated without adhesion force between robot foot and ground. Robot leg motion is shown with the black solid line and ground motion is shown with the red dashed line.

4.6 Discussion

Based on a dynamic model for structural and contact dynamics, the motion of a piezoelectrically actuated micro-robot has been simulated. Microscale forces, such as adhesion and squeeze film damping, are studied to understand their influence on robot locomotion. The robot speed is simulated to be in the scale of mm/s, with predicted speed in agreement with experimental speed in passive locomotion stimulated by vertical ground vibration. Error bars are simulated accounting for the resolution of fabrication and variation in forward motion over the duration of various simulations, and are likewise consistent with observed robot locomotion variability on a sample surface.

As a passive walker, this dynamic model can be compared with a smaller and faster robot modelled in [24]. The model techniques of [116] have a decent match for free leg motion between experiments and simulation, but are not able to give any prediction on the contact performance and forward motion. Compared to a single leg model from [63] which does include contact interaction, the leg motion prediction on its own is less accurate, but this current work permits estimation of robot forward motion and synthesis of multiple foot contacts, which was not done previously. As a candidate autonomous walking robot technology, comparison of the current robot's range of motion has been done in [114], with a basic projection of velocity, though findings from this work would suggest a reduction in robot speed and payload capacity due to squeeze-film damping and adhesion.

Towards the goal of predicting requirements and capabilities for dynamic locomotion of such an autonomous micro-robot in dynamic locomotion under piezoelectric actuation, we also applied the model developed above to a hypothetical robot being driven by an on-board power supply. To simulate autonomous locomotion, ground height is held constant in the dynamic model and the internal piezoelectric forcing, ($\mathbf{F}_{act}$ in the hybrid system model) are taken to be a square wave around the resonance of the actuators, to produce a tripod gait.

Figure 53 shows the simulated influence of adding robot payload when driving robot motion through on-board actuation near the first vertical resonance. The current micro-robot with structure and actuators is about 0.3 mg. In simulation, when the robot total mass is larger than 1.7 mg, the robot stop moving. In some cases, locomotion is

predicted to achieve a higher speed with a payload, as it improves uniformity of foot impact during simulation of a tripod gait. This is seen in Figure 53 as projected robot speed increases beginning when the robot mass is larger than 1.2 mg, because the robot foot has more contact with ground and fewer instantaneous rebound or bouncing impacts. When the total mass of a robot is larger than 1.7 mg, the actuation force is not large enough to support sustained vertical motion on all steps. Around 1.7 mg, the robot speed estimation has a large variation, because the robot can move quickly with lots of small bouncing impact to gain forward speed, or stick to the ground with almost no motion, heavily dependent on initial conditions and random perturbations to the robot actuation force or geometry.

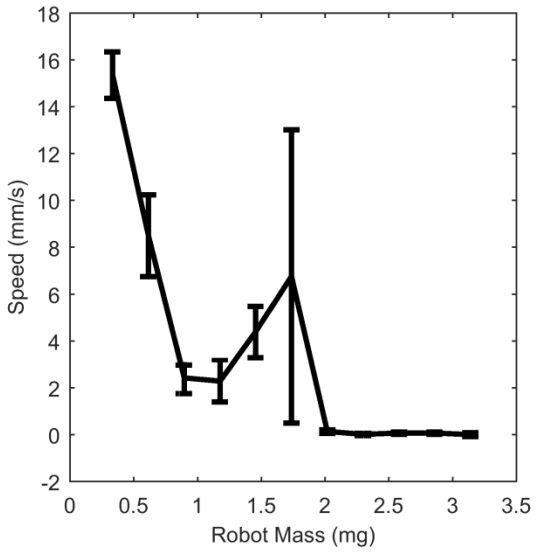

Figure 53 Simulated relation between robot mass and micro-robot motion when actuated with PZT actuators at 1.8kHz (first vertical resonance in simulation); Robot mass is about 0.33 mg with structure and actuators.

Figure 54 shows an example of robot speed trends as a function of frequency, in this case near the robot vertical resonance (1.8 kHz), associated with primarily lateral motion. This differs from ground excitation measurements, where vertical ground amplitude easily breaks foot-to-ground contact at various frequencies, but high-frequency excitations are both small amplitude (limited by the shaker) and excite only out-of-plane oscillation. In hypothetical untethered locomotion driven by the PZT, sufficient vertical foot displacement to break ground contact occurs most readily near the out-of-plane leg

resonance (1.8 kHz), but electrically coupled in-plane actuation is still at least partially-excited by the on-chip voltage.

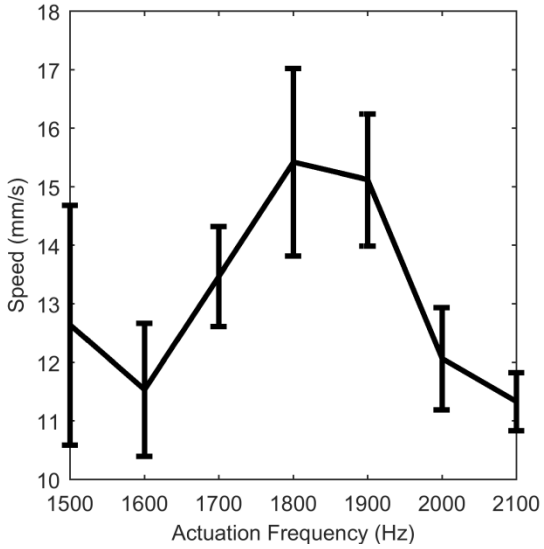

Figure 54 Simulated micro-robot motion when actuated with PZT actuators at different frequency around the first lateral resonance (438 Hz) with same voltage amplitude (20V).

4.7 Conclusion

The dynamics of a sample silicon hexapod micro-robot are studied as an example for understanding the legged micro-robots based on thin-film piezoelectric actuation. These robots have structural dynamics featuring elastic, linear resonances, light damping, and resulting high sensitivity to ground impact interactions. A dynamic model is modified from previous work with centimeter-scale piezoelectric robot prototypes, further integrating micro-scale feature such as adhesion and squeeze damping. The model is validated with passive out-of-chip locomotion, both lateral and vertical, of the detached hexapod micro-robot, using model information extracted from design parameters, finite element analysis results, and in-chip characterization.

Key features of small-scale motion near resonance examined in this work include squeeze-film damping and adhesion forces, with substantial effects for accuracy of foot motion and forward locomotion predictions, respectively. The model permits simulation of robot motion both with external vibration and on-board electrical actuation, allowing some exploration of potential robot-ground interactions should it operate under on-board

electrical power. However, some mismatch between simulation and measurements that can be taken still exists, possibly due to remaining complexities of foot-terrain interaction that are not been fully studied.

Further discussion on the robot motion with on-board electrical actuation was presented to understand possible scenarios for locomotion of micro-robots based on thin-film piezoelectric actuation principles. Microscale forces remain critical, but with actuation at vertical resonance, the robot is predicted to move at greater than 1 mm/s with a payload about 5 times its existing chassis weight, up to about 1.7 mg when the current mass of the structure and actuators is about 0.3 mg. Payload estimation and the simulation of different actuation frequency around robot lateral resonance emphasize the important of resonance characterization and operation near one or another of the robot's structural resonances. Further details of other contributing factors to microscale surface interactions, such as electrostatic forces and foot and/or ground plastic deformation, may improve the accuracy of dynamic model prediction. Further analysis will also examine other actuator inputs having potential for sustained efficient locomotion. Future tasks for practical micro-robot development include the validation of payload capability and integration with on-board battery or wirelessly-coupled power supplies.

CHAPTER 5 Clustered Optimization of a Small-Scale Robot Swarm with Minimal On-Board Sensing

5.1 Introduction

Micro-fabrication technology has the potential to one day enable small-scale robots to accomplish various missions, as for rescue, exploration, and defense, as a swarm of tens or even hundreds of individuals. Some previous research focused on the sensing, control and communication within a small-scale robot swarm [46, 117] to achieve a better robot performance. However, when robots are scaled down to sub-centimeter dimensions, robot payloads limit their on-board sensing and control capability. Therefore, an open question is whether off-board sensing results are sufficient for control and optimization purposes. Using several optimization algorithms, this work explores this question for a very minimal addition of on-board sensing in a simple task of locomotion speed optimization.

Various micro-robot designs have been proposed and validated [28, 31, 35, 41, 114]. Among these designs, a centimeter-scale walking robot [118] is used as the sample platform to study the possible utility of swarm optimization with or without on-board sensing. This centimeter-scale hexapod robot (Figure 57) has identical actuation design as the centimeter-scale robots presented in the previous chapter, but each leg of this design can be actuated individually. The supporting structure of the robot is 3D printed with polylactic acid (PLA). Limited fabrication resolution causes variance in robot parameters such as beam properties of robot legs and resulting resonance modes. Different terrain conditions lead to even more difference between robots' motion. The dynamic model of this robot [118] is well developed and validated with the capability to predict the dynamic

performance over a modest set of environmental (terrain) conditions. It is possible to estimate robot velocity and leg motion by integrating the influences from piezoelectric actuation, rigid robot chassis, multiple-mode dynamics of the robot legs and nonlinear foot-terrain interaction. Based on this centimeter-scale robot model, another model has been modified to explain the dynamics of millimeter-scale robots [119]. Therefore, any findings and conclusions from this work have the potential to be further extended to even smaller robots.

For millimeter-scale waking robots, an important question remaining to be answered is how much on-board sensing is necessary to understand robot dynamics, to optimize the robot locomotion, and to design and implement robot control [120]. Assuming a robot foot as a rigid point mass at the end of a flexible micro-robot leg, the foot motion may be measured as the tip deflection of the leg. Tracking foot motion of a micro-robot is then one possible way to implement on-board sensing. For piezoelectrically actuated micro-robots [114], independent sensing transducers are one candidate to track the robot foot motion, as in the form of resistive sensors [121] or current sensors [122]. However, integrating separate sensors and sensing small amounts of current on-board can both increase control circuit complexity and thus payload requirements. Therefore, an approach of using existing piezoelectric actuators as sensors intermittently is developed and validated in this work, to provide a better understanding of robot locomotion without increasing payload or fabrication complexity.

Three optimization algorithms are then applied to examine the potential for swarm optimization with or without intermittent on-board sensing: simulated annealing, Particle Swarm Optimization, and clustered Particle Swarm Optimization. Simulated annealing is a heuristic optimization algorithm that searches for the global optima by mimicking the annealing process [123, 124]. SA takes a small step in each iteration. This small step is accepted if it provides an improvement or is possibly accepted if no improvement. By tuning a few parameters in SA, a selected robot can search the actuation parameters associated with its global optimum performance.

Particle swarm optimization [125, 126] optimizes the performance of a robot in a swarm with swarm and individual information, specifically the global optimum within

the swarm and the global optima of individual robots. In reality, a swarm of micro-robots will encounter different terrain conditions and also their own performance varies by fabrication resolution, so each “particle”, or micro-robot, is not identical to the others. The diversity in the robot parameters hurts the performance of PSO because this algorithm is working based on the assumption of identical particles. Limited efforts have been done in clustered PSO [127] because the majority of PSO applications target the global optimum or the optimum of the overall swarm.

Considering the diversity of micro-robot parameter and/or terrain perturbations, individuals experiencing apparently similar circumstances may to be clustered together to seek an improvement in optimizing time and performance. The clustering process depends on not only the robot performance but also on-board sensing features that indicate the similarity between robots’ responses to their environment. With hierarchical clustering [128], the robots in a swarm are clustered into small groups by calculating the weighted distance between robots/groups. Each iteration combines a pair of closest robots/groups into one group. The distance is calculated with speed and sensing features of the robots.

The comparison between simulated annealing and Particle Swarm Optimization demonstrate the reduction of convergence time using swarm information; and the comparison between Particle Swarm Optimization and clustered Particle Swarm Optimization illustrates an improvement from the existence of on-board sensing in a very minimal form.

5.2 Robot Design and Dynamic Model

5.2.1 Robot Architecture

The robot simulated [118] in this paper is a simple small-scale (<10 cm) walking robot with 3 pairs of compliant legs connected with a rigid body, as shown in Figure 57. The robot frame is 3D printed with PLA. Six bimorph PZT actuators (T219-A4Cl-103X)

are epoxied to each PLA leg with intentional misalignment. The misalignment between PLA and PZT enables robot foot to generate coupled motion in two directions. The six legs are actuated in a tripod gait. This motion overcomes the force of gravity on the robot and resistance due to friction from surface underneath, to move robot forward.

This architecture is inspired by a type of silicon-based millimeter-scale robot (2-5 mm in dimension) [114]. The millimeter-scale robot has two thin-film PZT actuators for each leg, to generate foot motion in two directions. Its chassis is made from silicon with parylene-C, again a polymer material, for elastic mechanisms. Accounting for scaling, both robot architectures perform similarly in a reasonable range of operating condition.

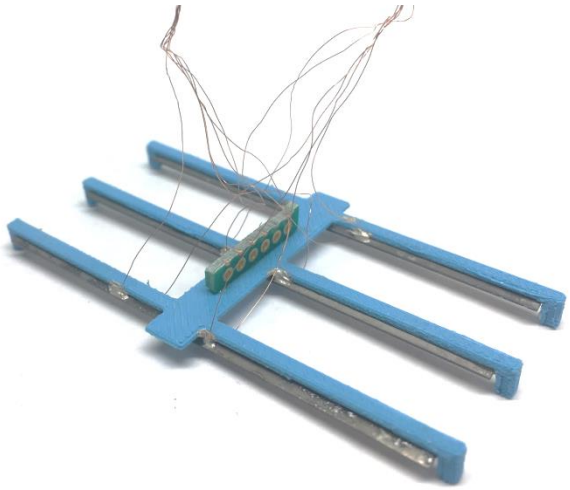

Figure 55 Photo of a 3D printed PLA hexapod robot integrating PZT actuators.

To test the sensing signal from the PZT actuators as sensors, the front two and back two legs are connected to the power source for actuation, while one of the middle legs is connected for sensing. A Laser Doppler Vibrometer (LDV) is used to measure the vertical motion of the leg with the PZT actuator as sensor. The sensing voltage signal from the robot is compared with the LDV measurement data to validate the accuracy of the derived model.

5.2.2 Dynamic Model

The dynamic model used in this chapter is that introduced in previous chapters, and includes robot body, leg and contact dynamics. This model is capable of replicating robot dynamics measured experimentally. Both robot forward motion and robot leg vertical motion from experiments and dynamic model are compared to validate this model.

The robot body is modeled as a rigid body with multiple degrees of freedom. Unrealistic side walking is excluded in this model, though this walking is observed in some other robot architectures.

Leg dynamics of the small-scale robot are explained with a simplified cantilever beam with complex boundary condition. The robot foot is modeled as a tip mass at the end of a cantilever beam, namely the robot leg. The mass of each robot leg is not negligible because the mass of PZT is comparable to other parts of robot foot. The actuation force from PZT actuators is modeled as distributed force along the beam (robot leg). The impact force calculated from contact dynamics is modeled as tip force. Based on this model, multiple resonance modes are calculated to determine the optimal operation frequency range and the distribution of external force into each mode.

Contact dynamics consider the foot-terrain interaction in two directions. A simple model with coefficient of friction and restitution is enough for centimeter scale, though more complex nonlinearities are observed with a millimeter-scale robot. Full details of the dynamics model are provided in [114, 118].

5.3 On-Board Sensing

To use a piezoelectric actuator as a sensor requires understanding of the relationship between tip deflection of a piezoelectric beam and its voltage output. This relationship depends on the beam geometry, boundary condition, and piezoelectric material properties. Many research studies focusing on piezoelectric materials have

demonstrated successful models of piezoelectric sensing for various applications [101, 129-132]. Some past works have similarities with the small-scale walking robots examined here [133-135], integrating bulk bimorph lead zirconate titanate (PZT) actuators with a compliant support layer/structure. [133] presents a model for bimorph PZT actuators with subtract layer, which also includes tip mass as boundary condition and is able to predict beam behavior in frequency domain. However, the time domain response is more critical in the study of robot dynamics. This work also confirms the proportional relationship between the tip velocity and the integral of PZT voltage output, under the specific operating conditions of the small-scale robots. Among previous works, [134] provided an equivalent circuit model and extended PZT output voltage to the loading circuit performance. The final equation in that work shows a linear relationship between the PZT output voltage and the acceleration of the beam tip, which is same as a linear relationship between the integral of PZT voltage and tip velocity. However, this work only shows the critical steps of its derivation, which is not sufficient to be further modified for microrobot application.

In this section, the relationship between the foot motion and sensing voltage signal as a relative acceleration measure is derived from basic physical behaviors for a robot leg. A model for bulk bimorph PZT sensors are derived and validated with a centimeter-scale robot prototype with 6 bulk PZT actuators/sensors, which can be further implemented in the microrobot application.

5.3.1 Sensing Model Derivation

A multi-layer cantilever model can be a lumped model for the robot leg with 3D-printed PLA structure and a bulk bimorph PZT actuator. Therefore, starting from the derivation in the appendix of [135], a derivation is presented to explain microrobot foot motion sensing. The first assumption for the derivation is to neglect the PLA structure layer during sensor charge generation analysis, because the 300 um thick PLA layer is much more compliant and has much less mass than the 480 um thick PZT actuator, the PLA structure is negligible in the modeling process. Therefore, the model is simplified to

two PZT layers with one more intermediate layer. Then the moment of inertia of two PZT layers is given as:

$$I = 2(\frac{wt^3}{12} + wtb^2)$$

in which *w* is the width of a robot leg, *t* is the thickness of an individual piezoelectric layer, *b* is the distance from the center of the beam to the center of one piezoelectric layer. One more coefficients are defined, B_{fs}, which stand for the relation between vertical force to stress:

$$B_{fs} = \frac{2I}{b(2l_b + l_m - l_e)} \quad (1)$$

in which l_b, l_m, l_e are the length of beam, tip mass and electrode. The final relation between the tip acceleration and the output voltage is determined from the stress equation of one PZT layer:

$$\sigma_{in} = \sigma_m + \sigma_{bm} + \sigma_t + \sigma_y \quad (2)$$

in which the input stress σ_{in} is expressed with the tip mass (m) and body acceleration ($\ddot{y}$):

$$\sigma_{in} = \frac{m}{2B_{fs}}\ddot{y} \quad (3)$$

The stress of the inertial element, tip mass is expressed with tip acceleration ($\ddot{z}$):

$$\sigma_m = \frac{m}{2B_{fs}}\ddot{z} \quad (4)$$

The damping stress is negligible since PZT is lightly damped and the stress from Young's modulus (Y) and strain term (δ) is:

$$\sigma_y = Y\delta \quad (5)$$

The last stress term is from the piezoelectricity (σ_t):

$$\sigma_t = -\frac{dY}{t}\frac{V}{2} \quad (6)$$

in which d is the piezoelectric strain constant, d_{31} specifically in this robot. V is the total voltage generated across the beam. Knowing the permittivity of PZT (ε), the relation between output voltage and strain can be further derived to be:

$$V = -2\frac{dYt}{\varepsilon}\delta \tag{7}$$

The final equation that relates the output voltage with vertical acceleration can be simplified to:

$$\frac{\ddot{y}-\ddot{z}}{V} = (\frac{dY}{2t} + \frac{\varepsilon}{2dt})/(\frac{m}{2B_{fs}}) \tag{8}$$

5.3.2 Sensing Model Validation

From the value listed in Table 10, the coefficient between vertical acceleration and voltage is calculated to be around 33 m/s^{2}V. When this coefficient is applied to the integral of measured voltage, a comparison is presented to show the match between measured foot velocity and calculated velocity.

Table 10: Parameters and their value used for robot foot motion model.

Width of robot leg	w	3.2 x 10^{-3} m
Thickness of one piezo-layer	t	2.4 x 10^{-4} m
Distance from bending axis to piezo-layer	b	1.2 x 10^{-4} m
Length of beam	l_b	3.18 x 10^{-2} m
Length of tip mass	l_m	4 x 10^{-3} m
Length of electrode	l_e	3.18 x 10^{-2} m
Tip mass	m	1.66 x 10^{-4} kg
Young's modulus	Y	6.6 x 10^{10} Pa
Piezoelectric strain constant	d_{31}	-190 x 10^{-12} m/V
Permittivity	ε	1800 x 8.85 x 10^{-12} F/m

Using the coefficient calculated from the model, the robot foot motion calculated from PZT sensors are compared with the motion measured from the LDV. The comparison is shown in Figure 56. Motion at less than 500 Hz can be clearly captured with PZT sensors. The actual coefficient calculated from measurements is 31.5 ± 3.3 m/

s^2V, by computing the ratio between the LDV-measured speed and the integral of PZT output voltage. The calculated value is set with in the measurement range with errors.

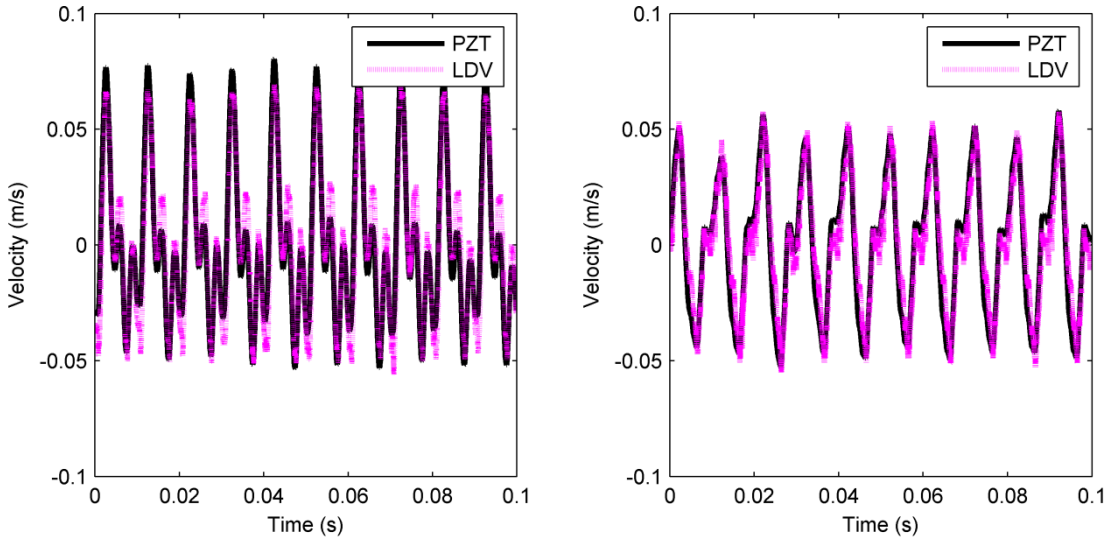

Figure 56. The comparison of the robot foot motion measured from LDV and PZT sensor when the robot is actuated with 100 Hz (left) 20 V square wave and (right) 60V sin wave

5.4 Preliminary Results for Motion Optimization

5.4.1 Classical Approach

To begin assessment of robot velocity optimization with and without hypothesized on-chip feedback, some preliminary simulations are generated with the dynamic model to demonstrate common features of robot behavior. The robot speed trend with respect to frequency and duty cycle of a square wave input is shown in Figure 57. From this simulation, the relationship between robot speed and actuation parameters does not support an analytical method for robot speed optimization, for reasons such as the impact events that occur at foot touchdown. Therefore, seeking for a numerical solution with suitable computational complexity becomes important for small-scale robot optimization.

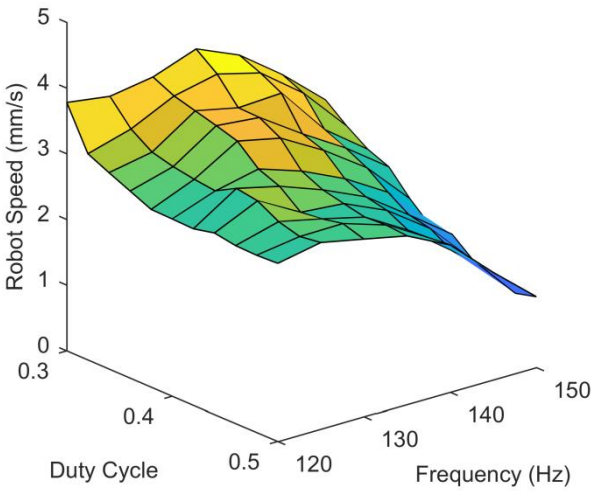

Figure 57 Simulated speed trend with respect to frequency and duty cycle of actuation signal. The relation between speed and actuation parameters tends to be non-derivative.

A sampling of intuitive algorithms has also been tried for this optimization and are reported here. Figure 58 (top) shows the schematic of an "Individual Algorithm", optimizing a swarm of several robots under random external perturbation. It is assumed in these scenarios that an external observer can measure robot locomotion speed, but has no other information about on-robot dynamics. The Individual Algorithm acts to update the individual robot actuation parameters with the parameters and the speed in previous iterations of control inputs, with the principle equation being:

$$d_i^{k+1} = d_i^k + \alpha * \frac{v_i^k - v_i^{k-1}}{d_i^k - d_i^{k-1}} + n_i^k \tag{9}$$

in which d_i^k and v_i^k denote the input parameter (d) and the speed (v) at the k-th iteration of the i-th robot, and α and n_i^k are the fixed scaled factor for perturbation and the randomized noise matrix, respectively, both empirically determined. The value of α and n_i^k are different for each input parameter; from testing, $\alpha = 10$ and $-0.1 \leq n_i^k \leq 0.1$ for frequency and $\alpha = 0.01$ and $-0.1\% \leq n_i^k \leq 0.1\%$ for duty cycle.

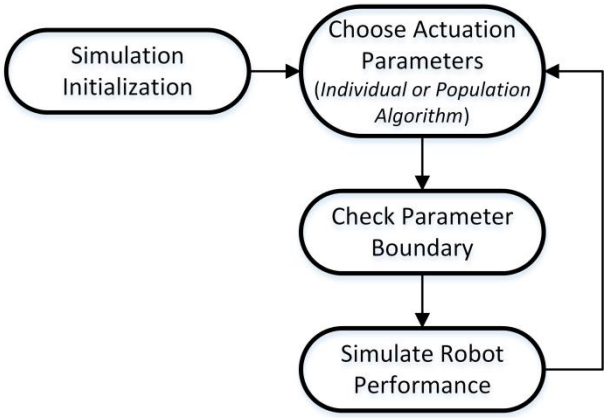

Figure 58 Schematic of the Individual Algorithm and Population Algorithm (bottom) for robot speed optimization

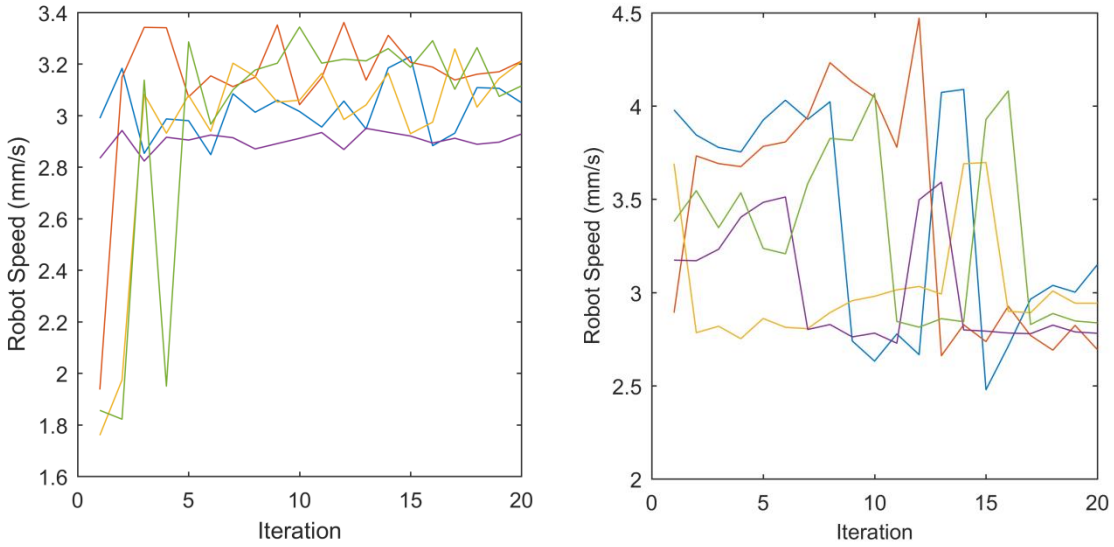

Figure 59 Result of speed optimization with single parameter (top) and two parameters (bottom) from the Individual Algorithm, where the five different trajectories represent five different robots in the simulation, and the x-axis represents the number of iteration, the y-axis represents speed [mm/s].

Figure 59 shows the optimization results when applying Individual Algorithm to five randomly generated robots. Single-parameter update and two-parameter update are presented. From this simulation, the Individual Algorithm cannot guarantee a stable optimization if multiple actuation parameters are included, requiring more a sophisticated multi-variable search than is presented here. Also, the robot speed is not stabilized at a high value compared to what will be seen using more coordinated optimization schemes.

The second coordination method in the absence of on-robot data is then denoted as the "Population Algorithm." The schematic of the Population Algorithm is demonstrated in Figure 58 (bottom). In this method, the information from all robots in the swarm has an influence on the single robot parameter update. Specifically, the average speed and actuation parameters of all robots are used in the update principle. The principle equation is derived to be:

$$d_i^{k+1} = d_i^k + \alpha * \frac{\bar{v}^k - v_i^k}{\bar{d}^k - d_i^k} + n_i^k \tag{10}$$

where $\bar{d}^k$ and $\bar{v}^k$ denote the average input parameter ($\bar{d}$) and the average speed ($\bar{v}$) of all robots at the k-th iteration. The value of α and n_i^k remain the same as discussed in the Individual Algorithm. Figure 60 shows the result from performing the Population Algorithm of speed optimization. The speed of robots is slightly better after 20 iterations.

$$d_i^{k+1} = d_i^k + \alpha * \frac{\bar{v}^k - v_i^k}{\bar{d}^k - d_i^k} + n_i^k \tag{11}$$

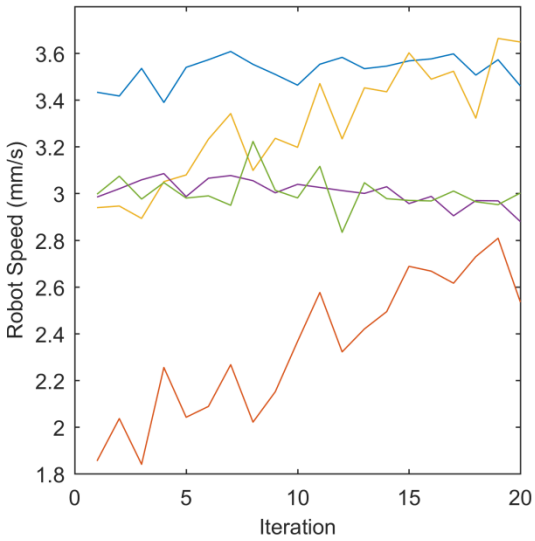

Figure 60 Result of speed optimization with two parameters from the Population Algorithm, where the five different trajectories represent five different robots in the simulation, and the x-axis represents the number of iteration, the y-axis represents speed [mm/s].

5.4.2 Features for Clustering

Because of the limitations of two intuitive optimization algorithms, machine learning algorithms are proposed for this optimization, using data clustering based on simple measurements hypothesized from on-board robot sensing. For example, one of the simplest pieces of information to extract from a piezoelectrically-actuated micro-robot is deformation of the piezoelectric element (i.e., vertical deformation of a robot leg in the simulated robots), as it requires no additional structures to be fabricated at the micro-scale level. Nonetheless, active sensing still incurs significant power or complexity costs, rising with sensing frequency[136, 137], so decision making with a small number of measurements per step is highly desirable.

Data clustering is a technique of combining similar data points together based on specific and distinctive features they share within a cluster. It is plausible to identify many distinctive features and hence to cluster robot velocity based on these features that are distinguished in phase plots. For the purpose of data clustering, a candidate feature will contain three parameters: the measure itself (i.e. displacement or velocity), an angle from 0° to 360° reflecting its timing over one cycle of robot leg motion, and the number of the leg it is associated with. One challenge is to select, among all candidate features, the most representative and applicable ones to use in the data clustering algorithms. In this work, phase plots serve as a visual guide for selecting candidate features.

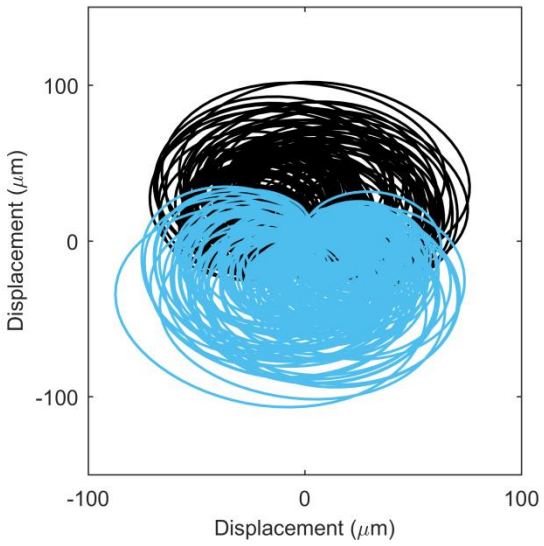

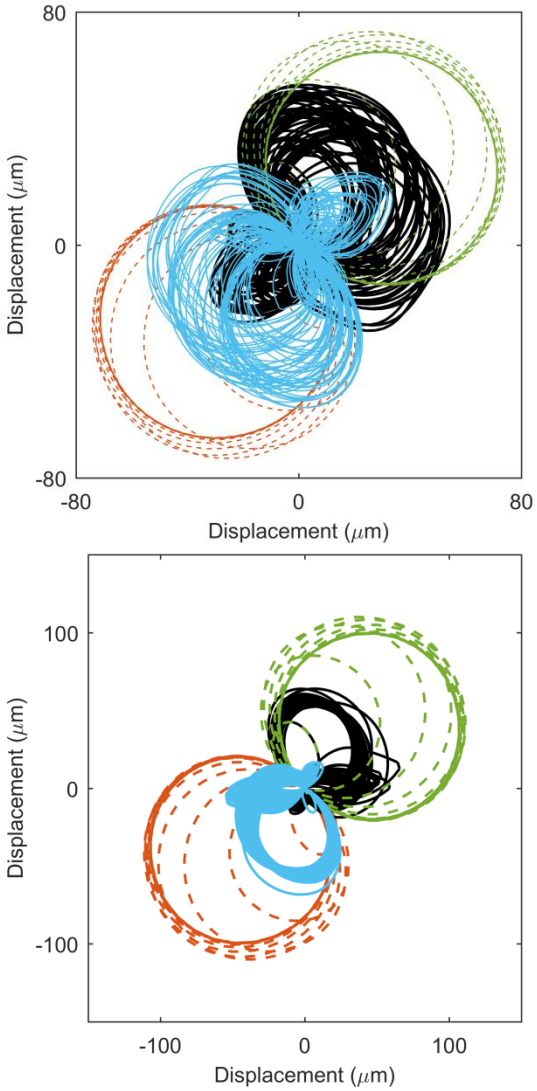

Figure 61 Phase plot of the robot foot displacement with respect to the body in the z-direction, when the robot body lateral speed is slow (left), medium (middle) and fast (right); each number on the legend chart represent one leg on the robot with some leg motion overlapping each other on the graph.

In this work, candidate sensing features that are representative of the robot speed were determined as follows. First, robot speed was arbitrarily divided into three categories: slow (0.20 to 1.99 mm/s), medium (2.00 to 4.99 mm/s), and fast (above 5.00 mm/s). Under such a scheme, an ideal candidate feature would produce distinctive phase plot patterns for each robot speed categories. Hence, phase plots of the robot in multiple states were generated by choosing one parameter at a time. It was found after numerous simulations that there was a rather regular correlation between the leg motion depicted on

any phase plots and the robot speed: as the robot speed increases, the robot leg motion becomes less variable from cycle to cycle (i.e., more uniform step-to-step foot trajectories). Representative candidate features in the z-direction include: robot foot displacement with respect to (*w.r.t.*) the body (*fz*), robot foot displacement *w.r.t.* the ground (*fbz*), and robot foot velocity *w.r.t.* the (*fvz*). Some representative phase plots featuring *fz* are presented in Figure 61.

5.5 Algorithms

After a literature review of several machine learning algorithms, Simulated Annealing and Particle Swarm Optimization were selected for proof-of-concept evaluation in this small-scale robot application. The Simulated Annealing promises a global optimum, or a local optimum close enough to the global ones, for one robot. This algorithm shows the insight time-wise, how long a heuristic algorithm needs when searching for a numerical solution, and helps to assess the utility of a swarm optimization. Particle Swarm Optimization is selected for its capability to optimize a swarm of objects. Other evolutionary algorithms can also be a potential candidate for robot application, with learning rate or evolution rate a possible concern with this type of algorithm.

5.5.1 Simulated Annealing (SA)

SA is adapted for small-scale robot application in this work as follows. This algorithm includes tunable starting and stop temperature (T_i and T_f), and cooling rate (δ_T). The principle is:

$Let\ d_i^k = d_i^0; T = T_i; k = 1$

$While\ T < T_f$:

$d_i^k = random\ within\ range(d_i)$

$$if\ v\left(d_i^k\right) > v\left(d_i^{k-1}\right)\ or\ P\left(v\left(d_i^k\right), v\left(d_i^{k-1}\right)\right) > rand(1): k = k + 1;$$

$$T = \ \delta_T T;$$

in which k is the iteration number; $v\left(d_i^k\right)$ is the velocity simulated from d_i^k, which is defined as in the Individual Algorithm; $rand(1)$is a random function returning a value within the range of 0 to 1. $P\left(v\left(\mathrm{d_i^k}\right), v\left(\mathrm{d_i^{k-1}}\right)\right)$ is a probability function returning a value from 0 to 1. A conventional way to define this function is with the exponential function (*exp()*):

$$P\left(v\left(d_i^k\right), v\left(d_i^{k-1}\right)\right) = exp\left(\left(v\left(d_i^k\right) - v\left(d_i^{k-1}\right)\right)/T\right) \quad (12)$$

5.5.2 Particle Swarm Optimization (PSO)

PSO is also adapted for small-scale robot application as follows. The schematic of PSO is demonstrated in Figure 62. The concept of this algorithm is to update each robot with its currently estimated optimum and the global optimum of all robots within its swarm in each step. The update equations are determined as:

$$vd_i^{k+1} = w_v vd_i^k + w_{sw} rand(1)\left(v^{sw} - v_i^k\right) + w_{sg} rand(1)\left(v_i - v_i^k\right) \quad (13)$$

$$d_i^{k+1} = d_i^k + vd_i^{k+1} \quad (14)$$

in which w_{sw}, w_{sg}, and w_v are the weight of swarm global optimal velocity, of single robot optimal velocity, and parameter approaching velocity, respectively; v^{sw} and v_i are the best velocity of the swarm and *i*-th robot; vd_i^k is the approaching velocity of parameter of the *i*-th robot at the *k*-th iteration.

5.5.3 Clustered Particle Swarm Optimization (CPSO)

CPSO is modified from standard PSO. After clustering robots into multiple groups, the group optima are also used to approach optimum of each robot. The

schematic of CPSO is shown in Figure 63. Within the first iteration, robots in a swarm are clustered into various groups with normalized speed ($v_{n,i}$) and their sensing feature value ($p_{n,i}$). Robots with similar performance are clustered by calculating the virtual distance ($l_{i,j}$) between each two robots (i and j). The virtual distance is calculated from:

$$l_{i,j} = \sqrt{w_{sp}\left(v_{n,i} - v_{n,j}\right)^2 + w_{ss}\left(p_{n,i} - p_{n,j}\right)^2} \tag{15}$$

in which w_{sp} and w_{ss} are the weight of the normalized robot speed and the normalized sensing feature value.

The maximum number of robots in one group (max_g) is set as a stop criteria. The update equations are similar to PSO, but further including the group optimum:

$$v_{d,i}^{k+1} = w_v v_{d,i}^k + w_{sw} rand(1)\left(v^{sw} - v_i^k\right) + w_{sg} rand(1)\left(v_i - v_i^k\right)$$

$$+ w_g rand(1)\left(v_j - v_i^k\right) \tag{16}$$

$$d_i^{k+1} = d_i^k + v_{d,i}^{k+1} \tag{17}$$

in which w_g is the weight of group optimal velocity; v_j is the best velocity of the j-th group that includes i-th robot; $v_{d,i}^k$ is the parametric velocity of the i-th robot at the k-th step.

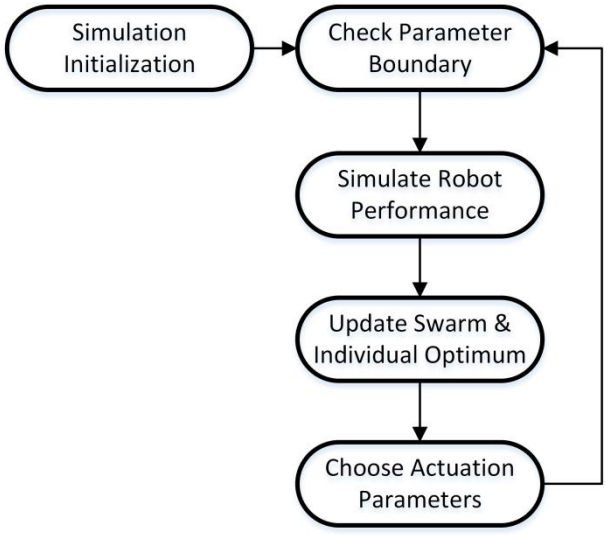

Figure 62 Schematic of the Particle Swarm Optimization for robot speed optimization;

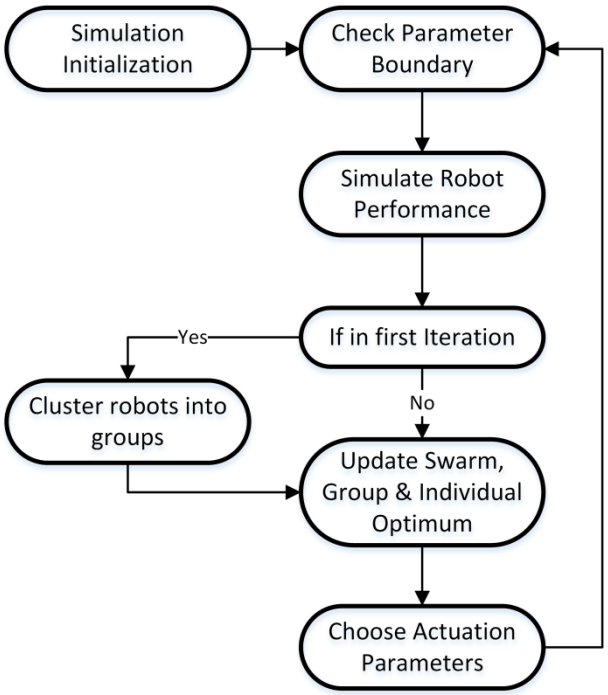

Figure 63 Schematic of the Clustered Particle Swarm Optimization for robot speed optimization;

5.6 Results

The simulation results of the three algorithms are generated after carefully selecting the algorithm parameters. Parameters in simulations, shown in Table 11, are not all optimized, though they still assist to indicate the performance and potential of the algorithms. The results from SA and PSO illustrate the advantage and drawbacks of algorithms for a swarm of robots or a single robot within the swarm. The simulation with and without clustering is intended to examine the importance of on-board sensing, even being at a minimal level.

Table 11 The optimization parameters, the ranges of actuation and terrain parameters selected for simulation

Algorithm	Parameters/Ranges	Value

SA	T_i	1
	T_f	0.01
	δ_T	0.9
PSO	w_{sw}	0.4
	w_{sg}	0.2
	w_v	0.1
CPSO	w_{sp}	1
	w_{ss}	1
	w_g	0.8
	max_g	10

5.6.1 Single vs. Swarm Optimization

Figure 64 compares the simulation of one identical robot with single optimization and swarm optimization. The single robot optimization with SA runs 100 small steps, though only 20 of them are accepted due to the acceptance criteria. This enhances the computational time complexity, and testing time complexity for real robot application. Overall, as demonstrated with Figure 57, a brutal simulation can reach the global optimal solution with certain step width of parameters. A single robot optimization can approach a global optimum of robot actuation parameters, or a local optimum close enough to the global one, because it is close to a brutal simulation with stop criteria. However, a much longer computing time is traded off for the single robot optimization algorithm.

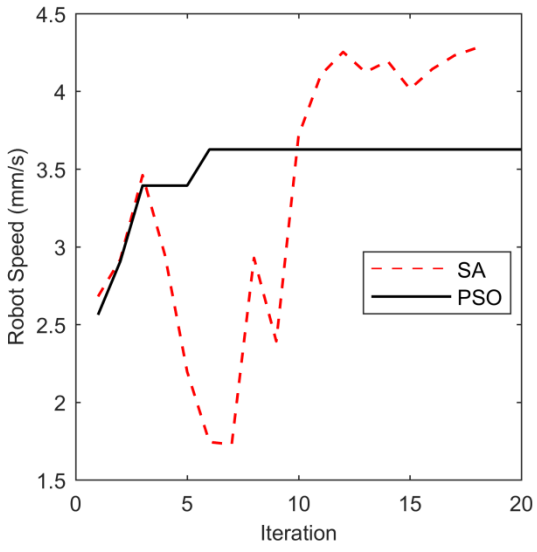

Figure 64 Velocity trend of one robot, using Simulated Annealing with 20 updates from 100 small steps and Particle Swarm Optimization within a swarm of 50 robots and 20 iterations.

PSO, as an example of a swarm algorithm, generates stable results with around 6 iterations for a robot within a swarm of 50 robots. The steady-state result from this algorithm has smaller speed than that from SA. This difference may possibly be compensated in certain degrees with better parameters selection, because the parameters so far are selected within a reasonable range without further searching. Overall, swarm algorithm significantly reduces the time required to reach an equilibrium parameter selection, though at a cost of reduced average performance.

5.6.2 Clustering with On-board Sensing

To examine the utility of limited on-board sensing, comparison between PSO and CPSO identifies the robot performance difference caused by clustering robots with minimized on-board sensing. Figure 65 compares the performance of PSO and CPSO with identical initial condition. A swarm of 50 robots is applied with PSO, the average speed of all 50 robots is plotted against iteration up to 50 (Figure 65). After 10 iterations, the average speed is almost stabilized around 3.55 mm/s. Converging speed is close to the performance of fewer robots in the last section.

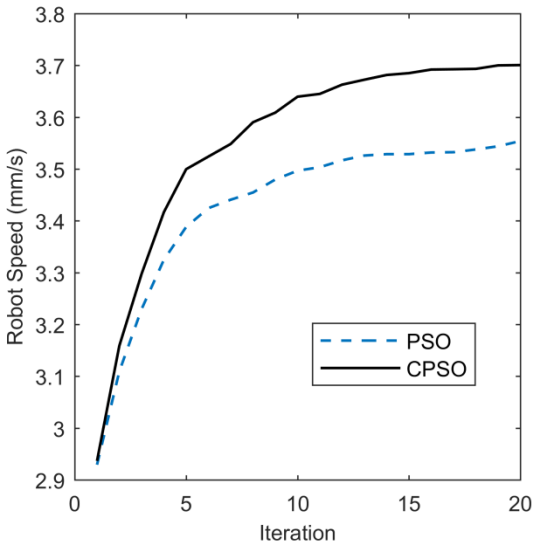

Figure 65 Average velocity of 200 robots as a swarm, using Particle Swarm Optimization (PSO, blue dash line) and Clustered Particle Swarm Optimization (CPSO, black solid line);

CPSO optimizes the robot performance with hierarchical clustering. The clustering process only exists in the first iteration, with robot speed and robot sensing. After around 10 iterations, the robot speed optimized with CPSO is stabilized to 3.7 mm/s, turning out to be an improvement of 23% over PSO.

5.7 Discussions and Conclusions

Understanding use of piezoelectric actuators as sensors can benefit on-board sensing scheme design for millimeter-scale piezoelectric robots. With a couple of actuators on a single robot leg, using one actuator as a sensor can help to perform real-time continuous sensing when robot actuation is under way. Without extra sensing components, it can simplify the fabrication process and reduce the payload budget. In this work, the relationship between the sensor tip deflection and sensing voltage signal is characterized and validated with a centimeter-scale robot prototype. The measurement and model estimation matches within the range of error. Practical sensing measurement

with the robot is achieved at different actuation conditions. The sensing algorithm is functional for motion occurring at up to hundreds of Hz.

Based on this sensing algorithm, robot foot information can be sensed for the design of robot control and algorithm. The displacement of robot foot motion was selected from the phase plot analysis before the analysis of the sensing implementation. Therefore, for the sensing results directly from embedded PZT voltage output, acceleration of foot motion should be integrated to get displacement, which may require further integral circuit design and lead to drift issue. However, there is certain chance that the acceleration phase plot can also be used to directly differentiate robot performance, as was observed with the displacement phase plot.

The optimization algorithms in this chapter are then developed based on the model for robot dynamics, with selected hypothetical on-board sensing information. Within the optimization algorithms presented in this chapter, PSO has a much better time-wise performance by trading off a much faster convergence rate for up to 30% reduction in average performance (speed), as a proof-of-concepts for the relationship between individual optimization and swarm optimization. CPSO, with clustering, performs 6% better than the conventional PSO in this proof-of-concept scenario. Notably, CPSO improves the algorithm performance without trading off any increased time or either each iteration or convergence. As observed from simulation, PSO performance gets worse if the diversity of robots increases, which emphasize the importance of applying clustering algorithm with on-board sensing features. In addition, the potential correlation between robot speed and selected sensing feature can weaken the urgency of external sensing. Worth attention here is that the parameters of swarm optimization algorithm, PSO and CPSO, are not optimized, so with further study into algorithm parameters, weights as an example, the algorithm performance may be further improved.

The limitation of the sensing model is the performance at high frequency. The sensing scheme cannot measure the rapid change in motion near impact of the robot foot, which usually happens on the scale of μs. This limitation emphasizes the importance of understanding robot dynamics. The dynamic model can help to correlate the relationship between low frequency robot leg motion and actual robot forward motion. Another

potential issue is that the sensing output voltage is associated with acceleration of foot, when information on robot velocity and displacement may be more closely related to the robot locomotion. On-board integration of the signal may require extra components and power consumption, so it would be useful to try to implement optimization of robot performance using acceleration measurements in future work. .

Some other future works also may improve the optimization algorithms. Instead of clustering at the first iteration only, further clustering can be executed every few iterations of optimization. This modification is related to clustering performance by repeating the process. The minimized sensing capability is observed to have an influence on generating robot actuation parameters for better robot performance. However, it is still unclear that how much improvement can be reached by adding more sensing capability without moving to more energy-intensive active control algorithms. Other than the algorithms presented in this work, additional evolutionary algorithms, such as genetic algorithm, are worth trying and modifying for robot optimization problem with individual diversity, because they are developed based on the biological examples in similar scale to the robots and swarms presented in this thesis.

CHAPTER 6 Centimeter-scale Robot with Jumping and Running Locomotion

6.1 Introduction

The design and fabrication of micro-robots, especially at the millimeter-scale, has benefitted from the development of progressively more sophisticated micro-fabrication processes. A significant diversity grows in locomotion options for micro-scale robots, with successes in running/walking [41, 119], crawling [32], flying [28, 29], jumping [31, 138], and swimming [139]. However, a single locomotion strategy may be restricted by environments, such as complex ground conditions or geometries and/or unpredictable air dynamics. To deal with environmental challenges, other than the improvement of single robot performance and capability, multi-robot cooperation and multi-locomotion robots are proposed as potential solutions in larger scale. Multi-robot cooperation is realized by coordinating multiple robots with the same [100, 140] or different [141] locomotion strategies. Multi-locomotion robots are defined as robots that are capable of moving with more than one type of gait or in multiple mediums, such as a crawling-jumping robot [142] or flying-walking robot [143]. This was recently extended into the micro-scale with an aerial-aquatic robot [144]. The objective of this work is to explore what can be done to allow different type of terrestrial motions at centimeter and smaller scale, especially using planar geometries that might scale to micro-scale fabrication techniques.

Meanwhile, centimeter-scale terrestrial robots can be functional on their own terms. Many research groups [44, 112, 118, 145, 146] have provided successful designs of either running/walking or jumping robots in small scales (<10 cm), with select designs compared in Table 12. In the centimeter-scale, electric motor actuation is powerful enough to move a robot more than 20 body lengths per second, with steering, as demonstrated in [145]. A vibratory robot with piezoelectric actuation is capable of moving a few body lengths per second with simpler actuator design, which benefits from the high power density of piezoelectric material. However, the high voltage of the actuation signal is a challenge to realize on-board power unit integration. Besides developing appropriate converter circuitry, another solution is thin-film piezoelectric materials. [44] presented a passive undulatory locomotion to realize biomimetic motion with 20 legs. [146] achieved fast locomotion, with the capability to steer with different bending vibration modes. [112] includes connection units onboard, but lacked an on-board power unit. The previous work in our group [118] demonstrates a centimeter-scale robot with a speed of 5 mm/s, and the extended design with this work has achieved a speed of 50 mm/s with more aggressive forward motion design. The robot design presented in [112, 118, 146] has the potential to be further scaled down to be compatible for micro-fabrication process. Some jumping robots are also developed to achieve different gait. [138] presents a robot that is capable of jumping more than one meter with motor actuation, and [142] shows a 10-centimeter robot that can both walk and jump with motor actuation and a mechanical energy storage system.

Table 12: Literature review of centimeter-scale running/walking and jumping robot

Design	Actuation	Gaits	Performance	Power	Power Unit
Qu [118]	Piezoelectric	Running/walking	0.14 body	2.7 mW	No

			length/s		
Hoffman [44]	Piezoelectric	Walking	0.5 body length/s	N/A	No
Dharmawan [146]	Piezoelectric	Running/walking with Steering	28 body length/s	1.45 W	No
Rios [112]	Piezoelectric	Running/walking	10.8 body length/s	2.49 W	Partial
Zarrouk [145]	Motor	Running/walking with Steering	200 body length/s	0.178 W	Yes
Haldane [138]	Motor	Jumping	~4 body height	1.22 J/jump	Yes
Jung [142]	Motor	Walking + Jumping	6.3 body length/s ~ 8 body height	2.2 W (walk) 25 J/jump	Yes
This work	Piezoelectric	Running + Jumping	3 body length/s 0.5 body height	46 mW (walk) 410 μJ/jump	No

Centimeter-scale running/walking robots can also serve as prototypes for fully micro-scale (having individual features down to the micron scale) robot design. When the design is scaled down, geometry-related properties will be influenced, such as resonant frequency, motion amplitude, so it is useful to model and study the robot locomotion based on modal analysis, which provides the capability to further understand the scaled robot.

In this chapter, inspired by the previous centimeter-scale piezoelectric walking robot design [118], we have modeled and tested a piezoelectric robot design with both running and jumping locomotion in centimeter-scale (< 40 mm). In this chapter, because at most one robot leg has contact with ground, the gait is strictly defined as running gait. However, if we extend our design with more legs, hexapod as an example, it is possible to realize both running and walking with this actuation design. The designated robot integrates a bulk bimorph lead zirconate titanate (PZT) actuator and 3D-printed polylactic acid (PLA) robot structure, and also has the potential to be further implemented in micro-scale with micro-fabricated thin-film PZT and parylene-C or polyimide structure. The

centimeter-scale robot is capable to jump at least half body height and walk more than 3 body lengths per second under varying actuation inputs. A simplified dynamic model is included to explain the locomotion at different frequency, and other actuation conditions, and the model is further extended to give a brief estimation for micro robot locomotion. Future millimeter-scale robots with multi-locomotion design can potentially be realized with current surface micro-fabrication process [114], and adjusting operation conditions, namely the actuation frequency and voltage.

6.2 Robot Architecture

A two-leg robot is designed and assembled to further study the locomotion of piezoelectrically actuated robot at small-scale, as shown in Figure 66. The structure of robot is 3D printed with PLA. One bimorph PZT actuator is bonded under the robot body and leg with epoxy. An intentional misalignment between the PZT actuator and robot leg generates a biased motion, which moves the robot forward. The robot stands on the flat bottom of its foot, which is to a certain extent influenced by the force from power cord, so during the experiments the power cords are connected after the robot is fully released, to minimize external force. From the understanding of robot dynamics generated in our previous study, it was recognized that it is important to synchronize robot legs within a hexapod design to achieve comparatively uniform motion performance. In this design, the leg number is reduced to two to ease the synchronization conditions. Also an actuator shared with two legs ensures the vibration modes of each robot foot are coupled.

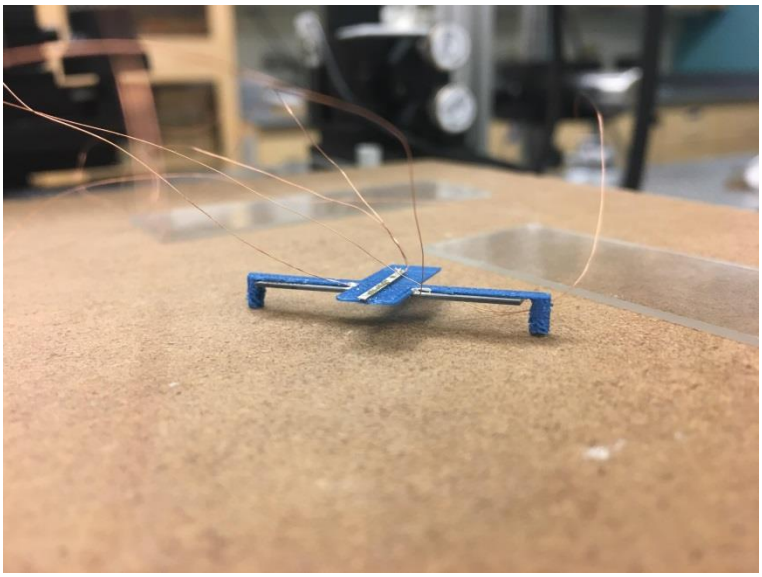

Figure 66. The photograph of a two-leg robot with PZT intentionally misaligned with its PLA leg. Extra sensing element on top of the body for future test, which is not included in this work.

The robot demonstrates jumping locomotion at low frequency with clear in-air motion and fast running locomotion with higher power consumption and efficiency. The two-leg robot suffers the balance issue, but it can help demonstrate one fundamental strategy locomotion at centimeter scale. A quadruped or hexapod robot with similar actuation design might benefit from the study of two-leg locomotion, and generate similar locomotion with rigid body connection if leg synchronization can be closely enforced.

6.3 Robot Dynamics

After we developed the hybrid dynamic model for millimeter-scale hexapod micro-robots and their centimeter-scale prototypes [119], a two-leg robot prototype was assembled to study robot gait. The two robot legs share a bulk bimorph PZT actuator, so

ideally the motion of two robot foot will be identical, though wobbling is observed in preliminary tests when the robot is actuated at high frequency, some hundreds of Hz. Meanwhile, the robot can walk quickly when actuated at around 200 Hz and 500 Hz, but is not able to overcome obstacles because of the limited step height and wobbling generated from differences in motion between the two legs at those speeds. To explain these observations, as shown in next section, and explore possible opportunities for scaling, a two-leg robot dynamic model is simplified from hexapod robot model.

In this simplified version of the robot model from previous chapters, only lateral and vertical motion of the robot interacts with two degrees of freedom vibration of the robot leg under actuation. Therefore, due to symmetry only one side of robot needs to be modeled to simulate robot motion. Some assumptions are made in this model:

A1. Both robot legs are identical to each other regarding actuation and structural condition.

A2. Both feet are in contact with the same ground condition.

A3. Higher order vibration modes are negligible in the model.

A4. Robot motion in vertical and lateral directions is decoupled, influenced independently by different actuation conditions.

With these assumptions, the state space model is shown as following:

$$\dot{x} = Ax + Bu$$

$$y = Cx$$

$$A = \begin{pmatrix} 1 & 0 & 0 & 0 \\ 0 & 1 & 0 & 0 \\ 0 & 0 & 0 & 1 \\ 0 & 0 & -kn_1 & -bn_1 \end{pmatrix} \qquad B = \begin{pmatrix} 0 & 0 \\ \frac{1}{m} & 0 \\ 0 & 0 \\ 0 & \frac{1}{m_{eff}} \end{pmatrix}$$

$$x = \begin{pmatrix} d_1 \\ v_1 \\ d_2 \\ v_2 \end{pmatrix}$$

in which kn_1 and bn_1 are the normalized spring constant and damping ratio, m and m_{eff} are the mass of half robot and the effective mass of the on robot side under tip force as a beam. Input u will be the force acting on the robot body and the force effectively acting on the robot foot to actuate vibration. The states of the system are the displacement (d) and velocity (v) of the robot body, as a rigid body, and of the robot leg vibration, as a vibrating beam. This state-space form is suitable for both vertical and lateral motion, but with different inputs to the systems. The actuation force is effectively modeled as tip force acting on the end of the robot leg in vibrating mode only, because the practical actuation in PZT actuator can only bend the entire leg in vertical direction.

During locomotion, two dynamic modes are considered in the model: in-air and impact. The in-air mode describes the free robot motion in air without interaction with ground. In this mode, the robot body and robot vibration are influenced by the gravity and actuation force only. The robot model will transition to the impact mode when the simulation detects that the robot foot will move below the ground within the next time step. During the impact mode, the robot body motion will be influence by the reaction force to the vibrating actuation force transmitted from the ground.

6.4 Dynamics and Locomotion Validation

6.4.1 Simulation

Based on the parameters identified from the data sheet of the PZT actuator, as shown in Table 13, two simulations with different actuation conditions are generated from the simplified mode described. Across simulations under same actuation condition, 5% resolution error is given to the robot leg properties, such as spring constant and damping ratio; to check the influence caused by structural properties. Two actuation conditions are simulated:

2 Hz actuation with 160V square wave

200 Hz actuation with 120V square wave

Table 13: Two-leg robot simulation parameters

Robot mass	0.49 g
Robot height	3.2 mm
Robot length	11 mm
Body width	36 mm
PZT actuator size	31.8 mm x 0.48 mm x 3.2 mm
PZT capacitance	4 nF
PZT blocked force	0.08 N
Resonant frequency	923 Hz
Damping ratio	1500 (Normalized)

In simulation condition A, the impact of both feet happens at almost same time, and is dominated by the phase change of the actuation signal, as shown in Figure 67 (left).

In condition A, the vertical jumping is always more than 1 mm from the simulations. As shown in Figure 67 (right), the simulated lateral speed is 3.9 ± 0.6 mm/s, and the simulation also shows a clear step within each actuation cycle.

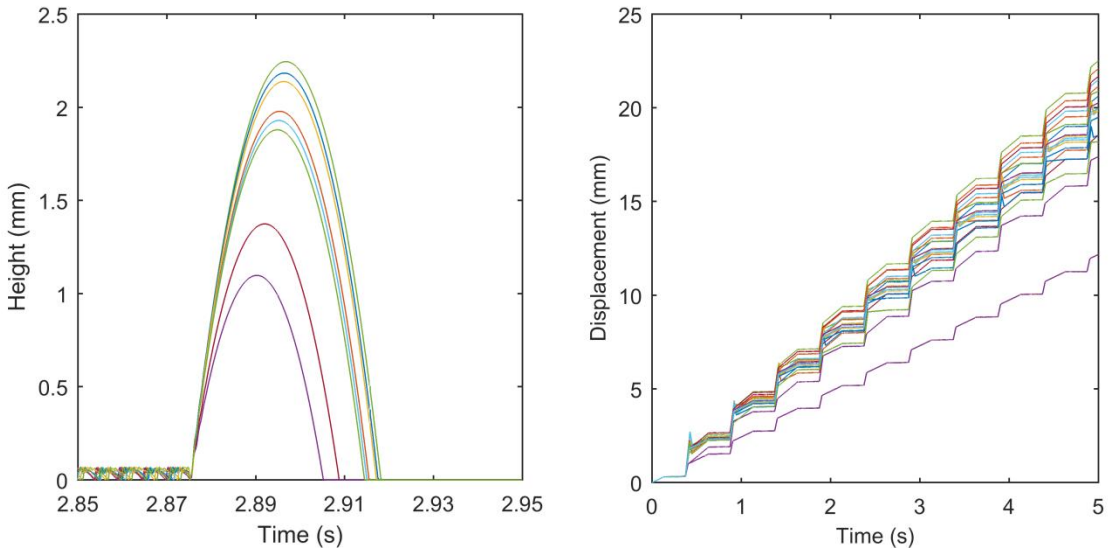

Figure 67: 20 runs of simulation of robot dynamics with 2Hz, 160V actuation, with 5% randomness between runs: (left) zoom-out vertical motion of robot with same take-off instance (5 samples plotted); (right) lateral displacement of 20 simulations.

In the simulation B, the contact instance varies from case to case, as shown in Figure 68 (left). This observation indicates that if two legs are not identical to each other, then this divergence is significant and will cause wobbling. A series of irregular contact instances is a random process in condition B, because the actuation period is less than the post-contact in-air time length. When the actuation frequency is further increased, the wobbling motion along the motion axis should be included in the model to accurately estimate robot motion, which is what was done for the hexapod robots in previous chapters, but not implemented here. Considering this high frequency performance, the robot vertical motion is less efficient in jumping and leads to lower possibility of the

jumping occurrence. However, rapid contact instances may be positively correlated with lateral speed. As shown in Figure 68 (right), the robot lateral speed at 200 Hz is 10.1 ± 1.4 mm/s.

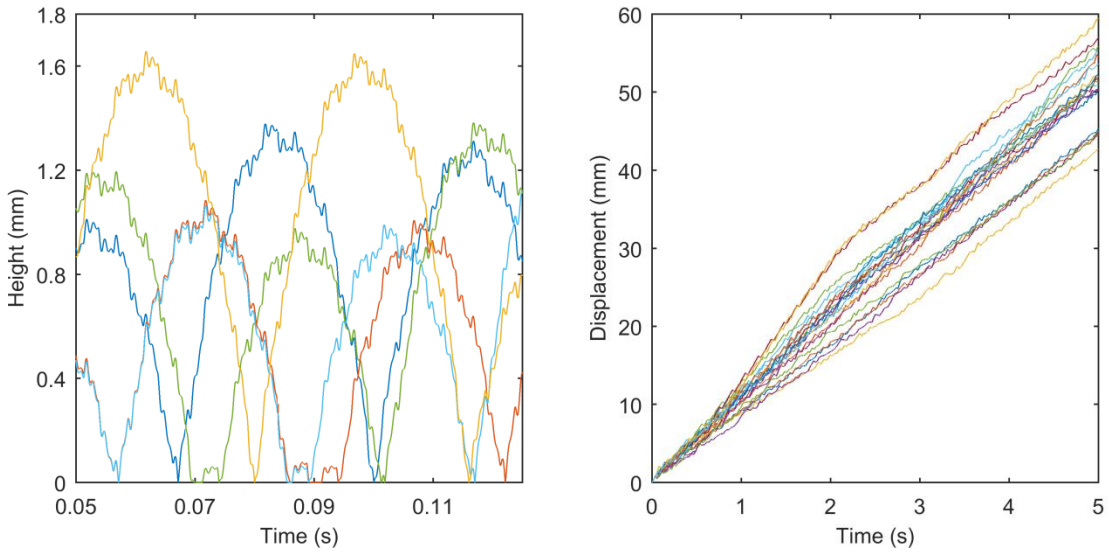

Figure 68: 20 runs of simulation of robot dynamics with 200Hz, 120V actuation, with 5% randomness between runs: (left) zoom-out vertical motion of robot with same take-off instance (5 samples plotted); (right) lateral displacement of 20 simulations.

6.4.2 Measurements

The two different type of locomotion are also observed in the robot test. At low frequency, less than 10 Hz, the robot is moving slowly but able to jump (> 2 mm) more than half of its' body height (< 4 mm). At high actuation frequency, the robot has a small probability of jumping, up to at most 1 mm, which is also similar to what indicated by the simulation. The lateral speed of the robot is simulated to be about 3.9 mm/s for actuation condition A and 10.1mm/s for condition B. The measured speed is 4.6 mm/s, as an average value, for condition A and 34 mm/s for condition B. The speed amplitude from simulation and experiments is close, though the measured speed of condition B is much

faster than simulated value. The higher measured speed may be caused by the increased number of contacts from wobbling process. The forward motion is about 3 body lengths per second though the body length can be even shorter because it's not a major design parameter.

Though we excluded the rotational motion of the robot, simulation results otherwise match the important phenomena observed experimentally, especially at low frequency. The detailed robot lateral motion is captured with a camera and image processing software, as shown in Figure 69 (left). Similar to Figure 67 (right), at low frequency a "step" displacement pattern happens at the same frequency as actuation. A close-to-linear trajectory of 200 Hz actuation is shown in Figure 69 (right), which indicates the model underestimated the robot speed at higher speed with irregular impact pattern. Figure 70 shows the measurement of robot foot vertical motion, at a different frequency, the low frequency drift could be from the surface roughness of the robot foot. However, the vertical motion amplitude and pattern is similar to what we simulated to be.

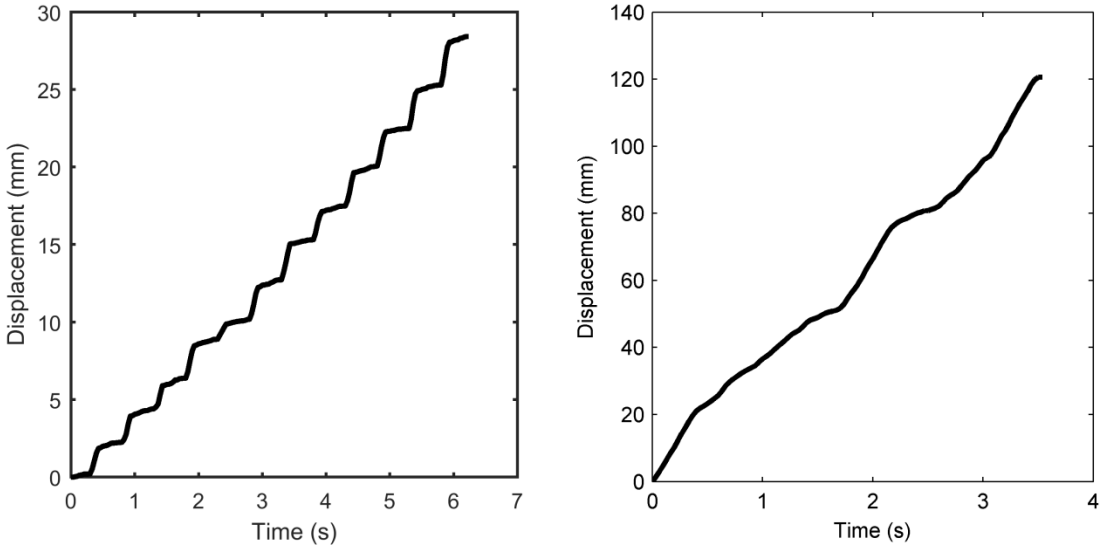

Figure 69: Sample of lateral displacement of two-leg robot with square wave at: (left) 2Hz, 160V; and (right) 200 Hz, 120 V.

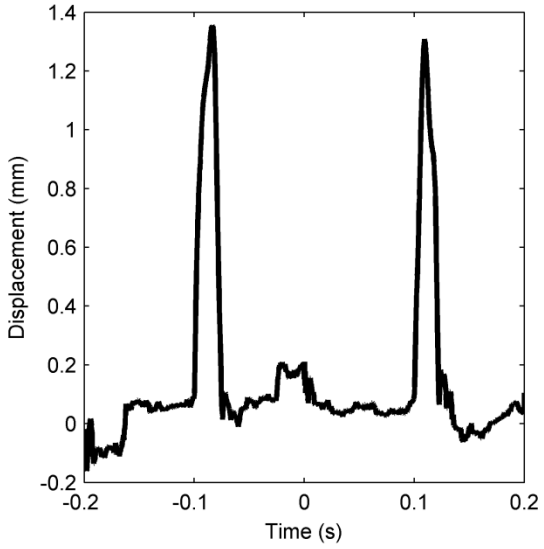

Figure 70: Sample of vertical displacement of two-leg robot with 5Hz, 160V square wave

6.4.3 Locomotion Boundary and Switch

Based on the simulation of condition A, the in-air time is less than 50 ms, so if the actuation frequency is about or higher than 20 Hz, jumping should not be expected to happen, as shown in Figure 71. During our test, this transient happens between 15 - 20 Hz, because we observed jumping at 15 Hz and did not observe jumping at 20 Hz, which is a close alignment with our simulation.

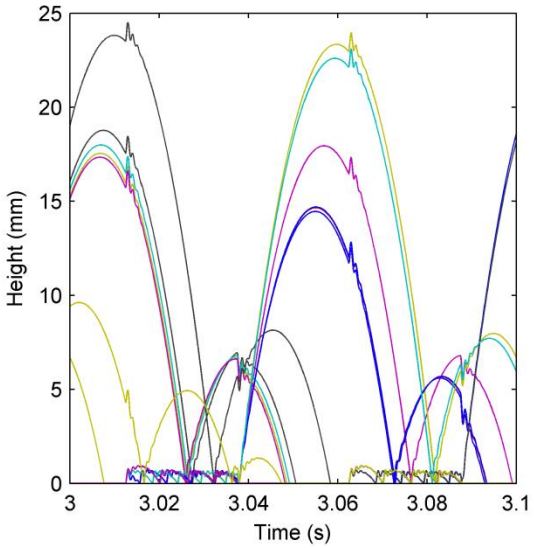

Figure 71: 20 runs of simulation of robot vertical motion with 20 Hz 160V actuation, with 5% randomness between runs

An open loop control algorithm has been implemented to realize the switch between running and jumping. The command starts and ends with two 0.4 s of 200 Hz 80V square wave, with one intermediate 2 s of 2 Hz 160 V square wave. Some sample frames of the motion are shown in Figure 72. The demonstrated open-loop control can help the robot overcome obstacles on the ground, but not as efficient as a feedback control approach. The feedback signal requires the integration of robot sensors, such as antenna[147] and motion sensors.

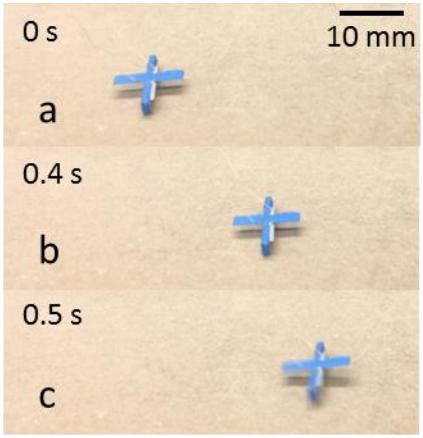

Figure 72: Sample frame of the robot running and jumping: a) initial condition before actuation signal; b) robot position after 0.4s running; c) robot in the middle of a jumping.

6.4.4 Power

Power consumption is another major concern for movable micro robots, because of the limitations of power storage technology and robot payload. The actuation signal in this work is a square wave to a capacitive piezoelectric load, so the major energy dissipation happens at the switching phase. When the settling time is less than the switching period, the total power dissipation for a actuation frequency is expressed as:

$$P = 2fE_1$$

in which E_1 is the energy dissipation of single switch, f is the actuation frequency. The single switch dissipation can be further expressed as:

$$E_1 = \frac{1}{2}CV^2$$

in which C is the capacitance of the PZT actuator and V is the actuation voltage. Low frequency jumping locomotion consumes less energy if its actuation signal amplitude is same as higher frequency.

The current of the actuation signal is measured with a current probe (Tektronix CT6), as shown in Figure 73. The dissipation is calculated by integrating the product of measured voltage and current of actuation signal. The current for the switching phase exists for less than 0.5 μs, so the calculation of the dissipation is useful with actuation frequency less than 1MHz. In reality, more charge may be lost during the switching phase due to the non-ideal circuit performance. Based on tests, the total energy dissipation for a single switch is more than 30 μJ for a 20V input step function. The energy stored on the actuator (E_1) is calculated to be more than 7 μJ, versus a calculated value of 3.2 μJ. The mismatch is attributed to parasitic capacitance and other resistive losses in the experimental setup. Therefore, the lower bound of energy dissipation for each individual jump at 2Hz is 819 μJ with the 160 V square wave. The energy dissipation due to parasitic capacitance would be reduced with integrated on-board power unit, and a charge recovery circuit [148] may help to partial of the lost across the capacitance during the switch.

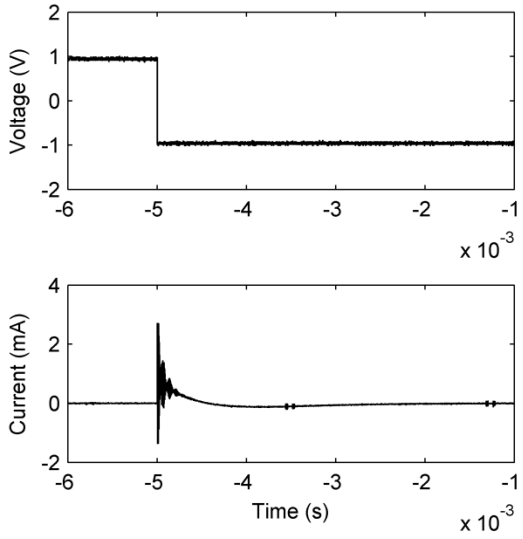

Figure 73: The power consumption measurement: actuation voltage and current of a single switch calculated from the integration of measured voltage and current.

6.5 Robot Dynamics and Locomotion Prediction

Here, the dynamic model is modified to provide some prediction of feasible robot locomotion at the micro-scale. The characterization and prediction of a millimeter-scale hexapod walking robot is presented in Chapter 4. Jumping locomotion is tested and simulated in this chapter. As shown in Figure 74, the robot is capable of jumping about 2 mm if the current centimeter-scale design is scaled down by 10 times in all dimensions other than the thin-film PZT, which is still 1 μm as designed in current millimeter-scale robot. Due to the fabrication constrain, a unimorph PZT layer is more realistic in millimeter scale, which should be designed to provide an actuation force in similar magnitude as bulk PZT actuators in centimeter scale. The simulation is delivered with 20V square wave actuation, which is the maximum actuation signal for current micro-

scale robot characterization, though this simulation may overestimate the robot performance by neglecting air damping. At the least, this simulation can provide a prediction that a similar jumping pattern will exists at smaller scale. The jumping amplitude in the simulation is significantly influenced by the actuation force from piezoelectric actuation, which indicates the importance of actuation structure design in micro scale.

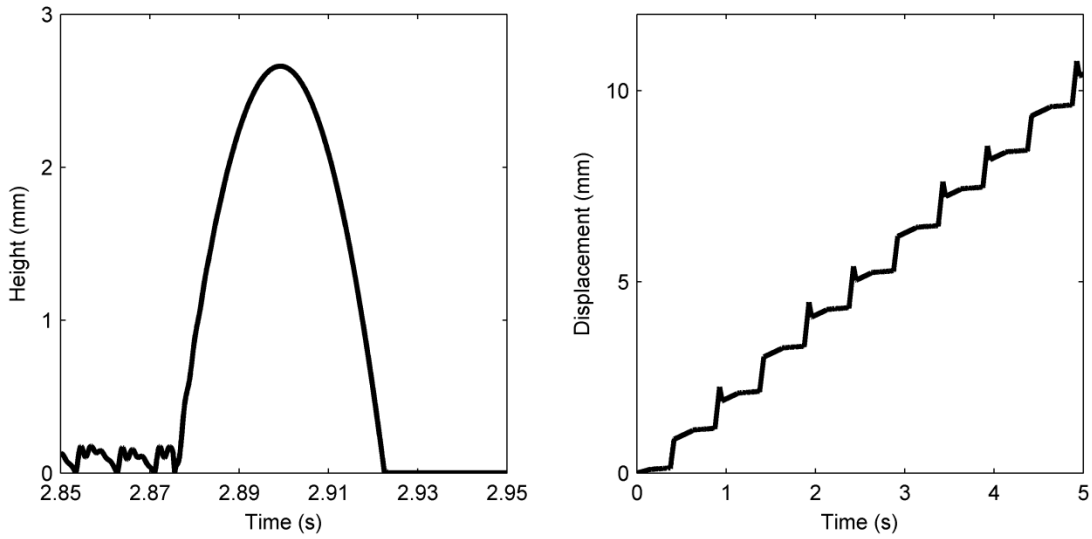

Figure 74: Robot jumping height and lateral motion estimation for the microrobot if which is scaled down by 10 times in all dimensions

6.6 Conclusion

In this work, we proposed a new centimeter-scale robot design intended to achieve multiple types of locomotion. The robot design using planar processing has the potential to be further realized in millimeter scale with existing micro-fabrication technologies. A fully assembled multi-locomotion robot is presented and tested, with a numerical dynamic model to understand and estimate its major dynamics in centimeter scale. This study indicates the potential of realizing multiple types of locomotion with a scaled-down robot design.

The robot in centimeter scale can jump more than half of robot height with low power consumption, as low as 819 μJ for each individual actuation period. The robot is also capable to walk as fast as 34 mm/s from our measurement, which is more than 3 body lengths per second. In practice, the switching between locomotion modes may someday rely on on-board sensing, to help overcome obstacles in the environment. Some preliminary works shows that using PZT actuators as sensors can solve the sensing issue without putting extra requirements to fabrication process based on the robot design.

This work provides a candidate solution for realizing multiple type of locomotion in the centimeter scale and further discusses the approach's feasibility at the millimeter-scale. With the fast running locomotion realized around robot resonance and the jumping locomotion at low frequency, the flexibility of robot motion in complex terrestrial condition is increased. The outcome of this work further emphasizes the importance of being able to synchronize leg motion despite presence of fabrication variability at high-frequency actuation, which could provide the potential of a jumping without slower robot speed. The first task in the future work is to add wobbling motion into the model, which can provide a more accurate jumping height estimation at different actuation conditions and at different scales, though current model with certain resolution can help to qualitatively demonstrate the locomotion limitation at certain actuation conditions. A locomotion switching algorithms should be prepared to take full use of the locomotion capability of the robot, which includes but is not limited to the on-board sensing and control algorithms.

CHAPTER 7 Summary and Future Work

7.1 Summary

In this dissertation, we have demonstrated modeling of nonlinear hybrid dynamics in small-scale for two applications: a magnetoelastic micro-motor and various piezoelectric compliant robots and scaled robot prototypes. The understanding of nonlinear dynamics of these devices can assist the design, sensing, and control to realize designated motion in the small-scale.

The bidirectional dynamic model of the piezoelectric compliant micro-motor is capable of predicting the major dynamic characteristics in frequency domain, with the understanding of rigid and compliant motion, contact dynamics, and fluidic dynamics. An innovative sensing scheme is designed for a Kalman estimator, based on the understanding of motor dynamics, to track motor motion.

The dynamics of small scale robots are studied with both centimeter-scale robot prototypes and a millimeter-scale micro-machined robot. The dynamic model, including robot rigid body motion, robot compliant foot motion, contact dynamics, and fluidic dynamics, is developed and validated with empirical results in the frequency and time domain. The robot performance of centimeter-scale prototypes is measured and compared with simulation of dynamic model for validation, which includes the robot foot and body motion in two directions. Then the model is scaled down to millimeter scale and validated with the characterization of millimeter-scale robot in chip and the performance of the externally actuated millimeter-scale robot.

After validation, the dynamic model is used to design optimization algorithms for simple robot control and new robot prototypes demonstrating multiple gaits, namely jumping and running. A sensing scheme is designed to use at least one on-board PZT actuator as a sensor that produces voltage signal proportional to foot acceleration. This scheme can keep the complexity of integrating on-chip sensing at current level because it introduces no more sensing layers and structures. The information from the sensor helps to monitor robot performance, and for proof-of-concept assessment, robots in a simulated swarm are clustered into different groups based on such hypothesized sensing information. The optimization algorithm uses minimal on-board sensing to improve the robot performance, with low computational complexity.

Meanwhile, multiple gaits are realized with a robot design using planar fabrication techniques, which can also conceptually be realized in micro-scale using conventional micro-machining processes. A simplified robot design is assembled in the centimeter-scale with rapid prototyping techniques to validate the design principle. Both jumping gait, more than half body height per jump, and running gait, more than 3 body lengths per second, are realized with this design with different actuation conditions.

7.2 Contributions

The contributions of this work can be categorized into two parts: the understanding of hybrid dynamics in small-scales and the extension work with dynamics. The hybrid dynamics of micro-motor and micro-robot are studied in this work, both devices have complex compliant motion at multiple resonant modes and nonlinear contact dynamics. In Chapter 2, a dynamic model for micro-motor is presented to explain the measured dynamics in frequency and time domain. Based on the dynamic model, a capacitive sensing scheme is designed to help the estimation of device motion. In Chapter 3 and 4, a general approach is presented for the dynamics of small-scale robots, both centimeter-scale prototypes and millimeter-scale robots. The validation covers scale factors, dynamic performance in frequency and time domain, and under various actuation

principles and structure design. Some predictions of micro-scale robot are provided based on the dynamic model developed. In Chapter 5 and 6, the understandings of dynamics helps design and validate the multi-gait robots and on-board sensing scheme with existing actuators, which are compatible with micro-fabrication process. Several optimization algorithms are studied, based on the on-board sensing signals, as examples to determine the importance of swarm operation and shared on-board sensing signals.

7.3 Future Work

The work in this dissertation provides some fundamental understanding of robot dynamics. With the understanding of dynamics, some extensive work can be done to improve the function and performance of robots in small-scale.

Based on the sensing implementation demonstrated in this work, it is possible to collect on-board sensing information. However, the relationship between sensing results of robot foot motion and lateral motion of robot body is not fully studied. This relationship can provide us a better idea of whether on-board sensing is necessary by understanding the maximum improvement that can be achieved with sensing. An estimation algorithm has been developed in our research group to track the robot foot motion with better accuracy. The next step is to develop an estimation algorithm to track the robot body motion with the information of robot foot motion. Some preliminary work has been done so far, but we are still looking for better estimators for micro-robots.

The power tether is a major issue for micro-robots, and centimeter-scale prototypes. During the testing of prototypes, the influence of the power tether should be tracked and eliminated to provide a reasonable estimation for free robot motion. For a

millimeter-scale robot, external actuation is a temporary solution for the missing power cord. An on-board power circuit is necessary to improve the testing results in centimeter-scale. Both cell battery and/or solar cell with converting circuit are potential solutions for this concern. The efficiency of the power unit may need to be optimized for robot application because piezoelectric actuation requires high voltage and fast switching.

Last but not least, the design of miniature robots can be improved based on the current understanding of robot dynamics, implementing multiple gaits as an example. The geometry of the robot foot and leg may be associated with various actuation patterns. The efficiency and performance of different designs can be evaluated with centimeter-scale prototypes. The robot weight optimization is another topic. Less weight will cause the actuation energy being absorbed by body compliant motion, and excessive weight will lead to less motion efficiency.

The future work mentioned here represents only a portion of the many tasks that could be addressed in the near future to realize practically-useful robots at small scales. I wish that my work on nonlinear hybrid dynamics of small-scale devices will thus help in improving the performance of these and related miniature devices.

REFERENCE

[1] N. Yazdi, F. Ayazi, and K. Najafi, "Micromachined inertial sensors," Proceedings of the IEEE, vol. 86, pp. 1640-1659, 1998.

[2] W. P. Eaton and J. H. Smith, "Micromachined pressure sensors: review and recent developments," Smart Materials and Structures, vol. 6, p. 530, 1997.

[3] S. B. Fuller, E. J. Wilhelm, and J. M. Jacobson, "Ink-jet printed nanoparticle microelectromechanical systems," Journal of Microelectromechanical systems, vol. 11, pp. 54-60, 2002.

[4] H. Toshiyoshi and H. Fujita, "Electrostatic micro torsion mirrors for an optical switch matrix," Journal of Microelectromechanical Systems, vol. 5, pp. 231-237, 1996.

[5] T. A. Schaedler, A. J. Jacobsen, A. Torrents, A. E. Sorensen, J. Lian, J. R. Greer, et al., "Ultralight metallic microlattices," Science, vol. 334, pp. 962-965, 2011.

[6] J. Qu, J. Tang, Y. B. Gianchandani, K. R. Oldham, and S. R. Green, "Dynamic modeling of a bidirectional magnetoelastic rotary micro-motor," Sensors and Actuators A: Physical, vol. 223, pp. 49-60, 2015.

[7] B. Kim, M. G. Lee, Y. P. Lee, Y. Kim, and G. Lee, "An earthworm-like micro robot using shape memory alloy actuator," Sensors and Actuators A: Physical, vol. 125, pp. 429-437, 2006.

[8] J. Tang, S. R. Green, and Y. B. Gianchandani, "Miniature Wireless Magnetoelastic Resonant Motor With Frequency Selectable Bidirectional Rotation," Journal of microelectromechanical systems, vol. 22, pp. 730-738, 2013.

[9] L.-S. Fan, Y.-C. Tai, and R. S. Muller, "IC-processed electrostatic micromotors," Sensors and actuators, vol. 20, pp. 41-47, 1989.

[10] H. Guckel, K. Skrobis, T. Christenson, J. Klein, S. Han, B. Choi, et al., "Fabrication and testing of the planar magnetic micromotor," Journal of Micromechanics and Microengineering, vol. 1, p. 135, 1991.

[11] H. Guckel, T. Christenson, K. Skrobis, T. Jung, J. Klein, K. Hartojo, et al., "A first functional current excited planar rotational magnetic micromotor," in Micro Electro Mechanical Systems, 1993, MEMS'93, Proceedings An Investigation of Micro Structures, Sensors, Actuators, Machines and Systems. IEEE., 1993, pp. 7-11.

[12] A. Iino, K. Suzuki, M. Kasuga, M. Suzuki, and T. Yamanaka, "Development of a self-oscillating ultrasonic micro-motor and its application to a watch," Ultrasonics, vol. 38, pp. 54-59, 2000.

[13] V. Kaajakari and A. Lal, "Micromachined ultrasonic motor based on parametric polycrystalline silicon plate excitation," Sensors and Actuators A: Physical, vol. 137, pp. 120-128, 2007.

[14] A. M. Flynn, L. S. Tavrow, S. F. Bart, R. A. Brooks, D. J. Ehrlich, K. R. Udayakumar, et al., "Piezoelectric micromotors for microrobots," Journal of Microelectromechanical systems, vol. 1, pp. 44-51, 1992.

[15] J.-S. Park, L. L. Chu, A. D. Oliver, and Y. B. Gianchandani, "Bent-beam electrothermal actuators-Part II: Linear and rotary microengines," Journal of Microelectromechanical systems, vol. 10, pp. 255-262, 2001.

[16] S. F. Bart, M. Mehregany, L. S. Tavrow, J. H. Lang, and S. D. Senturia, "Electric micromotor dynamics," Electron Devices, IEEE Transactions on, vol. 39, pp. 566-575, 1992.

[17] A. Endemano, J. Fourniols, H. Camon, A. Marchese, S. Muratet, F. Bony, et al., "VHDL–AMS modelling and simulation of a planar electrostatic micromotor," Journal of Micromechanics and Microengineering, vol. 13, p. 580, 2003.

[18] I. Dufour, E. Sarraute, and A. Abbas, "Optimization of the geometry of electrostatic micromotors using only analytical equations," Journal of Micromechanics and Microengineering, vol. 6, p. 108, 1996.

[19] J. Maas, P. Ide, N. Frohleke, and H. Grotstollen, "Simulation model for ultrasonic motors powered by resonant converters," in Industry Applications Conference, 1995. Thirtieth IAS Annual Meeting, IAS'95., Conference Record of the 1995 IEEE, 1995, pp. 111-120.

[20] N. W. Hagood IV and A. J. McFarland, "Modeling of a piezoelectric rotary ultrasonic motor," Ultrasonics, Ferroelectrics and Frequency Control, IEEE Transactions on, vol. 42, pp. 210-224, 1995.

[21] J. Maas, T. Schulte, and N. Frohleke, "Model-based control for ultrasonic motors," Mechatronics, IEEE/ASME Transactions on, vol. 5, pp. 165-180, 2000.

[22] D. Sun, J. Liu, and X. Ai, "Modeling and performance evaluation of traveling-wave piezoelectric ultrasonic motors with analytical method," Sensors and Actuators A: Physical, vol. 100, pp. 84-93, 2002.

[23] A. Frangi, A. Corigliano, M. Binci, and P. Faure, "Finite element modelling of a rotating piezoelectric ultrasonic motor," Ultrasonics, vol. 43, pp. 747-755, 2005.

[24] T. Yasuda, I. Shimoyama, and H. Miura, "Microrobot locomotion in a mechanical vibration field," Advanced Robotics, vol. 9, pp. 165-176, 1994.

[25] T. Ebefors, J. U. Mattsson, E. Kälvesten, and G. Stemme, "A walking silicon micro-robot," in Proc. Transducers' 99, Sendai, Japan, 1999, pp. 1202-1205.

[26] J. J. Abbott, M. C. Lagomarsino, L. Zhang, L. Dong, and B. J. Nelson, "How should microrobots swim?," The international journal of Robotics Research, 2009.

[27] U. Scarfogliero, C. Stefanini, and P. Dario, "A bioinspired concept for high efficiency locomotion in micro robots: the jumping robot grillo," in Robotics and Automation, 2006. ICRA 2006. Proceedings 2006 IEEE International Conference on, 2006, pp. 4037-4042.

[28] R. J. Wood, "The first takeoff of a biologically inspired at-scale robotic insect," Robotics, IEEE Transactions on, vol. 24, pp. 341-347, 2008.

[29] D. S. Drew and K. S. Pister, "First takeoff of a flying microrobot with no moving parts," in Manipulation, Automation and Robotics at Small Scales (MARSS), 2017 International Conference on, 2017, pp. 1-5.

[30] W. A. Churaman, L. J. Currano, C. J. Morris, J. E. Rajkowski, and S. Bergbreiter, "The first launch of an autonomous thrust-driven microrobot using nanoporous energetic silicon," Journal of Microelectromechanical Systems, vol. 21, pp. 198-205, 2012.

[31] S. Bergbreiter and K. S. Pister, "Design of an autonomous jumping microrobot," in Robotics and Automation, 2007 IEEE International Conference on, 2007, pp. 447-453.

[32] J.-S. Koh and K.-J. Cho, "Omegabot: Crawling robot inspired by ascotis selenaria," in Robotics and Automation (ICRA), 2010 IEEE International Conference on, 2010, pp. 109-114.

[33] S. Bergbreiter, "Effective and efficient locomotion for millimeter-sized microrobots," in Proceedings of IEEE/RSJ International Conference on Intelligent Robots and Systems, Nice, France, 2008, pp. 4030-4035.

[34] S. Firebaugh, J. Piepmeier, E. Leckie, and J. Burkhardt, "Jitterbot: A mobile millirobot using vibration actuation," Micromachines, vol. 2, pp. 295-305, 2011.

[35] R. S. Pierre, D. Vogtmann, and S. Bergbreiter, "Model-Based Insights on the Design of a Hexapod Magnetic Walker," in Experimental Robotics, 2016, pp. 715-727.

[36] D. R. Frutiger, K. Vollmers, B. E. Kratochvil, and B. J. Nelson, "Small, fast, and under control: wireless resonant magnetic micro-agents," The International Journal of Robotics Research, vol. 29, pp. 613-636, 2010.

[37] C. Pawashe, S. Floyd, and M. Sitti, "Modeling and experimental characterization of an untethered magnetic micro-robot," The International Journal of Robotics Research, vol. 28, pp. 1077-1094, 2009.

[38] B. R. Donald, C. G. Levey, C. D. McGray, I. Paprotny, and D. Rus, "An untethered, electrostatic, globally controllable MEMS micro-robot," Journal of microelectromechanical systems, vol. 15, pp. 1-15, 2006.

[39] P. Basset, A. Kaiser, P. Bigotte, D. Collard, and L. Buchaillot, "A large stepwise motion electrostatic actuator for a wireless microrobot," in Micro Electro Mechanical Systems, 2002. The Fifteenth IEEE International Conference on, 2002, pp. 606-609.

[40] K. Suzuki, I. Shimoyama, and H. Miura, "Insect-model based microrobot with elastic hinges," Journal of Microelectromechanical systems, vol. 3, pp. 4-9, 1994.

[41] S. Hollar, A. Flynn, C. Bellew, and K. Pister, "Solar powered 10 mg silicon robot," in Micro Electro Mechanical Systems, 2003. MEMS-03 Kyoto. IEEE The Sixteenth Annual International Conference on, 2003, pp. 706-711.

[42] P. E. Kladitis and V. M. Bright, "Prototype microrobots for micro-positioning and micro-unmanned vehicles," Sensors and Actuators A: Physical, vol. 80, pp. 132-137, 2000.

[43] R. Murthy, A. N. Das, D. O. Popa, and H. E. Stephanou, "ARRIpede: An assembled die-scale microcrawler," Advanced Robotics, vol. 25, pp. 965-990, 2011.

[44] K. L. Hoffman and R. J. Wood, "Passive undulatory gaits enhance walking in a myriapod millirobot," in Intelligent Robots and Systems (IROS), 2011 IEEE/RSJ International Conference on, 2011, pp. 1479-1486.

[45] K. Oldham, J. Pulskamp, R. Polcawich, P. Ranade, and M. Dubey, "Thin-film piezoelectric actuators for bio-inspired micro-robotic applications," Integrated Ferroelectrics, vol. 95, pp. 54-65, 2007.

[46] H. Woern, M. Szymanski, and J. Seyfried, "The I-SWARM project," in Robot and Human Interactive Communication, 2006. The 15th IEEE International Symposium on, 2006, pp. 492-496.

[47] K. L. Hoffman and R. J. Wood, "Myriapod-like ambulation of a segmented microrobot," Autonomous Robots, vol. 31, pp. 103-114, 2011.

[48] M. Shin, J. Choi, R. Q. Rudy, C. Kao, J. S. Pulskamp, R. G. Polcawich, et al., "Micro-Robotic Actuation Units Based on Thin-Film Piezoelectric and High-Aspect Ratio Polymer Structures," in ASME 2014 International Design Engineering Technical Conferences and Computers and Information in Engineering Conference, 2014, pp. V004T09A021-V004T09A021.

[49] A. M. Hoover, E. Steltz, and R. S. Fearing, "RoACH: An autonomous 2.4 g crawling hexapod robot," in Intelligent Robots and Systems, 2008. IEEE/RSJ International Conference on, 2008, pp. 26-33.

[50] K. Sugita, D. Tanaka, S. Ono, S. Chiba, K. Iwata, Y. Han, et al., "SMA actuator and pulse-type hardware neural networks IC for fast walking motion of insect-type MEMS microrobot," in Advanced Intelligent Mechatronics (AIM), 2016 IEEE International Conference on, 2016, pp. 431-435.

[51] R. P. LaRose III and K. D. Murphy, "Impact dynamics of MEMS switches," Nonlinear Dynamics, vol. 60, pp. 327-339, 2010.

[52] S. Lee, S. Howell, A. Raman, and R. Reifenberger, "Nonlinear dynamics of microcantilevers in tapping mode atomic force microscopy: a comparison between theory and experiment," Physical Review B, vol. 66, p. 115409, 2002.

[53] S. Krylov and D. I. Barnea, "Bouncing mode electrostatically actuated scanning micromirror for video applications," Smart materials and structures, vol. 14, p. 1281, 2005.

[54] B. F. Toler, R. A. Coutu Jr, and J. W. McBride, "A review of micro-contact physics for microelectromechanical systems (MEMS) metal contact switches," Journal of Micromechanics and Microengineering, vol. 23, p. 103001, 2013.

[55] L. Wu, J.-C. Golinval, and L. Noels, "A micro-model for elasto-plastic adhesive–contact in micro-switches: Application to cyclic loading," Tribology International, vol. 57, pp. 137-146, 2013.

[56] A. Granaldi and P. Decuzzi, "The dynamic response of resistive microswitches: switching time and bouncing," Journal of Micromechanics and Microengineering, vol. 16, p. 1108, 2006.

[57] C. Do, M. Cychowski, M. Lishchynska, M. Hill, and K. Delaney, "Integrated modeling of nonlinear dynamics and contact mechanics of electrostatically actuated RF-MEMS switches," in IECON 2010-36th Annual Conference on IEEE Industrial Electronics Society, 2010, pp. 2293-2298.

[58] B. McCarthy, G. G. Adams, N. E. McGruer, and D. Potter, "A dynamic model, including contact bounce, of an electrostatically actuated microswitch," Journal of microelectromechanical systems, vol. 11, pp. 276-283, 2002.

[59] D. A. Czaplewski, C. W. Dyck, H. Sumali, J. E. Massad, J. D. Kuppers, I. Reines, et al., "A soft-landing waveform for actuation of a single-pole single-throw ohmic RF MEMS switch," Journal of Microelectromechanical Systems, vol. 15, pp. 1586-1594, 2006.

[60] J. H. Ryou and K. R. Oldham, "System Identification of Contact Dynamics for a Piezoelectric Microactuator," in ASME 2012 5th Annual Dynamic Systems and Control Conference joint with the JSME 2012 11th Motion and Vibration Conference, 2012, pp. 227-234.

[61] J. H. Ryou and K. R. Oldham, "Model identification for impact dynamics of a piezoelectric microactuator," Journal of Micromechanics and Microengineering, vol. 22, p. 115002, 2012.

[62] J. H. Ryou and K. Oldham, "Foot-terrain interaction for a prototype silicon micro-robot," in ASME 2011 Dynamic Systems and Control Conference and Bath/ASME Symposium on Fluid Power and Motion Control, 2011, pp. 103-110.

[63] J. H. Ryou and K. R. Oldham, "Dynamic characterization of contact interactions of micro-robotic leg structures," Smart Materials and Structures, vol. 23, p. 055014, 2014.

[64] C. S. Casarez, J. H. Ryou, and K. R. Oldham, "Dimensional Analysis of Dynamic MEMS Micro-Robotic Walking Subject to Orthogonal Actuation and Small-Scale Forces," in ASME 2013 International Design Engineering Technical Conferences and Computers and Information in Engineering Conference, Portland, OR, 2013, pp. V001T09A022-V001T09A022.

[65] K. Uchino, "Piezoelectric ultrasonic motors: overview," Smart Materials and Structures, vol. 7, p. 273, 1998.

[66] R. Moroney, R. White, and R. Howe, "Ultrasonic micromotors: physics and applications," in Micro Electro Mechanical Systems, 1990. Proceedings, An Investigation of Micro Structures, Sensors, Actuators, Machines and Robots. IEEE, 1990, pp. 182-187.

[67] M. L. Chan, B. Yoxall, H. Park, Z. Kang, I. Izyumin, J. Chou, et al., "Design and characterization of MEMS micromotor supported on low friction liquid bearing," Sensors and Actuators A: Physical, vol. 177, pp. 1-9, 2012.

[68] T. Wang, C. Lancée, R. Beurskens, J. Meijer, B. Knapen, A. F. van der Steen, et al., "Development of a high-speed synchronous micro motor and its application in intravascular imaging," Sensors and Actuators A: Physical, vol. 218, pp. 60-68, 2014.

[69] T. Hosobata, A. Yamamoto, and T. Higuchi, "An electrostatic induction motor utilizing electrical resonance for torque enhancement," Sensors and Actuators A: Physical, vol. 173, pp. 180-189, 2012.

[70] X. Lu, J. Hu, L. Yang, and C. Zhao, "A novel dual stator-ring rotary ultrasonic motor," Sensors and Actuators A: Physical, vol. 189, pp. 504-511, 2013.

[71] K. Shcheglov, C. Evans, R. Gutierrez, and T. K. Tang, "Temperature dependent characteristics of the JPL silicon MEMS gyroscope," in Aerospace Conference Proceedings, 2000 IEEE, 2000, pp. 403-411.

[72] Y.-C. Tai, L.-S. Fan, and R. S. Muller, "IC-processed micro-motors: Design, technology, and testing," in Micro Electro Mechanical Systems, 1989, Proceedings, An Investigation of Micro Structures, Sensors, Actuators, Machines and Robots. IEEE, 1989, pp. 1-6.

[73] W.-M. Zhang, G. Meng, D. Chen, J.-B. Zhou, and J.-Y. Chen, "Nonlinear dynamics of a rub-impact micro-rotor system with scale-dependent friction model," Journal of Sound and Vibration, vol. 309, pp. 756-777, 2008.

[74] G. Meng, W.-M. Zhang, H. Huang, H.-G. Li, and D. Chen, "Micro-rotor dynamics for micro-electro-mechanical systems (MEMS)," Chaos, Solitons & Fractals, vol. 40, pp. 538-562, 2009.

[75] ASM Handbook: ASM International, 1989.

[76] I. Metglas. Magnetic Alloy 2826MB (nickel-based) Technical Bulletin [Online]. Available: http://www.metglas.com

[77] C. C. Lee, C. Y. Wang, and G. Matijasevic, "Au-In bonding below the eutectic temperature," Components, Hybrids, and Manufacturing Technology, IEEE Transactions on, vol. 16, pp. 311-316, 1993.

[78] W. W. So and C. C. Lee, "Fluxless process of fabricating In-Au joints on copper substrates," Components and Packaging Technologies, IEEE Transactions on, vol. 23, pp. 377-382, 2000.

[79] K. Takahata and Y. B. Gianchandani, "Batch mode micro-electro-discharge machining," Microelectromechanical Systems, Journal of, vol. 11, pp. 102-110, 2002.

[80] S. F. Foerster, M. Y. Louge, H. Chang, and K. Allia, "Measurements of the collision properties of small spheres," Physics of Fluids (1994-present), vol. 6, pp. 1108-1115, 1994.

[81] W.-M. Zhang and G. Meng, "Numerical simulation of sliding wear between the rotor bushing and ground plane in micromotors," Sensors and Actuators A: Physical, vol. 126, pp. 15-24, 2006.

[82] M. Behzad, M. Alvandi, D. Mba, and J. Jamali, "A finite element-based algorithm for rubbing induced vibration prediction in rotors," Journal of Sound and Vibration, vol. 332, pp. 5523-5542, 2013.

[83] S. Demiri, Geometric effects on the wear of microfabricated silicon journal bearings, 2010.

[84] A. P. Lee and A. P. Pisano, "Repetitive impact testing of micromechanical structures," Sensors and Actuators A: Physical, vol. 39, pp. 73-82, 1993.

[85] B. Bhushan, "Nanotribology and nanomechanics of MEMS devices," in Micro Electro Mechanical Systems, 1996, MEMS'96, Proceedings.'An Investigation of Micro Structures, Sensors, Actuators, Machines and Systems'. IEEE, The Ninth Annual International Workshop on, 1996, pp. 91-98.

[86] B. Bhushan and X. Li, "Micromechanical and tribological characterization of doped single-crystal silicon and polysilicon films for microelectromechanical systems," Journal of Materials Research, vol. 12, pp. 54-63, 1997.

[87] M. Bao and H. Yang, "Squeeze film air damping in MEMS," Sensors and Actuators A: Physical, vol. 136, pp. 3-27, 2007.

[88] W. Griffin, H. H. Richardson, and S. Yamanami, "A study of fluid squeeze-film damping," Journal of Basic Engineering, vol. 88, p. 451, 1966.

[89] M. Y. Okiishi, B. MUNSON, and D. YOUNG, "Fundamentals of Fluid Mechanics," John Wiley & Sons, Inc, 2006.

[90] J. Qu and K. R. Oldham, "Position estimation for a capacitively-sensed magnetoelastic rotary microstage using an extended Kalman smoother," in American Control Conference (ACC), 2014, 2014, pp. 3663-3668.

[91] S. Kim, J. E. Clark, and M. R. Cutkosky, "iSprawl: Design and tuning for high-speed autonomous open-loop running," The International Journal of Robotics Research, vol. 25, pp. 903-912, 2006.

[92] J. G. Cham, S. A. Bailey, J. E. Clark, R. J. Full, and M. R. Cutkosky, "Fast and robust: Hexapedal robots via shape deposition manufacturing," The International Journal of Robotics Research, vol. 21, pp. 869-882, 2002.

[93] M. Uemura and S. Kawamura, "Resonance-based motion control method for multi-joint robot through combining stiffness adaptation and iterative learning control," in Robotics and Automation, 2009. ICRA'09. IEEE International Conference on, 2009, pp. 1543-1548.

[94] M. Ruderman, F. Hoffmann, and T. Bertram, "Modeling and identification of elastic robot joints with hysteresis and backlash," Industrial Electronics, IEEE Transactions on, vol. 56, pp. 3840-3847, 2009.

[95] C.-H. Rhee, J. S. Pulskamp, R. G. Polcawich, and K. R. Oldham, "Multi-degree-of-freedom thin-film PZT-actuated microrobotic leg," Journal of Microelectromechanical Systems, vol. 21, pp. 1492-1503, 2012.

[96] U. Saranli, M. Buehler, and D. E. Koditschek, "RHex: A simple and highly mobile hexapod robot," The International Journal of Robotics Research, vol. 20, pp. 616-631, 2001.

[97] P. Birkmeyer, K. Peterson, and R. S. Fearing, "DASH: A dynamic 16g hexapedal robot," in Intelligent Robots and Systems, 2009. IROS 2009. IEEE/RSJ International Conference on, 2009, pp. 2683-2689.

[98] B. G. Lambrecht, A. D. Horchler, and R. D. Quinn, "A small, insect-inspired robot that runs and jumps," in Robotics and Automation, 2005. ICRA 2005. Proceedings of the 2005 IEEE International Conference on, 2005, pp. 1240-1245.

[99] J. M. Morrey, B. Lambrecht, A. D. Horchler, R. E. Ritzmann, and R. D. Quinn, "Highly mobile and robust small quadruped robots," in Intelligent Robots and Systems Proceedings. 2003 IEEE/RSJ International Conference on, 2003, pp. 82-87.

[100] J. Brufau-Penella, J. Sánchez-Martín, and M. Puig-Vidal, "Piezoelectric polymer model validation applied to mm size micro-robot I-SWARM (intelligent swarm)," in Smart Structures and Materials, 2006, pp. 61660Q-61660Q-12.

[101] D. L. DeVoe and A. P. Pisano, "Modeling and optimal design of piezoelectric cantilever microactuators," Journal of Microelectromechanical systems, vol. 6, pp. 266-270, 1997.

[102] J. G. Smits and W.-S. Choi, "The constituent equations of piezoelectric heterogeneous bimorphs," Ultrasonics, Ferroelectrics, and Frequency Control, IEEE Transactions on, vol. 38, pp. 256-270, 1991.

[103] S. S. Rao and F. F. Yap, Mechanical vibrations vol. 4. New York: Addison-Wesley, 1995.

[104] K. Knisely, C. Zhao, and K. Grosh, "A MEMS AlN transducer array with flexible interconnections for use as a cochlear implant," in AIP Conference Proceedings, 2015, p. 100004.

[105] C. Zhao, K. E. Knisely, and K. Grosh, "Modeling, fabrication, and testing of a MEMS multichannel aln transducer for a completely implantable cochelar implant," in Solid-State Sensors, Actuators and Microsystems (TRANSDUCERS), 2017 19th International Conference on, 2017, pp. 16-19.

[106] G. Gilardi and I. Sharf, "Literature survey of contact dynamics modelling," Mechanism and machine theory, vol. 37, pp. 1213-1239, 2002.

[107] R. Murthy, H. E. Stephanou, and D. O. Popa, "AFAM: An articulated four axes microrobot for nanoscale applications," IEEE Transactions on Automation Science and Engineering, vol. 10, pp. 276-284, 2013.

[108] E. Y. Erdem, Y.-M. Chen, M. Mohebbi, J. W. Suh, G. T. Kovacs, R. B. Darling, et al., "Thermally actuated omnidirectional walking microrobot," Journal of Microelectromechanical Systems, vol. 19, pp. 433-442, 2010.

[109] J. Qu, C. B. Teeple, and K. R. Oldham, "Modeling Legged Micro-Robot Locomotion based on Contact Dynamics and Vibration in Multiple Modes and Axes," Journal of Vibration and Acoustics, vol. 139, p. 031013, 2017.

[110] R. J. Full and M. S. Tu, "Mechanics of a rapid running insect: two-, four-and six-legged locomotion," Journal of Experimental Biology, vol. 156, pp. 215-231, 1991.

[111] C. Li, A. O. Pullin, D. W. Haldane, H. K. Lam, R. S. Fearing, and R. J. Full, "Terradynamically streamlined shapes in animals and robots enhance traversability through densely cluttered terrain," Bioinspiration & biomimetics, vol. 10, p. 046003, 2015.

[112] S. A. Rios, A. J. Fleming, and Y. K. Yong, "Miniature Resonant Ambulatory Robot," IEEE Robotics and Automation Letters, vol. 2, pp. 337-343, 2017.

[113] N. J. Kohut, A. O. Pullin, D. W. Haldane, D. Zarrouk, and R. S. Fearing, "Precise dynamic turning of a 10 cm legged robot on a low friction surface using a tail," in Robotics and Automation (ICRA), 2013 IEEE International Conference on, 2013, pp. 3299-3306.

[114] J. Choi, M. Shin, R. Q. Rudy, C. Kao, J. S. Pulskamp, R. G. Polcawich, et al., "Thin-film piezoelectric and high-aspect ratio polymer leg mechanisms for millimeter-scale robotics," International Journal of Intelligent Robotics and Applications, vol. 1, pp. 180-194, 2017.

[115] J. S. Pulskamp, R. G. Polcawich, and K. Oldham, "Highly Integrated Piezo-MEMS Enabled Millimeter-Scale Robotics," Proceedings of ASME IDETC/MNS, San Diego, CA, 2009.

[116] N. S. Tambe and B. Bhushan, "Scale dependence of micro/nano-friction and adhesion of MEMS/NEMS materials, coatings and lubricants," Nanotechnology, vol. 15, p. 1561, 2004.

[117] M. Dorigo and M. Birattari, "Swarm intelligence," Scholarpedia, vol. 2, p. 1462, 2007.

[118] J. Qu, C. B. Teeple, and K. R. Oldham, "Modeling Legged Microrobot Locomotion Based on Contact Dynamics and Vibration in Multiple Modes and Axes," Journal of Vibration and Acoustics, vol. 139, p. 031013, 2017.

[119] J. Qu, J. Choi, and K. Oldham, "Dynamic Structural and Contact Modeling for a Silicon Hexapod Microrobot," Journal of Mechanisms and Robotics, vol. 9, p. 061006, 2017.

[120] J. Qu and K. R. Oldham, "Estimators for micro-robot leg dynamics with uncertain jump conditions and infrequent sampling," in American Control Conference (ACC), 2016, 2016, pp. 5797-5802.

[121] S. Z. Mansour, R. J. Seethaler, Y. R. Teo, Y. K. Yong, and A. J. Fleming, "Piezoelectric Bimorph Actuator with Integrated Strain Sensing Electrodes."

[122] T. McPherson and J. Ueda, "A force and displacement self-sensing piezoelectric MRI-compatible tweezer end effector with an on-site calibration procedure," IEEE/ASME Transactions on Mechatronics, vol. 19, pp. 755-764, 2014.

[123] S. Kirkpatrick, C. D. Gelatt, and M. P. Vecchi, "Optimization by simulated annealing," science, vol. 220, pp. 671-680, 1983.

[124] P. J. Van Laarhoven and E. H. Aarts, "Simulated annealing," in Simulated annealing: Theory and applications, ed: Springer, 1987, pp. 7-15.

[125] Y. Shi and R. Eberhart, "A modified particle swarm optimizer," in Evolutionary Computation Proceedings, 1998. IEEE World Congress on Computational Intelligence., The 1998 IEEE International Conference on, 1998, pp. 69-73.

[126] J. Kennedy, "Particle swarm optimization," in Encyclopedia of machine learning, ed: Springer, 2011, pp. 760-766.

[127] J. Kennedy, "Stereotyping: Improving particle swarm performance with cluster analysis," in Evolutionary Computation, 2000. Proceedings of the 2000 Congress on, 2000, pp. 1507-1512.

[128] S. C. Johnson, "Hierarchical clustering schemes," Psychometrika, vol. 32, pp. 241-254, 1967.

[129] T. Low and W. Guo, "Modeling of a three-layer piezoelectric bimorph beam with hysteresis," Journal of Microelectromechanical Systems, vol. 4, pp. 230-237, 1995.

[130] A. T. Mineto, M. Braun, H. A. Navarro, and P. S. Varoto, "Modeling of a cantilever beam for piezoelectric energy harvesting," in 9th Brazilian Conference on Dynamics, Control and their Applications, 2010.

[131] J. G. Smits and A. Ballato, "Dynamic admittance matrix of piezoelectric cantilever bimorphs," Journal of microelectromechanical systems, vol. 3, pp. 105-112, 1994.

[132] J. G. Smits and W.-s. Choi, "The constituent equations of piezoelectric heterogeneous bimorphs," IEEE transactions on ultrasonics, ferroelectrics, and frequency control, vol. 38, pp. 256-270, 1991.

[133] Y. Wang, H. He, and R. Xu, "An analytical model for a piezoelectric vibration energy harvester with resonance frequency tunability," Advances in Mechanical Engineering, vol. 7, p. 1687814015590298, 2015.

[134] J. Ajitsaria, S.-Y. Choe, D. Shen, and D. Kim, "Modeling and analysis of a bimorph piezoelectric cantilever beam for voltage generation," Smart Materials and Structures, vol. 16, p. 447, 2007.

[135] S. Roundy, P. K. Wright, and J. M. Rabaey, "Energy scavenging for wireless sensor networks," Norwell, 2003.

[136] B. Edamana, B. Hahn, J. S. Pulskamp, R. G. Polcawich, and K. Oldham, "Modeling and Optimal Low-Power On–Off Control of Thin-Film Piezoelectric Rotational Actuators," IEEE/ASME Transactions on mechatronics, vol. 16, pp. 884-896, 2011.

[137] B. Hahn and K. R. Oldham, "A Model-Free ON–OFF Iterative Adaptive Controller Based on Stochastic Approximation," IEEE Transactions on Control Systems Technology, vol. 20, pp. 196-204, 2012.

[138] D. W. Haldane, M. Plecnik, J. K. Yim, and R. S. Fearing, "Robotic vertical jumping agility via series-elastic power modulation," Science Robotics, vol. 1, p. eaag2048, 2016.

[139] H. Li, J. Tan, and M. Zhang, "Dynamics modeling and analysis of a swimming microrobot for controlled drug delivery," Automation Science and Engineering, IEEE Transactions on, vol. 6, pp. 220-227, 2009.

[140] D. L. Christensen, E. W. Hawkes, S. A. Suresh, K. Ladenheim, and M. R. Cutkosky, "μTugs: Enabling microrobots to deliver macro forces with controllable adhesives," in Robotics and Automation (ICRA), 2015 IEEE International Conference on, 2015, pp. 4048-4055.

[141] C. J. Rose, P. Mahmoudieh, and R. S. Fearing, "Coordinated launching of an ornithopter with a hexapedal robot," in Robotics and Automation (ICRA), 2015 IEEE International Conference on, 2015, pp. 4029-4035.

[142] G.-P. Jung, C. S. Casarez, S.-P. Jung, R. S. Fearing, and K.-J. Cho, "An integrated jumping-crawling robot using height-adjustable jumping module," in Robotics and Automation (ICRA), 2016 IEEE International Conference on, 2016, pp. 4680-4685.

[143] R. J. Bachmann, F. J. Boria, R. Vaidyanathan, P. G. Ifju, and R. D. Quinn, "A biologically inspired micro-vehicle capable of aerial and terrestrial locomotion," Mechanism and Machine Theory, vol. 44, pp. 513-526, 2009.

[144] Y. Chen, H. Wang, E. F. Helbling, N. T. Jafferis, R. Zufferey, A. Ong, et al., "A biologically inspired, flapping-wing, hybrid aerial-aquatic microrobot," Science Robotics, vol. 2, p. eaao5619, 2017.

[145] D. Zarrouk and R. S. Fearing, "Controlled in-plane locomotion of a hexapod using a single actuator," IEEE Transactions on Robotics, vol. 31, pp. 157-167, 2015.

[146] A. G. Dharmawan, H. H. Hariri, S. Foong, G. S. Soh, and K. L. Wood, "Steerable miniature legged robot driven by a single piezoelectric bending unimorph actuator," in Robotics and Automation (ICRA), 2017 IEEE International Conference on, 2017, pp. 6008-6013.

[147] R. Rudy, A. J. Cohen, J. S. Pulskamp, R. G. Polcawich, and K. R. Oldham, "Antenna-Like Tactile Sensor for Thin-Film Piezoelectric Micro-Robots," in ASME 2013 International Design Engineering Technical Conferences and Computers and Information in Engineering Conference, 2013, pp. V001T09A023-V001T09A023.

[148] Y. Moon and D.-K. Jeong, "An efficient charge recovery logic circuit," IEEE journal of solid-state circuits, vol. 31, pp. 514-522, 1996.